POLYTECHNIQUE MONTRÉAL
affiliée à l'Université de Montréal

Photoluminescence of isotopically purified germanium

MARCIN WAJS
Département de génie physique

Thèse présentée en vue de l'obtention du diplôme de *Philosophiæ Doctor*
Génie physique

Août 2025

POLYTECHNIQUE MONTRÉAL
affiliée à l'Université de Montréal

Cette thèse intitulée :

Photoluminescence of isotopically purified germanium

présentée par **Marcin WAJS**
en vue de l'obtention du diplôme de *Philosophiæ Doctor*
a été dûment acceptée par le jury d'examen constitué de :

Maksim SKOROBOGATIY, président
Sébastien FRANCOEUR, membre et directeur de recherche
Rémo MASUT, membre
Louis GAUDREAU, membre externe

DEDICATION

I'll manage to turn back, I'm sure
I'll surprise the dusk with light
Somewhere at the end of the world I'll find myself
I think I'd like to be there already.

Zawrócić zdążę wiem
Zaskoczę światłem zmierzch
Gdzieś na końcu świata odnajdę się
Chyba chciałbym już tam być.

Myslovitz - "Do utraty tchu"

ACKNOWLEDGEMENTS

Writing this thesis has been far from an individual effort, and there are many people without whom it would never have come to fruition.

First of all, I wish to thank my research group. Sébastien, for taking me on board, giving me space to grow as a scientist, and for all the physics discussions I will fondly remember. Anne-Laurence, for teaching me how to be a good experimentalist and for persevering through the pandemic-induced idleness. Simon, for never giving up and for being good at everything I wasn't able to do. I want to thank Alaric, Mathias, Maxime, Rayan, Clément, Arnaud, Shaghayegh, Amine, Romain, and many others with whom I have had the pleasure of sharing the lab.

My research would not have been possible without the support from Polytechnique Montréal and funding agencies who generously provided the necessary resources. I am also grateful to our friends from across Génie Physique - in particular, Oussama Moutanabbir and the members of his research group. Among them, Samik Mukherjee played a key role in devising and designing the crystal growth techniques, subsequently implemented at IKZ by the team led by Radhakrishnan Sumathi. Special thanks go to Nicolas for bringing the samples to our lab that one afternoon, precipitating the 150 pages that follow.

I want to thank my parents, Ola and Paweł, for being the most wonderful family I could have asked for. Despite the physical distance I have put between us, I always knew I could rely on your support unconditionally. Your names belong on the front page of this thesis every bit as much as mine.

Szymon, Andrzej, Miśka, thank you for knowing me better than I know myself and for being there for me whenever I needed you. Kajtek, thank you for not giving up on my lackluster planning skills. Antek, thank you for always being Antek.

Ania, Ola, Czarek, Jacek, Kuba, Mateusz, and Maciek, you have witnessed the moment this thesis was completed, but much more importantly, you have given me conviction that I could

aim high. Your company is always a blast, and your strength has been an inspiration.

I want to thank all my Montréal friends, especially Ian, for always having a solution, and Earl, for being a reminder of what is important in life. Canadian kindness is much more than a cliché.

Last but not least, I wish to thank the jury members for committing their time to reading my thesis. I am looking forward to ending this chapter of my life with a proper scientific discussion with you.

RÉSUMÉ

Le germanium a émergé comme une plateforme prometteuse pour les technologies quantiques, avec des applications allant des points quantiques aux qubits de spin, en raison de ses hautes mobilités de charge et de son couplage spin-orbite intrinsèquement important. Cette thèse présente une investigation complète de la photoluminescence (PL) indirecte dans le germanium naturel de haute pureté, culminant avec une analyse détaillée des effets isotopiques dans des échantillons isotopiquement purifiés de ^{72}Ge, ^{73}Ge, ^{74}Ge et ^{76}Ge.

La fondation de cette recherche a été établie grâce à une optimisation méticuleuse de l'appareillage expérimental. Une percée critique a été réalisée en résolvant les décalages d'alignement induits par le spectromètre, réduisant les décalages du plan focal du détecteur de plus de 100 μm à moins de 3 μm sur la gamme 0-3000 nm. Étant donné la nécessité de coupler le signal PL dans une fibre optique avec un MFD de 8 μm, cette amélioration de stabilité d'un facteur 30 a permis les mesures de haute qualité qui sous-tendent toutes les analyses subséquentes.

Un cadre théorique complet pour les formes de raies de PL indirecte a été développé et rigoureusement validé, englobant toutes les contributions connues incluant la densité d'états jointe, la structure fine de l'état fondamental excitonique, les corrections de non-parabolicité des bandes, l'élargissement collisionnel, et les effets instrumentaux. Le modèle a permis la détermination précise de la séparation énergétique de l'état fondamental excitonique comme $\Delta E = 0,77 \pm 0,05$ meV par ajustement spectral direct, avec une validation indépendante par dépendance en température donnant $\Delta E = 0,7 \pm 0,2$ meV.

Une avancée théorique significative a été réalisée en identifiant le mécanisme d'élargissement collisionnel dominant. Par une analyse systématique, ce travail a démontré de manière concluante que l'élargissement collisionnel est principalement causé par les interactions exciton-porteur libre plutôt que par les collisions exciton-exciton, contredisant directement la littérature établie.

L'investigation systématique des conditions d'excitation a révélé des dépendances importantes qui étaient précédemment incomplètement comprises. Les effets de longueur d'onde

laser sur les exposants de puissance ($k \approx 1$ pour 1059 nm versus $k \approx 1,5$ pour 532 nm) ont été attribués à des profondeurs de pénétration dépendantes de la longueur d'onde affectant les interactions de défauts plutôt qu'à des effets fondamentaux de structure de bandes. L'analyse des effets d'ouverture numérique a démontré le rôle dominant de la diffusion externe latérale des porteurs, tandis que les études dépendantes de la température ont révélé des phénomènes de localisation de porteurs produisant une augmentation dramatique de PL à faibles puissances d'excitation. Ces découvertes fournissent des aperçus cruciaux pour optimiser les conditions expérimentales et comprendre la dynamique des porteurs.

L'analyse isotopique complète représente la réalisation primaire de cette thèse. Des échantillons de haute pureté de ^{72}Ge, ^{73}Ge, ^{74}Ge, et ^{76}Ge ont été investigués avec des rapports signal-sur-bruit sans précédent. Les décalages énergétiques isotopiques ont démontré un excellent accord avec les prédictions théoriques basées sur l'échelle $M_v^{-1/2}$. Pour la première fois, les énergies absolues de phonons ont été déterminées pour tous les modes acoustiques et optiques à travers les quatre isotopes avec des incertitudes inférieures à 0,4 meV. La renormalisation de la bande interdite électronique due aux interactions électron-phonon a été précisément déterminée comme -45 ± 3 meV. La caractérisation systématique a révélé une dépendance isotopique genuines dans les rapports d'intensité TO/LA, tout en établissant que des effets tels que l'élargissement de désordre isotopique se produisent en dessous des limites de résolution expérimentale actuelles.

Cette analyse multidimensionnelle, progressant de l'optimisation expérimentale à travers la validation théorique jusqu'à la caractérisation spectrale et isotopique complète, représente une des investigations les plus approfondies de la photoluminescence indirecte dans le germanium. Les découvertes fournissent des données de référence essentielles pour la recherche future tout en résolvant plusieurs controverses de longue date dans le domaine, avec des implications importantes pour les applications de technologie quantique où les temps de cohérence et la pureté du matériau sont des considérations critiques.

ABSTRACT

Germanium has emerged as a promising platform for quantum technologies, with applications ranging from quantum dots to spin qubits, owing to its high charge mobilities and intrinsically large spin-orbit coupling. This thesis presents a comprehensive investigation of indirect photoluminescence (PL) in high-purity natural germanium, culminating in a detailed analysis of isotopic effects in isotopically purified samples of ^{72}Ge, ^{73}Ge, ^{74}Ge and ^{76}Ge.

The foundation of this research was established through meticulous optimization of the experimental apparatus. A critical breakthrough was achieved in solving spectrometer-induced alignment shifts, reducing detector focal plane shifts from over 100 μm to less than 3 μm across the 0-3000 nm range. Given the necessity of coupling PL signal into a fiber optic with MFD of 8 μm, this 30-fold improvement in stability enabled the high-quality measurements that underpin all subsequent analyses.

A comprehensive theoretical framework for indirect PL lineshapes was developed and rigorously validated, encompassing all known contributions including joint density of states, excitonic ground state fine structure, band non-parabolicity corrections, collisional broadening, and instrumental effects. The model enabled accurate determination of the excitonic ground state energy splitting as $\Delta E = 0.77 \pm 0.05$ meV through direct spectral fitting, with independent validation through temperature dependence yielding $\Delta E = 0.7 \pm 0.2$ meV.

A significant theoretical advancement was achieved in identifying the dominant collisional broadening mechanism. Through systematic analysis, this work conclusively demonstrated that collisional broadening is predominantly caused by exciton-free carrier interactions rather than exciton-exciton collisions, directly contradicting established literature.

Systematic investigation of excitation conditions revealed important dependencies which were previously incompletely understood. Laser wavelength effects on power exponents ($k \approx 1$ for 1059 nm versus $k \approx 1.5$ for 532 nm) were attributed to wavelength-dependent penetration depths affecting defect interactions rather than fundamental band structure effects. Analysis of numerical aperture effects demonstrated the dominant role of lateral carrier out-diffusion, while temperature-dependent studies revealed carrier localization phenomena producing dra-

matic PL enhancement at low excitation powers. These findings provide crucial insights for optimizing experimental conditions and understanding carrier dynamics.

The comprehensive isotopic analysis represents the primary achievement of this thesis. High-purity samples of ^{72}Ge, ^{73}Ge, ^{74}Ge, and ^{76}Ge were investigated with unprecedented signal-to-noise ratios. Isotopic energy shifts demonstrated excellent agreement with theoretical predictions based on $M_v^{-1/2}$ scaling. For the first time, absolute phonon energies were determined for all acoustic and optical modes across all four isotopes with uncertainties below 0.4 meV. The electronic band gap renormalization due to electron-phonon interactions was precisely determined as -45 ± 3 meV. Systematic characterization revealed genuine isotopic dependence in TO/LA intensity ratios, while establishing that effects such as isotopic disorder broadening occur below current experimental resolution limits.

This multidimensional analysis, progressing from experimental optimization through theoretical validation to comprehensive spectral and isotopic characterization, represents one of the most thorough investigations of indirect photoluminescence in germanium. The findings provide essential reference data for future research while resolving several long-standing controversies in the field, with important implications for quantum technology applications where coherence times and material purity are critical considerations.

TABLE OF CONTENTS

LIST OF TABLES

LIST OF FIGURES

LIST OF SYMBOLS AND ACRONYMS

Physical Constants

k_B	Boltzmann constant
$\hbar$	Reduced Planck constant
c	Speed of light
e	Elementary charge
m_e	Electron rest mass

Material Properties and Band Structure

E_g	Bandgap energy
a_0	Lattice parameter
ε_r	Relative dielectric constant
ε_1, ε_2	Real and imaginary parts of dielectric function
m_r	Reduced effective mass
E_x	Exciton binding energy
D_i	Deformation potential constant
ΔE	Energy splitting in excitonic ground state
α	Absorption coefficient
n_{op}	Optical refractive index
k	Extinction coefficient
R	Sample reflectance
$\mathcal{R}$	Reflectance (alternative notation)

Spectral and Optical Parameters

λ	Wavelength
ω	Angular frequency
$h\nu$	Photon energy
I_{PL}	Photoluminescence intensity
$I^{PL}_{allowed}$	PL intensity for allowed transitions
$I^{PL}_{forbidden}$	PL intensity for forbidden transitions
I_0	PL intensity at zero temperature
$I_{\max}$	Maximum laser beam intensity

Lineshape and Broadening Parameters

$E_{\max}$	Energy at intensity maximum
$E_{1,2}$	Half-maximum energies
FWHM	Full width at half maximum
Γ_L	Lorentzian broadening (full width)
σ	Gaussian broadening (standard deviation)
σ_{res}	Instrumental resolution
γ_{nat}	Natural decay rate
γ_{coll}	Collision rate
γ_{tot}	Total decay rate
$\Delta\omega$	Raman peak width

Carrier Densities and Populations

n	General particle density
n_e	Free electron density
n_h	Free hole density
n_x	Exciton density
$\overline{n}(z)$	Average excess carrier concentration
$\overline{n}_{av}$	Volume-averaged carrier concentration
N_c	Conduction band effective density of states
N_v	Valence band effective density of states
N_x	Exciton density of states
N_A	Acceptor defect density
N_A^0	Neutral acceptor density
f_c, f_v	Fermi-Dirac occupation probabilities
$n_{Q_j}(T)$	Bose-Einstein distribution function

Temperature and Thermal Parameters

T	Temperature
T_c	Critical temperature
T_{platform}	Platform temperature
T_{elec}	Electronic temperature
β	Inverse thermal energy, $1/k_BT$
T_{LA}	Electronic temperature from LA peak
T_{TO}	Electronic temperature from TO peak
T_{TA}	Electronic temperature from TA peak
$F(N_q)$	Phonon occupation factor

N_q	Phonon occupation number
E_a	Activation energy

Collision and Interaction Parameters

ρ_c	Weisskopf collision radius
$\bar{v}$	Average relative collision velocity
$\Delta\omega$	Collisional energy shift
$V(r)$	Interaction potential
σ	Collision cross-section
$\delta\phi$	Phase shift from collision
$\phi(0)$	Binding energy of EHL at zero temperature
$V(q)$	Electron-phonon coupling matrix element
$V(G)$	Pseudopotential factor

Experimental Setup Parameters

P_{laser}	Laser power
P_0	Total incident laser power
P_{532}, P_{633}, P_{790}, P_{1059}	Power of specific wavelength lasers
k	Power exponent
I_{bias}	SNSPD bias current
I_{crit}	Critical bias current
η	Coupling efficiency
$\eta_{\text{coll}}(z)$	Optical collection efficiency
w_1, w_2	Beam widths ($1/e^2$)
w_0	Beam waist at focal point
MFD	Mode field diameter
NA	Numerical aperture
a	Lateral displacement

Spectrometer and Alignment Parameters

θ	Grating angle
α_{ROLL}	Grating roll angle
α_{TILT}	Grating tilt angle
α_1, α_2	Rotation axis angles
Δx	Grating displacement
w_{slit}	Spectrometer slit width

Rate Constants and Coefficients

c_P	Photogeneration coefficient
c_x	Radiative recombination coefficient
c_{nA}	Defect capture coefficient
A, B	Model constants
$\|\|M_{cv}\|\|^2$	Transition matrix element squared

Quantum States and Transitions

$\psi(t)$	Time-dependent wavefunction
E_F	Fermi energy
ΔF	Quasi-Fermi level separation
Γ_i	Group theory representations
H_1, H_2	Interaction Hamiltonians
H_{e-p}	Electron-phonon interaction Hamiltonian
$\widehat{H}$	Hamiltonian operator
$\Delta\widehat{H}$	Hamiltonian correction
$c^\dagger_{k+q}$, c_k	Electron creation and annihilation operators
a_{Q_j}, $a^\dagger_{Q_j}$	Phonon creation and annihilation operators
$\langle\psi\|\Delta\widehat{H}\|\psi\rangle$	Energy shift expectation value

Phonon Modes and Energies

$\hbar\omega_q$	Phonon energy
$\vec{q}$	Phonon wavevector
LA	Longitudinal acoustic phonon
TA	Transverse acoustic phonon
LO	Longitudinal optical phonon
TO	Transverse optical phonon
$\hbar\omega_{Q_j}$	Phonon energy at wavevector Q_j
ω_{Q_j}	Phonon frequency at wavevector Q_j
k_{Q_j}	Force constant at wavevector Q_j
k_{TO}, k_{LA}, k_{TA}	Force constants for TO, LA, TA modes
ΔE_{TO-LA}	Energy separation between TO and LA peaks
ΔE_{LA-TA}	Energy separation between LA and TA peaks
ΔE_{LO-LA}	Energy separation between LO and LA peaks

Isotopes and Nuclear Properties

^{70}Ge, ^{72}Ge, ^{73}Ge, ^{74}Ge, ^{76}Ge	Germanium isotopes
^{nat}Ge	Natural germanium
^{28}Si	Silicon-28 isotope
Nuclear spin	Intrinsic angular momentum
M_v	Average atomic mass
$\overline{M_v}$	Mean isotopic mass
ΔM	Change in atomic mass

Isotopic Effects and Energy Shifts

$\Delta E_{electronic}$	Electronic energy shift due to isotopic mass
ΔE_{DW}	Debye-Waller energy shift
ΔE_{SE}	Self-energy contribution
E_0	Transition energy at infinite mass limit
$\langle u^2 \rangle$	Mean squared phonon amplitude
$\lvert u(Q_j) \rvert$	Displacement field amplitude
$\lvert \langle u(Q_j) \rangle \rvert^2$	Thermal average of displacement squared
$u(R)$	Atomic displacement at position R
G	Reciprocal lattice vector

States and Excitonic Complexes

FE	Free exciton
BE	Bound exciton
EHD	Electron-hole droplet
EHL	Electron-hole liquid
x_1	Lower energy split state
x_2	Higher energy split state
r	Intensity ratio between split states
r_0	Intensity ratio at zero temperature

Diffusion and Transport Parameters

D	Diffusion coefficient
L_{eff}	Effective diffusion length
s_0	Surface recombination velocity
τ	Recombination lifetime
$G(r, z)$	Carrier generation rate

Mathematical Functions and Variables

W_k	Lambert W function (branch k)
x	General exponent in lineshape expression
V	Volume
Ω	Solid angle
R	Ratio of free to total carrier density
X_f^2	Brewster angle reflectometry parameter
ϕ_b	Brewster angle
N	Number of atoms per unit cell

CHAPTER 1 INTRODUCTION

Germanium's position in the periodic table testifies to its important and interesting properties. It is situated in Group IV below carbon — the backbone of organic life — and silicon — which lies at the heart of virtually all electronic devices we use in our daily lives. Taking a wider view, it is one of only a handful of elemental semiconductors, it can be manufactured with extraordinarily high purity, contains a range of stable isotopes, and exhibits electrical transport properties superior to those of silicon. It is no wonder, then, that interest in germanium has been rising, sparked particularly by the search for suitable materials for future quantum technologies.

Germanium's historical role is no less important. The first transistor, developed at Bell Labs in December 1947, was based on a Ge crystal. In the ensuing race for supremacy in microelectronics, silicon emerged victorious due to its scalability, thermal stability, and the excellent quality of its native oxide, SiO_2. However, in modern high-tech quantum applications, these traditional concerns are often secondary to fundamental properties, which is where germanium holds the upper hand [1].

A key concern in quantum applications is maintaining the coherence of a physical system. This can be achieved by using high-purity materials (including isotopic purification) with high crystal quality and by interfacing them with light, which can provide high coherence over large distances. This thesis addresses both aspects through a photoluminescence (PL) study of isotopically purified samples of ^{72}Ge, ^{73}Ge, ^{74}Ge and ^{76}Ge, supported by an extensive PL investigation of ultra-high purity natural Ge.

1.1 Germanium as a semiconductor

Understanding germanium's semiconductor properties is essential for analyzing its photoluminescence, as these fundamental properties determine all spectral features observed in PL experiments. These properties are the subject of this section, followed by the next section where Ge is evaluated alongside other semiconductor alternatives for quantum technology applications.

Germanium crystallizes in the diamond cubic structure with a Fd$\bar{3}$m space group (shown in Fig. 1.1a), identical to silicon and carbon diamond. It consists of two interpenetrating face-centered cubic (FCC) lattices displaced by one-quarter of the body diagonal. The lattice parameter at room temperature is $a_0 = 5.6575$ Å, which is only $\sim 4\%$ larger than that of silicon. This structural similarity enables the growth of high-quality Ge/Si systems, despite the lattice mismatch.

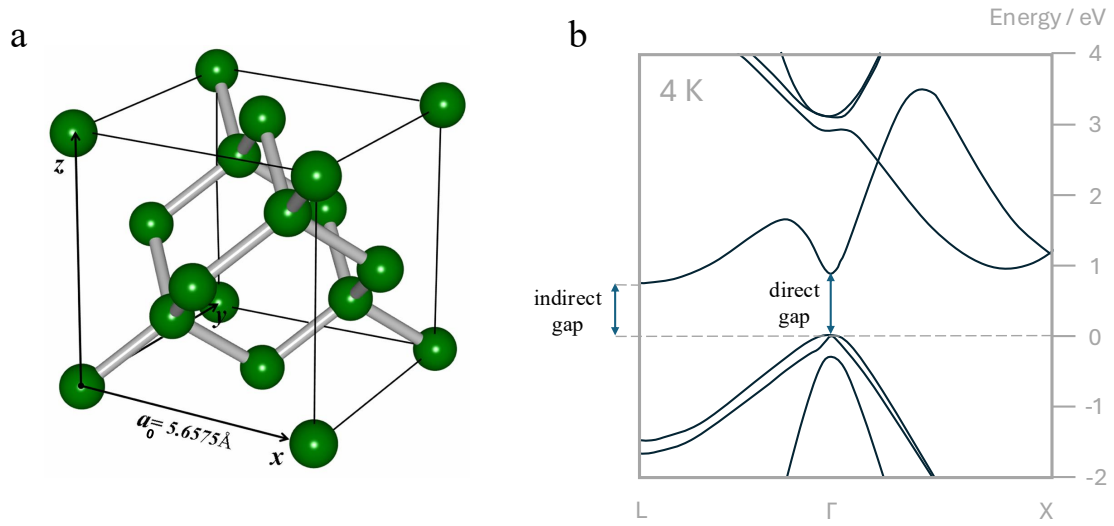

Figure 1.1 a) Diamond cubic crystal structure of Ge (adapted from [2]) and b) the band structure of Ge at 4 K (data from [3]).

The electronic band structure of germanium, shown in Fig. 1.1b, exhibits the typical features of an indirect bandgap semiconductor. The valence band maximum is found at the Γ-point, while the conduction band minimum is located at the L-points along the [111] directions. This band structure results in an indirect energy gap of $E_g = 0.66$ eV at room temperature and 0.74 eV at 0 K [4], while direct gap energies are 0.8 and 0.89 eV respectively. These values make germanium particularly suitable for NIR applications in the λ range of 1.3–1.8 μm.

Another notable feature of Ge's band structure is the spin-orbit coupling (SOC) which lifts the 6-fold degeneracy of the valence band at the Γ-point. The split-off band is located ~ 0.3 eV below the light and heavy hole bands which are also split by a small energy difference of < 1 meV. The significance of this strong SOC is further explored in the next section.

The phonon spectrum of germanium plays a fundamental role in determining its optical and thermal properties, particularly in the context of photoluminescence processes where phonon-assisted transitions dominate due to the indirect bandgap nature. The diamond cubic structure gives rise to six phonon branches: three acoustic branches (one longitudinal acoustic LA and two transverse acoustic TA) and three optical branches (one longitudinal optical LO and two transverse optical TO). Since the two transverse branches in each category are energy-degenerate, phonon energies are typically characterized by four distinct values corresponding to the LA, TA, LO, and TO modes. The phonon dispersion diagram is shown in Fig. 1.2, along with a Ge PL spectrum exhibiting peaks associated with the four phonon modes. The spectrum will be explored in detail in Chapter 4.

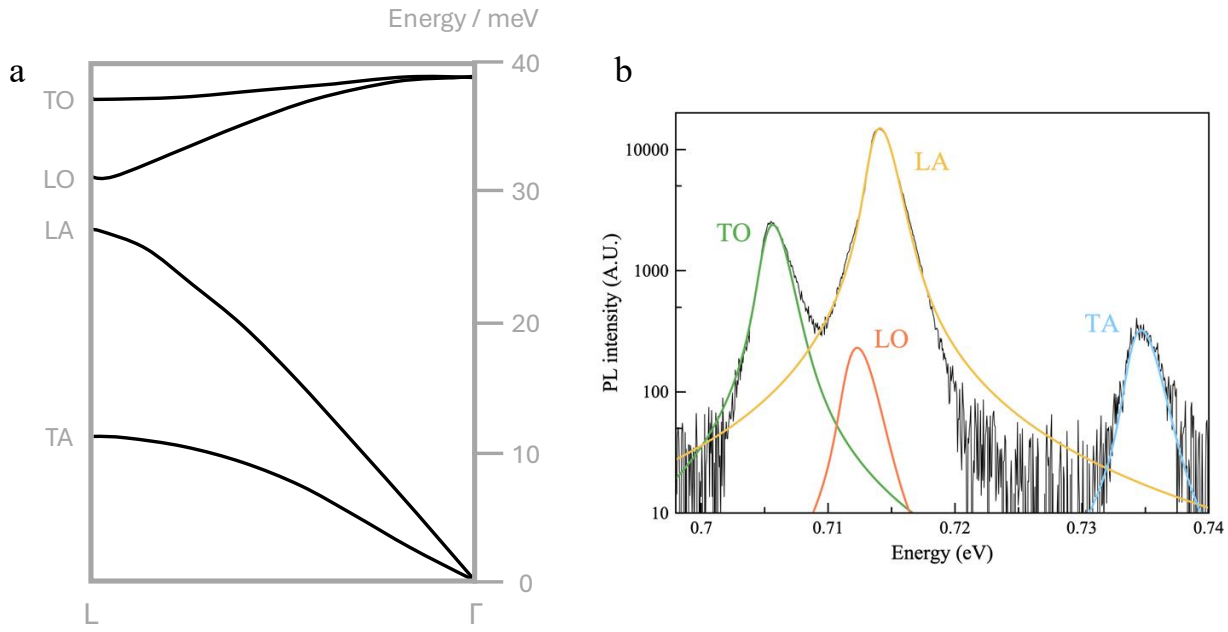

Figure 1.2 a) Phonon dispersion diagram (data from [5]) and b) a typical Ge PL spectrum.

Germanium has a wide isotopic spread with atomic masses ranging from 70 to 76. All stable isotopes have a nuclear spin of 0+ with the exception of ^{73}Ge which has a non-zero nuclear spin. Isotopic purification can therefore be used for eliminating nuclear spin noise on one hand, or controlling the density of non-zero nuclear spins on the other, if said spins are intended to be a part of a quantum system. Stable isotopes along with their natural abundances and nuclear spins are shown in Table 1.1.

Table 1.1 Stable isotopes of germanium, their natural abundances and nuclear spins.

Isotope	Natural Abundance (%)	Nuclear spin
^{70}Ge	20.38	0+
^{72}Ge	27.31	0+
^{73}Ge	7.76	9/2+
^{74}Ge	36.72	0+
^{76}Ge	7.83	0+

The high dielectric constant of germanium ($\varepsilon_r \approx 16$ [6]) is an important consideration in quantum device engineering as it leads to strong screening of charged impurities and defects. This screening effect reduces the spatial extent of electrostatic fluctuations around charged centers, thereby minimizing their impact on the nearby quantum states. For quantum applications, this translates to reduced sensitivity to the charge noise, which is particularly important for spin qubits which couple to electric field fluctuations via SOC.

Other properties affected by the large dielectric constant exciton binding energies and the spatial extent of excitonic wave functions, affecting the efficiency of optical transitions used in quantum photonic applications. In the context of the PL measurements (as well as laser control and read-out schemes), the pronounced refraction and a high reflection coefficient (which stem the from large ε_r) must be considered when optimizing the excitation and the collection efficiency.

1.2 Semiconductor comparison

The choice of semiconductor material determines the performance characteristics and practical limitations of quantum devices. Each material presents different trade-offs between key parameters such as coherence time, gate speed, operating temperature and the ease of integration. Table 1.2 compares a range of important properties of four common semiconductor candidates for quantum technologies: germanium (Ge), silicon (Si), gallium arsenide (GaAs), and indium arsenide (InAs).

Germanium emerges as an attractive choice due to its exceptional carrier mobility characteristics. With a hole mobility of 1900 cm^2/Vs, germanium significantly outperforms silicon (480 cm^2/Vs), GaAs (400 cm^2/Vs), and InAs (500 cm^2/Vs) [7]. High hole mobility is crucial

Table 1.2 Comparison of key properties for spin-based quantum technologies across different semiconductors. Mobility and bandgap values at 300K [7].

Property	Ge	Si	GaAs	InAs
Bandgap (eV)	0.67	1.12	1.42	0.36
Hole mobility (cm^2/Vs)	1900	480	400	500
Electron mobility (cm^2/Vs)	3900	1350	8500	40000
SOC strength (meV)*	290 [3]	< 0.1 [8]	340 [9]	430 [9]
Spin coherence time (μs)**	1-10 [10]	10-100 [11]	0.1-1 [12]	0.1-1 [13]
Operating T (mK)*** [14]	10-100	10-50	10-4000	10-100
CMOS compatibility	Yes	Yes	No	No
Primary quantum advantage	Fast gates via EDSR	Long coherence	Direct gap	Strong SOC, topological qubits

*Spin-orbit coupling strength varies significantly with confinement geometry and electric fields
**Spin dephasing time for quantum dot qubits, highly dependent on nuclear environment
***Typical operating range for spin qubits; specific values depend on qubit type and fidelity requirements

for engineering fast quantum gates, which are essential for advanced quantum algorithms and error correction protocols [14]. Additionally, germanium exhibits strong spin-orbit coupling (290 meV), allowing electrical control of spin states through charge manipulation. This eliminates the need for magnetic field control, allowing gate operations to be performed significantly faster than the times required for magnetic resonance techniques while opening possibilities for efficient laser-based control schemes.

The preference for spin-based quantum systems over charge-based alternatives stems from their limited interactions with the environment. Spin degrees of freedom couple weakly to the ubiquitous electrical fluctuations that rapidly destroy charge-based quantum states, resulting in significantly longer coherence times. Furthermore, magnetic fields associated with spins are naturally more localized than electric fields from charges, enabling the engineering of smaller, more scalable quantum systems. The intrinsic two-level nature of a carrier spin provides an ideal foundation for the implementation of a qubit.

Silicon represents the opposite extreme when it comes to the spin-orbit coupling. Its exceptionally weak SOC (0.04 meV) accounts for the longest coherence times among the compared materials (10-100 μs [11]), as spins are effectively decoupled from electrical noise sources.

However, this weak coupling necessitates magnetic field control for spin manipulation, fundamentally limiting gate operation speeds and requiring the lowest operating temperatures (10-50 mK) [14]. Despite these limitations, silicon remains as a feasible option due to its compatibility with established CMOS fabrication processes and the possibility of isotopic purification (^{28}Si) to eliminate nuclear spin noise [15].

The main advantage of gallium arsenide for quantum photonic applications is its direct bandgap, which enables highly efficient optical processes including on-demand single photon generation and spin-photon interfaces critical for quantum networking. However, GaAs suffers from very short coherence times (0.1-1 μs [12]) due to the nuclear spin noise from both gallium and arsenic atoms, which cannot be eliminated through isotopic purification, and typically higher defect densities compared to silicon. Additionally, GaAs is incompatible with CMOS processing due to its compound semiconductor nature and requires specialized III-V fabrication techniques and substrates that significantly increase cost and complexity.

Indium arsenide combines the optical advantages of a direct bandgap semiconductor (0.36 eV) with the strongest spin-orbit coupling (430 meV) among the materials compared in Table 1.2. It also exhibits proximity-induced superconductivity, meaning that an inherently non-superconducting material (InAs) can host superconducting currents when placed adjacent to a superconducting material [16]. The strong SOC, when combined with proximity-induced superconductivity, can potentially host topologically protected Majorana fermions that offer inherent immunity to major decoherence mechanisms [17]. However, the realization of topological quantum computing remains technically challenging, requiring precise control over multiple parameters including magnetic fields, chemical potential, and superconducting proximity effects. Additionally, like GaAs, InAs suffers from short coherence times and CMOS incompatibility, limiting its near-term practical applications.

Each semiconductor thus occupies a distinct niche in the quantum technology landscape, with no single material providing optimal performance across all metrics. Germanium stands out as it offers an attractive balance between fast electrical control and reasonable coherence times, while maintaining CMOS compatibility. The detailed investigation of germanium's properties, particularly isotopic effects that influence spin coherence, is therefore of considerable technological importance.

1.3 Ge-based semiconductor devices

Recent advances in semiconductor fabrication have fundamentally transformed the viability of germanium-based devices, overcoming the critical material limitations that hindered germanium transistor development in the 1950s. These technological breakthroughs have reopened germanium as a competitive platform for both classical and quantum semiconductor applications.

The most significant development has been the successful implementation of germanium-compatible high-permittivity dielectrics, including hafnium oxide (HfO_2) and aluminum oxide (Al_2O_3), as alternatives to the problematic native germanium oxide [18]. This advancement explicitly addresses the fundamental obstacle that previously limited germanium's potential in device applications. Native GeO_2 suffers from multiple critical deficiencies: it readily desorbs under typical processing conditions, exhibits water solubility that compromises device stability, proves difficult to control during fabrication, and contains prohibitively high defect densities [1]. These characteristics make GeO_2 incompatible with essential device architectures such as MOSFETs, which require stable, high-quality gate oxides for proper operation. The introduction of alternative high-κ dielectrics completely circumvents these limitations, enabling the fabrication of high-performance germanium-based electronic devices.

A complementary approach exploits the crystallographic similarity between germanium and silicon [19]. The identical diamond cubic crystal structure and closely matched lattice parameters enable epitaxial growth of germanium layers on silicon substrates. This approach allows quantum systems to be implemented in germanium while taking advantage of the mature and extensively optimized silicon fabrication infrastructure developed over decades of industrial refinement. The resulting Ge-on-Si platform combines germanium's superior quantum properties with silicon's manufacturing advantages and cost-effectiveness.

Additional efforts focus on enhancing germanium's optical properties by engineering a transition from its inherent indirect bandgap to direct bandgap behavior. This transformation is feasible due to the relatively small energy difference between the indirect (Γ-valley) and direct (L-valley) transitions in germanium's band structure. Mechanical strain engineering, achieved through epitaxial growth on lattice-mismatched substrates, induces changes in the band structure that can promote direct gap behavior [20]. The resulting strain-induced modification of the conduction band alignment enhances optical efficiency and enables ap-

plications in integrated photonics. Similarly, compositional engineering through tin doping ($Ge_{1-x}Sn_x$ alloys) has shown particular promise, as tin incorporation progressively reduces the indirect-direct gap difference, ultimately enabling direct bandgap behavior at sufficient tin concentrations [21].

These fabrication advances have enabled successful demonstration of various germanium-based device architectures that validate its technological potential. High-performance germanium FinFETs have achieved competitive performance, exploiting germanium's superior hole mobility while maintaining excellent electrostatic control through innovative gate structures [22]. For quantum applications, gate-defined germanium quantum dot arrays have demonstrated single-electron occupancy and coherent spin manipulation, proving germanium's viability as a quantum computing platform [23]. Similarly, strained Ge/SiGe quantum well heterostructures have realized high-mobility two-dimensional hole gases with exceptional transport properties suitable for scalable quantum processors [24]. Beyond these emerging applications, germanium has already achieved commercial success in integrated photonics, where Ge-on-Si photodetectors and electro-optic modulators are routinely manufactured for high-speed optical communication systems. These diverse implementations across classical and quantum electronics, as well as photonics demonstrate that germanium has successfully transitioned from laboratory curiosity to an industrially viable platform.

1.4 Objectives of the study

Detailed understanding of germanium's interaction with light as well as the impact of isotopic composition are key to unlocking its potential for applications in quantum technologies. Yet, most reference studies on Ge photoluminescence (natural or isotopically purified) were reported decades ago, using inferior samples and measuring devices compared to those available today. Lengthy PL acquisition techniques not only compromised data accuracy, but also made it impractical to perform comprehensive studies resolved in multiple parameters (such as temperature and laser power), leading to inconsistent conclusions offered across the literature.

The overarching objective of this thesis was to perform a comprehensive investigation of photoluminescence of isotopically enriched ^{72}Ge, ^{73}Ge, ^{74}Ge and ^{76}Ge samples of unprecedented elemental and isotopic purity. To that effect, robust understanding of indirect PL lineshapes and the impact of excitation conditions in Ge was developed, based on extensive experimen-

tal data resolved in multiple parameters. This allowed accurate extraction of information from PL spectra with minimized uncertainties, as well as addressing some long-standing unresolved questions in the scientific literature. All this relied on a state-of-the-art IR detection system which made it practically feasible to conduct such a wide-ranging experimental study.

Indirect photoluminescence spectroscopy was chosen as it offers several advantages over alternative characterization techniques. Unlike absorption measurements, PL enables the study of carrier dynamics through temperature-dependent measurements and provides enhanced sensitivity to trace defect concentrations, which is particularly relevant for high-purity materials. It is less invasive than transport measurements, which rely on microfabrication processes that can locally compromise sample quality. Furthermore, since Ge is an inherently weak light emitter due to its indirect bandgap, this spectroscopic method benefits more than others from recent advances in IR detection technology.

1.5 The outline of the thesis

Chapter 2 discusses the experimental methods employed during PL measurements to ensure excellent detection efficiency in the $1.6 - 1.8\,\mu$m spectral range of interest. It provides an overview of the instruments and optical components of the experimental setup, including the rationale behind specific instrument choices. Particular attention is devoted to SNSPD detectors, both due to their central role and because the manufacturer provided limited information about system specifications, which required independent investigation. The key contribution described in Chapter 2 is an analysis of spectrometer-induced alignment shifts that initially compromised this study. Theoretical modeling led to the design of a practical solution that ensured high alignment stability.

Chapter 3 introduces three theoretical models referenced in subsequent chapters. First, it discusses the theory of indirect photoluminescence, including a demonstration of selection rules for phonon modes in Ge and derivation of the theoretical spectral lineshape for allowed and forbidden transitions. Second, Weisskopf theory of collisional broadening is presented in the context of charge carriers in semiconductors. Finally, the theory of power exponents in semiconductor PL is discussed, based on a model developed by Schmidt et al. [25] and extended by Spindler et al. [26]

Chapter 4 builds upon the first of these models (the spectral lineshape in indirect photo-

luminescence) to include the fine structure of the exciton and various types of broadening mechanisms, building on the models adopted in prior studies. It demonstrates that exciton-free carrier interactions dominate collisional broadening in Ge, contrary to existing literature that proposed exciton-exciton interactions. The complete model is used to extract spectral parameters with low uncertainty from high-quality PL spectra of natural Ge.

The impact of various measurement conditions on PL is examined in Chapter 5. It addresses the contentious issue of power dependence in Ge PL and the influence of excitation wavelength. Based on comprehensive analysis, an explanation in terms of defect interactions is shown to satisfactorily account for the experimental data. The impact of excitation NA is then quantified using a diffusion model. The chapter concludes with a discussion of laser heating and an interesting phenomenon of PL enhancement caused by charge carrier localization.

Chapter 6 examines additional emission peaks observed in the Ge spectra beyond indirect phonon-assisted PL. These are demonstrated to originate from electron-hole droplets (EHD) and bound excitons (BE). Comparison with existing literature reveals that ^{76}Ge samples (in which BE peaks were measured) were unintentionally doped with phosphorus atoms.

Equipped with the experimental capabilities and PL models developed in preceding chapters, Chapter 7 presents a comprehensive analysis of indirect PL from isotopically-purified ^{72}Ge, ^{73}Ge, ^{74}Ge and ^{76}Ge. The data are compared to existing theoretical models and previously reported experimental results, demonstrating considerable improvement in measurement uncertainties. The inclusion of ^{72}Ge and ^{73}Ge isotopes provides a more complete picture, as these were absent from earlier studies. For the first time, absolute values of phonon energies are reported for the four aforementioned isotopes.

CHAPTER 2 EXPERIMENTAL METHODS

Germanium can be prepared with purity unattainable for most known materials, with recent studies reporting samples of 13N purity, that is 99.99999999999% [27]. This is desirable for applications which require high carrier mobility or quantum coherence but it makes photoluminescence measurements more challenging. Being an indirect gap semiconductor, intrinsic PL of Ge is weak and impurities often provide dominant radiative recombination channels.

Since the main subject of this thesis has been PL from high purity Ge, an efficient detection system was essential in obtaining data of intended quality. As such, much time and effort was devoted to optimizing the laboratory set-up and the experimental methods form an integral part of this thesis.

This chapter will briefly describe the Ge samples before examining the components of the experimental PL set-up. Particular attention was given to the superconducting nanowire single photon detectors (SNSPDs) due to a limited amount of specifications provided by the manufacturer. Finally, an extensive investigation into the alignment stability of the spectrometer output will be presented, as it turned out to be a pivotal aspect of the set-up efficiency. It will be shown how theoretical models were developed to understand this issue, leading to effective practical solutions.

2.1 Germanium samples

High purity single crystal germanium (Ge) samples discussed in this thesis were produced at the Institute for Crystal Growth (IKZ) in Berlin. They include natural Ge as well as four isotopically purified samples of ^{72}Ge, ^{73}Ge, ^{74}Ge and ^{76}Ge. The isotope separation was carried out through the centrifugal method using monogermane (GeH_4) molecules. Subsequently, impurities were removed using the process of low-temeprature rectification [28]. Ge was extracted through thermal decomposition of GeH_4 and then underwent further elemental purification using zone melting [29].

The resulting isotopic and elemental purity was assessed by the manufacturer using laser mass spectroscopy [29]. Concentrations of 66 analyzed impurities were below the sensitivity

threshold of 10^{-5} mass %, except for that of Si at 2×10^{-5} mass %. Isotopic purity was found to be in excess of 99.9% for ^{72}Ge, ^{73}Ge and Ge^{74}Ge. ^{76}Ge proved more challenging to isolate and contained a significant (>10%) admixture of ^{74}Ge nuclei.

Ge single crystals were grown using the Czochralski method in the $< 100 >$ crystallographic direction in the environment of high-purity argon. Since the seed used was made of natural Ge, the growth was carried out in two stages, in order to minimize the isotopic contamination of the target crystal. The ingots were cut into wafers and polished, the specific samples investigated in this work had the areas of 6×6 mm and the thickness of 0.5 mm.

Throughout the measurements, the samples were cleaned with a variety of solvents, including acetone, isopropyl alcohol, methanol, distilled water and water with soap, leading to no noticeable changes in behavior. No other surface treatments were undertaken which means that a layer of oxide can be expected to have been present on the samples.

Care was taken to study the homogeneity of the samples, so that PL measurements presented throughout this thesis were representative of the bulk Ge, rather than any local anomaly. Measurements were performed at least twice on different regions of the same sample to establish repeatability of results. Any non-reproducible trends were excluded from the overall body of work.

2.2 Experimental set-up

All spectra acquired in this work were collected using photoluminescence (PL) spectroscopy. The experimental set-up used in the course of the measurements is shown in Fig. 2.1. This section will describe its components and principles of operation.

Two laser sources were used for the vast majority of the measurements, namely a 532 nm Millenia manufactured by Spectra-Physics with a maximum power output of 15 W and a 1059 nm Cobolt manufactured by Hübner with a maximum output of 205 mW. Both were continuous wavelength sources based on Nd:YAG crystals with photon energies significantly higher than the direct energy gap in Ge (0.89 eV at 0 K, corresponding to $\sim$ 1400 nm). Their paths were combined with a cube 90:10 beam splitter (BS1) to allow a simultaneous illumination with both. Occasionally, two other light sources were used as well - a tunable

Ti:Sapphire Tsunami (used in CW mode) and a 633 nm HeNe laser.

Excitation power of the laser sources was controlled in three ways: 1) software-controlled current fed through the diode, 2) tunable neutral density (ND) filter and 3) an assembly of a polarizer and half-wave plate. An optional telescope was used to tune the beam width to match the entrance pupil of the objective.

A DMLP1180 dichroic mirror from Thorlabs (BS2) was then used to steer the beam into the sample chamber. The samples were illuminated through a NA0.42 IR objective (to prioritize focusing power and beam quality) or through a 250 mm achromatic doublet lens (to prioritize signal transmission). The samples were housed in a Montana X-plane cryostat which sustained cryogenic temperatures and high vacuum. The temperature of 4 K was not achievable at the sample holder but < 6 K temperatures were reached reliably. At high excitation power, significant laser heating was observed at the sample holder thermometer, with ΔT of > 1 K under the illumination of ~ 100 mW.

Two additional features were installed in the vicinity of the sample chamber. A CCD camera was used for sample imaging and integrated into the set-up with a removable pellicle beam splitter. A Ne spectral lamp was used for the spectral calibration of the set-up. The wavelength range of interest included a Ne line at 1716.2 nm and a number of higher order reflections, a typical calibration curve is shown in Fig. 2.2.

The signal was passed through a 1300 nm long pass filter to remove the laser reflection, before entering a HJY iHR550 spectrometer equipped with a 600 l/mm grating, the relative efficiency of which is shown in Fig. 2.3. The alignment of the spectrometer itself will be covered in depth in Section 2.5. The spectrometer output was coupled into one of two single-mode fibers which led to SNSPD detectors PS1 and PS2 which are discussed in detail in the upcoming section.

2.3 Spectral resolution

The resolution of the set-up was evaluated experimentally using a Ne spectral lamp. During the process, it was noted that the actual spectrometer slit widths w_{slit} did not necessarily match the nominal values set in the software. Due to the importance of the slits in determin-

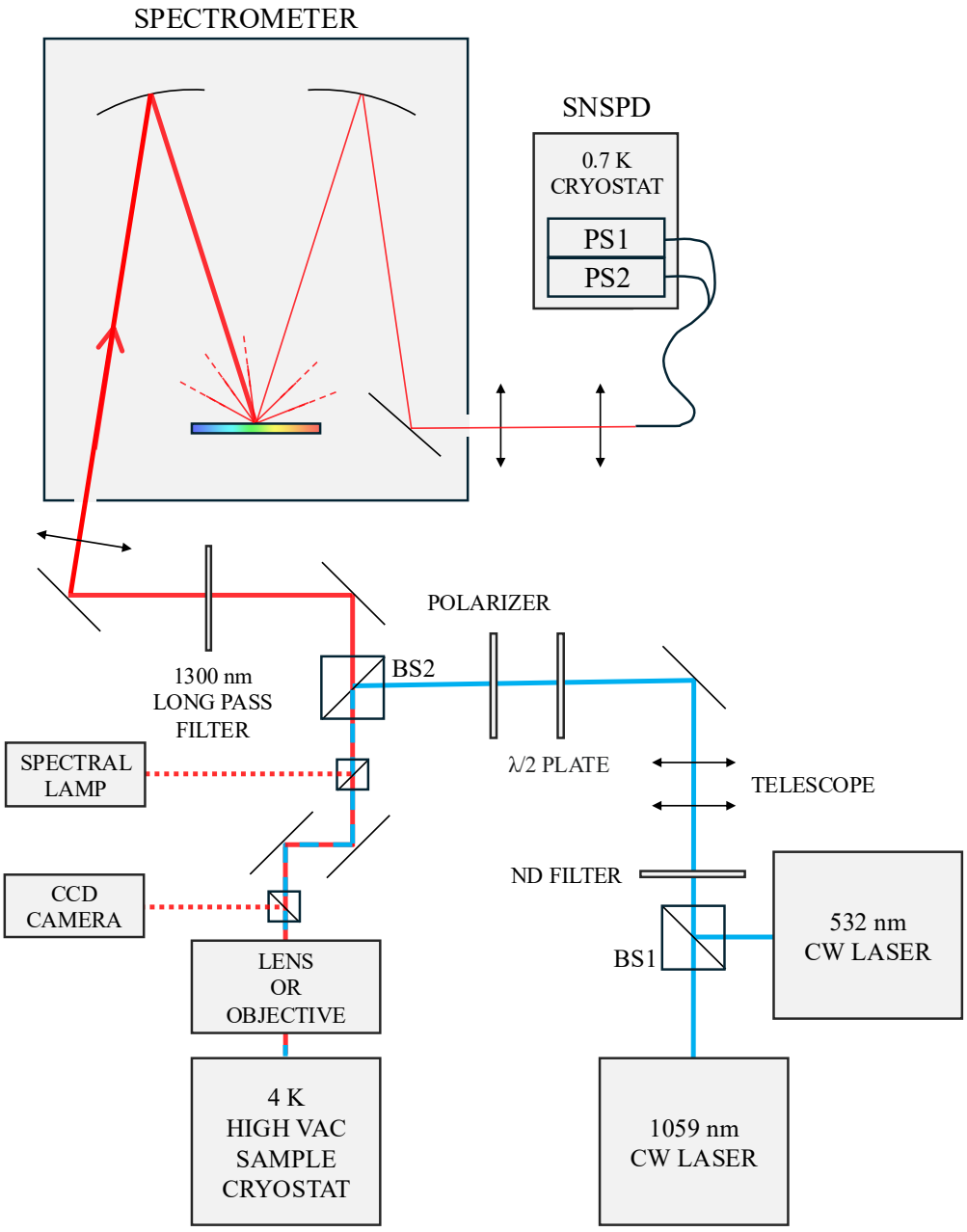

Figure 2.1 Schematic of the experimental set-up used for PL measurements. 532 nm and 1059 nm CW lasers (combined through a cube beam splitter BS1) were used for illumination, tunable ND filter and a $\lambda/2$ plate-polarizer assembly provided laser power control while an optional telescope adjusted the beam width to the entrance pupil of the objective. Dichroic mirror (BS2) steered the beam towards the sample chamber housed in a cryostat. Illumination and PL collection were carried out using a NA0.42 objective or a 250 mm lens. CCD camera was used for sample imaging and a Ne spectral lamp for calibration. The signal was passed through a 1300 nm long pass filter and a 550 mm spectrometer equipped with a 600 l/mm grating. Spectrometer output was coupled into a single-mode fiber with MFD $= 8\,\mu$m leading to a SNSPD detector (PS1 or PS2) housed in a cryostat with a sorption fridge capable of reaching sub-Kelvin temperatures.

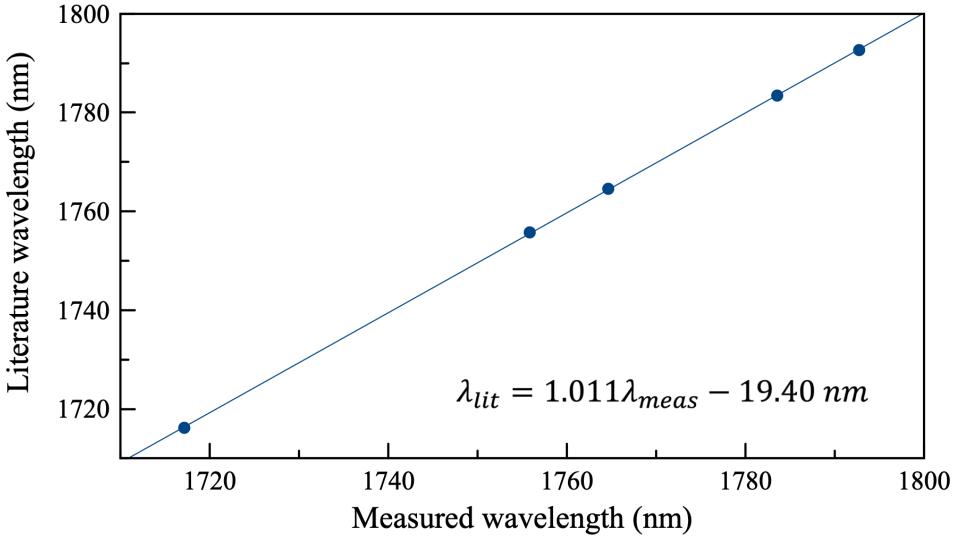

Figure 2.2 Typical spectral calibration curve obtained using emission lines from a Ne lamp. The uncertainty in λ following the calibration was 0.2 nm

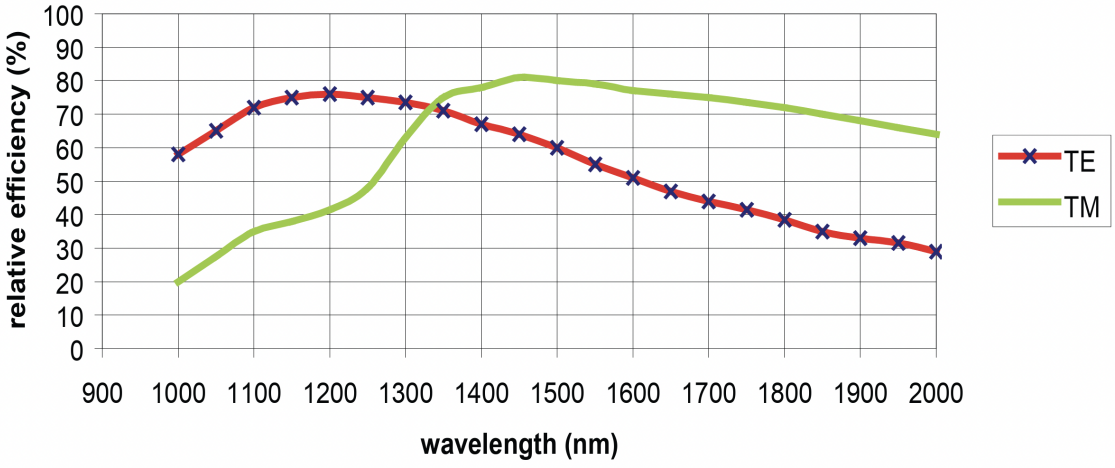

Figure 2.3 Relative efficiency of the diffraction grating for TE and TM polarization modes. It is normalized against the reflection off an Al surface. Figure reprinted from [30].

ing the resolution, calibration of w_{slit} was performed which is shown in Fig. 2.4. A laser beam was passed through the slit and the fringe separation of the resulting diffraction pattern was used as a linear measure of w_{slit}. It revealed an offset between the nominal and actual slit width values of 31 μm.

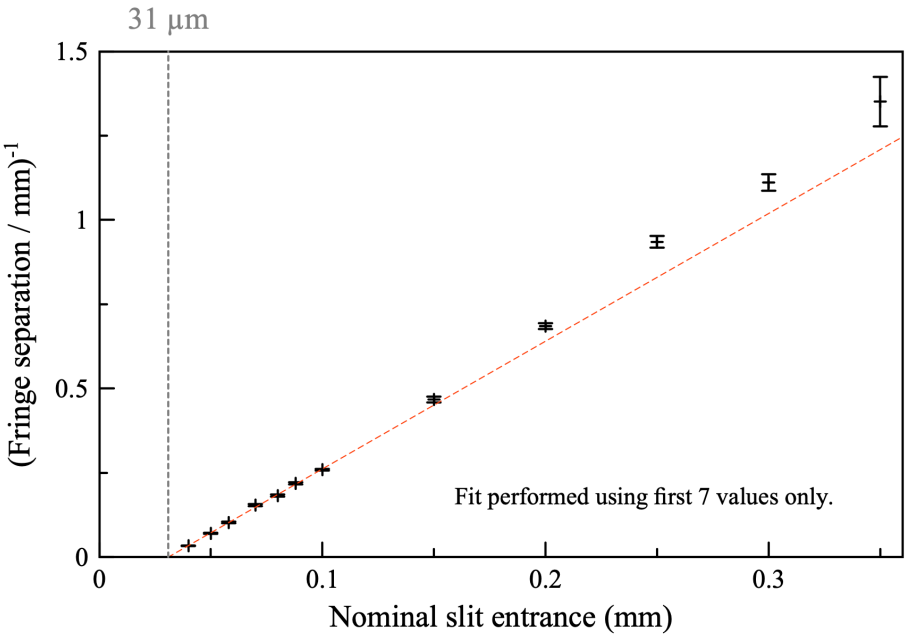

Figure 2.4 Calibration of the spectrometer slit width using the diffraction pattern of a laser passing through the slit. It revealed an offset of 31 μm between actual widths and those set in the spectrometer software.

The resolution of the set-up was found to be 0.20 ± 0.02 meV, by measuring the FWHM of a spectral line. Slits widths were decreased to the largest possible extent that did not significantly affect the beam profile. The measured value is an order of magnitude higher than the theoretical resolution of the spectrometer (0.021 meV, calculated from the manufacturer's specifications). The limiting factor was likely the spatial extent of the spectral lamp (or the sample in actual measurements) leading to off-axis signal.

2.4 SNSPDs

Signal detection was effectuated with two superconducting nanowire single photon detectors (SNSPDs) manufactured by PhotonSpot. The detector itself is a small superconducting circuit, into which a bias current is fed. The interaction with photons (which are delivered

to it via a fiber optic) causes the superconductive behavior to break down. The resulting increase in resistance leads to a spike in voltage across the circuit, which is then digitally amplified, recorded and added to the photon count.

SNSPDs are the most efficient detection technology for infrared light available on the market today. Table 2.1 compares their typical parameters [31] to those of photomultiplier tubes and avalanche photodiodes (SPADs), traditionally used in IR spectroscopy. Clearly, SNSPDs offer superior performance in regard to detection efficiency, noise mitigation and temporal resolution. However, they present an operational challenge as they require sub-Kelvin temperature for effective detection. This can be achieved by a cryostat equipped with a sorption fridge which uses evaporative cooling to extract heat beyond the liquid He temperature. As a result, the cost of an SNSPD assembly significantly exceeds the alternatives.

Table 2.1 Comparison of photodetector technologies commonly used in IR spectroscopy.

	Photomultiplier tube	**SPAD**	**SNSPD**
Detection Efficiency* (%)	~ 2	~ 10	> 90
Dark Count Rate** (s^{-1})	> 1000	> 50	~ 10
Jitter Time (ps)	> 300	$50 - 400$	$30 - 60$
Active Area	$> 1\,\text{mm}$	$> 40\,\mu\text{m}$	$< 10\,\mu\text{m}$
Operating temperature (K)	250	77	$1 - 2$

* At 1550 nm ** For SPADs, dark count rate is proportional to the active area.

Furthermore, embedding the detector inside a cryostat necessitates the use of fiber optic for photon delivery. In addition to alignment issues discussed in Section 2.5, this can negatively impact the PL yield, particularly in bulk PL measurements. Detectors with a large uniform active area can accommodate some off-axis signal emitted from the sample, as long as it passes through the experimental set-up. Fiber coupling rejects such off-axis contributions, akin to using a diffraction-limited pinhole. This is not an issue when a measurement resolves a single emitter, which is when SNSPDs truly excel.

Two detectors available for this project (PS1 and PS2) differed in the wavelength range for which they were designed. This is typically done not by altering the detector itself, but by filtering out some spectral contributions. The manufacturer did not provide efficiency curves which were needed to optimize set-up efficiency and correctly interpret experimental results.

Therefore, the detector performance was explicitly tested with a broadband light source. Fig. 2.5 shows normalized signal-to-noise ratio (SNR) for both detectors for different values of applied bias current. SNR was measured by normalizing the detector output against the emission curve of the light source and then dividing it by the square root of the dark count, representing the minimum level of the shot noise. It should be noted that this calculation method is only accurate for weak signals, as it ignores the shot noise in the signal itself. However, this is the most interesting regime as strong PL is easily detected, even if the set-up is not fully optimized.

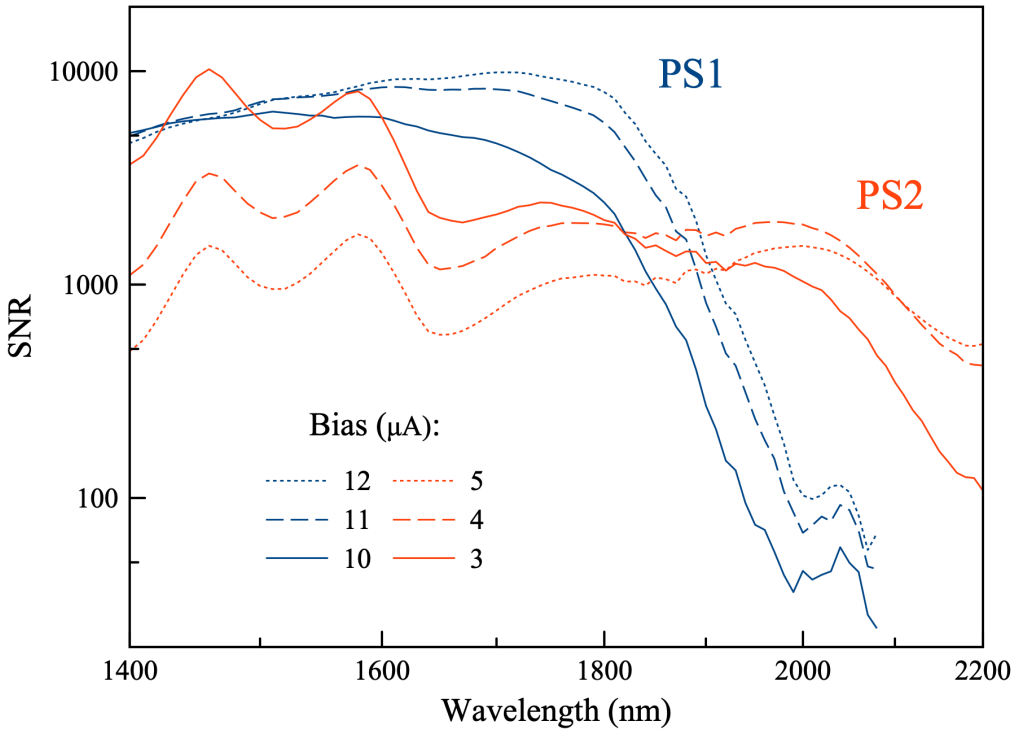

Figure 2.5 Spectral performance comparison of SNSPD detectors PS1 and PS2 for different values of applied bias current. SNR was calculated by normalizing the photon count against the emission curve of the broadband light source and dividing it by the square root of the dark count. Optimal operational ranges are $< 1800\,\text{nm}$ for PS1 and $1650 - 2100\,\text{nm}$ for PS2.

PS1 exhibits a high and relatively uniform SNR in the $1400 - 1800\,\text{nm}$ range, beyond which it rapidly falls off. This is because higher wavelength photons are filtered off, explaining this drop off as well as a low dark noise rate (PS1 is less affected by long wavelength photons or thermal noise). PS2 shows significant fluctuations in performance for $< 1650\,\text{nm}$, followed by a stable performance for $1650 - 2100\,\text{nm}$, albeit with a smaller SNR than PS1. This is

because of a higher dark count caused by allowing in more thermal photons. Regarding the fluctuations, they are a by-product of the design features which optimize the performance at higher wavelengths.

Another important aspect of using a SNSPD is choosing the optimal bias current I_{bias}. SNR was calculated (in a manner described above) for a range of I_{bias} values for a selection of wavelengths. The I_{bias} values which led to the highest SNR are shown in Fig. 2.6. They exhibit a linear dependence on λ up to the critical bias threshold I_{crit}. This corresponds to the I_{bias} value beyond which superconductive regime cannot be sustained.

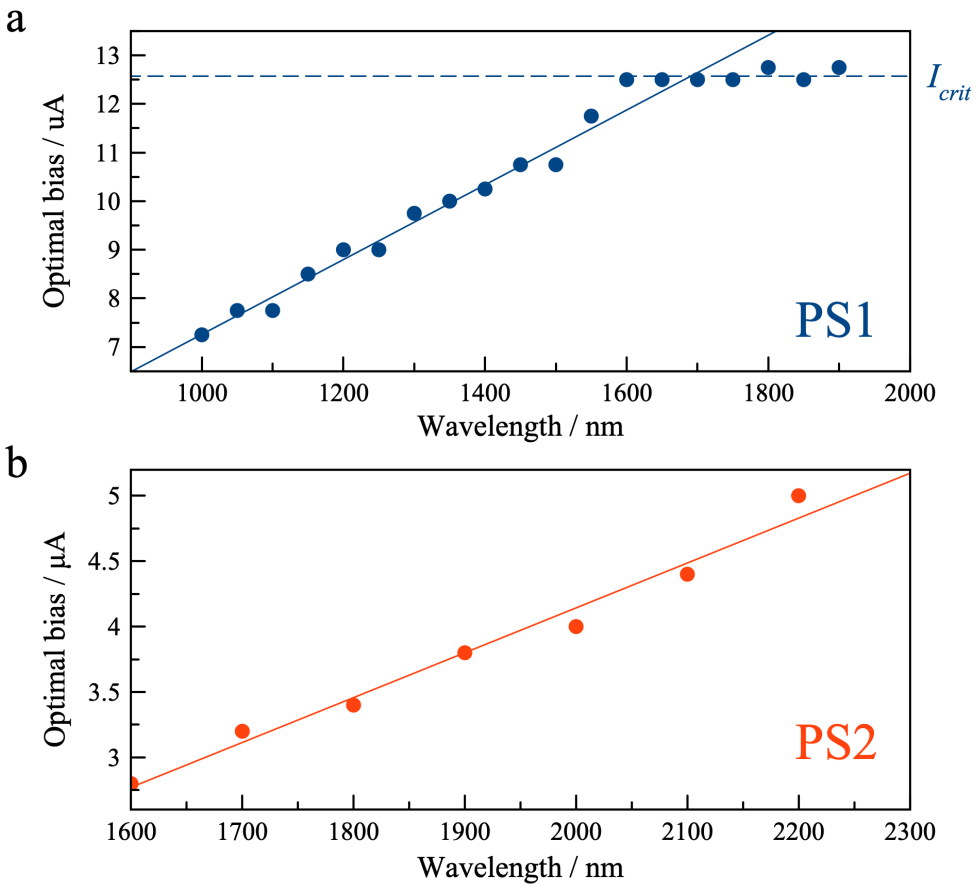

Figure 2.6 Optimal bias current I_{bias} of a) PS1 and b) PS2 for a selection of wavelengths. Optimal values were obtained by comparing SNR over a range of I_{bias}. I_{crit} corresponds to the value beyond which superconducting behavior can no longer be sustained.

Based on Fig. 2.5 alone, PS1 appears to be the preferred option for indirect PL from Ge,

which falls into the $1660 - 1780\,\text{nm}$ range. However, when coupling efficiency is considered in the light of provided fibers, available lenses and the diffraction limit at $\sim 1700\,\text{nm}$, the effective SNR turns out to be very similar for both detectors. PS2 was therefore chosen for the measurements presented in this thesis, as it ensured a more stable behavior (further from I_{crit}). It also allowed acquisitions further into the IR region, a factor potentially important for studying higher-order phonon replicas and other lower energy emission from Ge.

2.5 Spectrometer-induced shifts

This section discusses the problem of interfacing a diffraction grating-based spectrometer to a single mode fiber optic. It demonstrates how crucial it is for the detection efficiency, proposes theoretical models to understand the alignment stability of a spectrometer output and presents effective practical solutions.

2.5.1 Coupling efficiency

SNSPD used in this project employed a single-mode fiber optic for signal coupling, the mode field diameter (MFD) of which was $8\,\mu\text{m}$. Accordingly, very high alignment stability was necessary in order to maintain good signal collection across the entire spectral range of interest. Coupling efficiency η under a lateral displacement a of the signal with respect to the mode-field diameter (MFD) of the fiber can be quantified using an overlap integral:

$$\begin{aligned}\eta &= \frac{\left(\int_{-\infty}^{\infty} e^{-r^2/4w_1^2} e^{-(r-a)^2/4w_2^2} dr\right)^2}{\int_{-\infty}^{\infty} e^{-2r^2/4w_1^2} dr \int_{-\infty}^{\infty} e^{-2r^2/4w_2^2} dr} \\ &= \frac{4w_1 w_2}{w_1^2 + w_2^2} \exp\left(-\frac{a^2 w_1^2}{2w_2^2(w_1^2 + w_2^2)}\right)\end{aligned} \tag{2.1}$$

where w_1 and w_2 are the $1/e^2$ widths of the signal beam and MFD. Fig. 2.7 shows the drop-off in coupling efficiency as the signal beam and MFD become laterally misaligned. It was measured by recording PL signal from a Ge:Sb reference sample emitting at 1750 nm and displacing the detector fiber away from the optimal position. Fitting the data with Eq. 2.1 and assuming $w_1 = \text{MFD} = 8\,\mu\text{m}$ yields $w_2 = 8.4 \pm 0.1\,\mu\text{m}$, confirming successful NA matching. What is more pertinent to this section is the fact that a displacement a of only $14\,\mu\text{m}$ leads to 50% of the signal being lost. In order to limit the losses to $< 5\%$, lateral displacements must not exceed $\sim 3\,\mu\text{m}$.

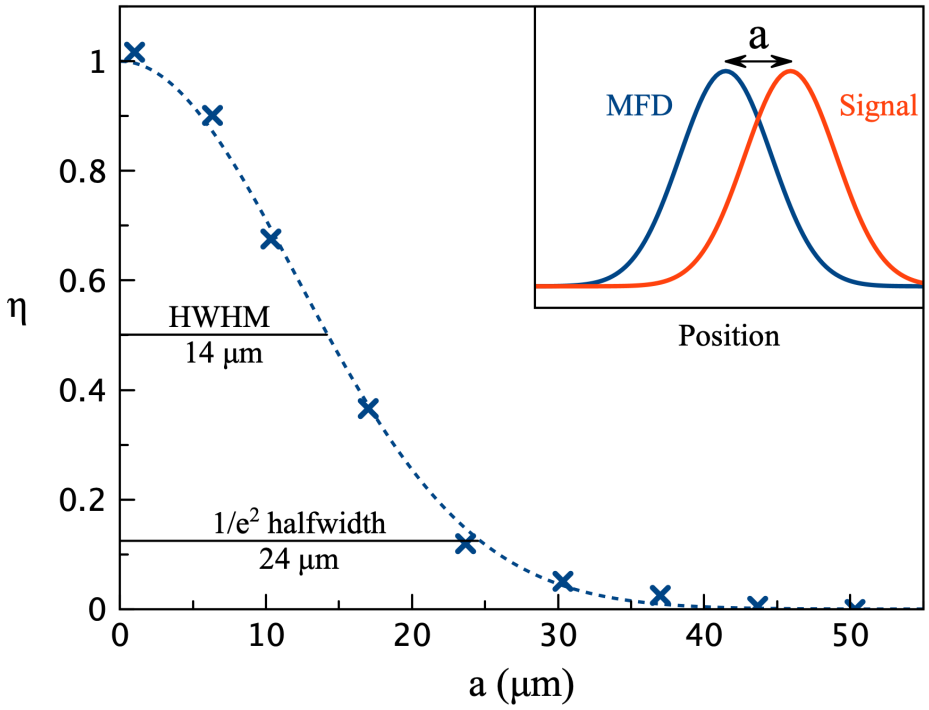

Figure 2.7 Coupling efficiency η drop-off with lateral misalignment a between the PL signal field and the mode field diameter (MFD) of the fiber. The data represent PL intensity from Ge:Sb at 1750 nm for different vertical offsets of the detection fiber. It was fitted using Eq. 2.1 which yielded the beam width of $8.4 \pm 0.1\,\mu$m. The inset shows a schematic representation of the overlap of two Gaussians with an offset a.

Standard diffraction grating-based spectrometers are not designed to maintain this degree of alignment stability as the grating rotates. Fig. 2.8 shows vertical shifts of the spectrometer output (in the plane of the detector) caused by the operation of the turret, i.e. scanning the output wavelength. The observed shifts exceed 100 μm and vary steeply in the range of interest (1650–1800 nm for indirect PL from Ge). This makes it impossible to perform broad spectral scans for which this experimental set-up was intended.

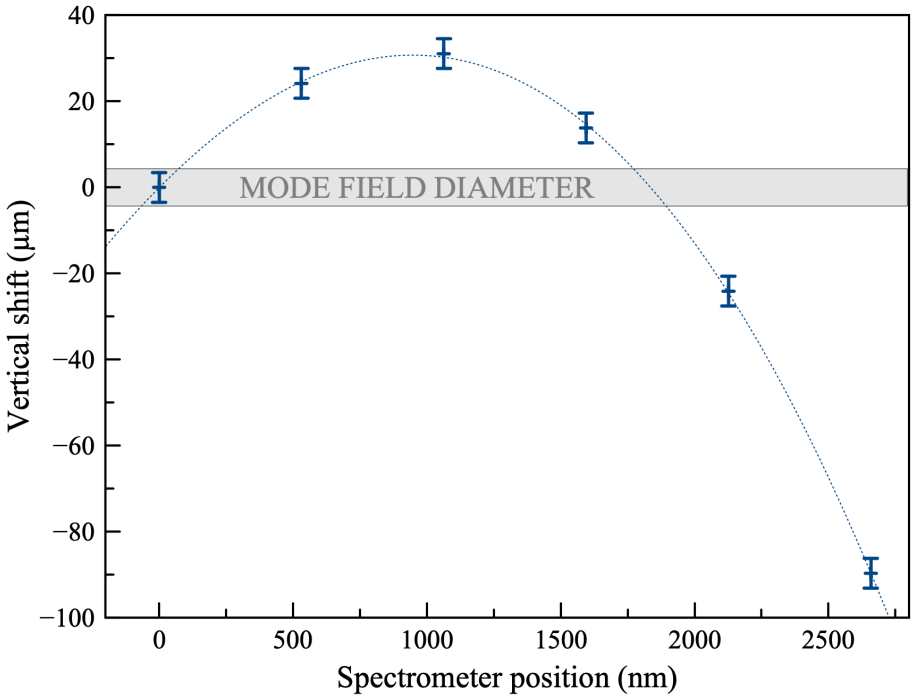

Figure 2.8 Vertical shifts of the signal beam recorded in the focal plane of the detector. The shifts caused by the spectrometer's operation vastly exceed the MFD of the fiber leading to an almost complete loss of coupling efficiency.

2.5.2 Modelization

In order to understand the origins of the walk-off problem and design a workable solution, a model was developed to quantify the influence of various degrees of freedom associated with the diffraction grating on the resulting vertical shifts in the detector's focal plane. Fig. 2.9 schematically shows the most important grating alignment parameters discussed in this section. They include translational displacement Δx away from the rotation axis, angles α_{ROLL} and α_{TILT} as well as θ - the angular position of the grating turret.

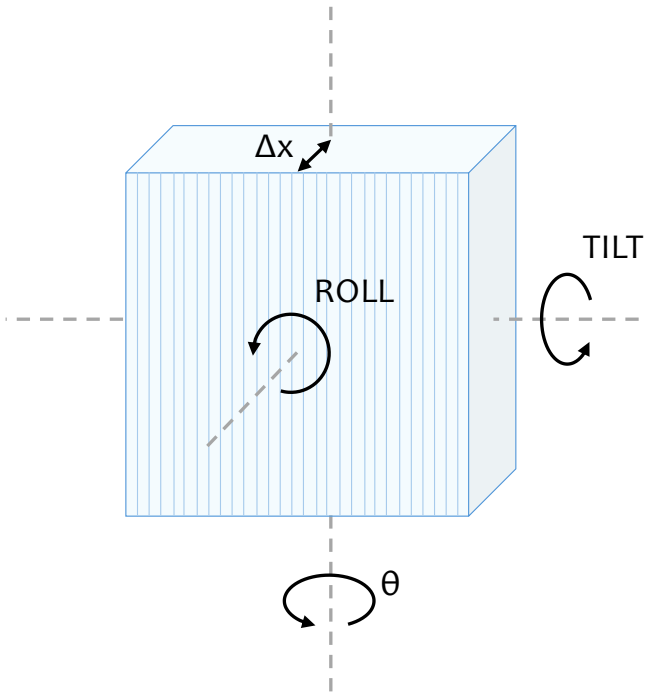

Figure 2.9 Schematic of important degrees of freedom in the alignment of a diffraction grating.

Consider a ray of light reflected off of the grating with a non-zero vertical slope relative to the optical axis of the experimental set-up. Its subsequent path, described in this paragraph, is shown schematically in Fig. 2.10 and constitutes the starting point for understanding the impact of α_{ROLL} on the alignment stability. The ray continues traveling at a constant angle until it reaches the 2^{nd} focusing mirror (see Fig. 2.1 for the top view of the relevant optical components). The mirror performs a Fourier transform on the beam profile, converting the slope into a lateral shift. To first order, this make the ray parallel to the optical axis at an elevated (or lowered) height. The two lenses after the spectrometer then act as a telescope which simply scales the shift size. Therefore, grating-induced slope is translated into a vertical shift in the plane of the detector.

Roll of the grating

Roll of the grating α_{ROLL} is the angle that the grooves of the grating make with the vertical axis (defined by the optical plane of the experimental set-up). This means that α_{ROLL}

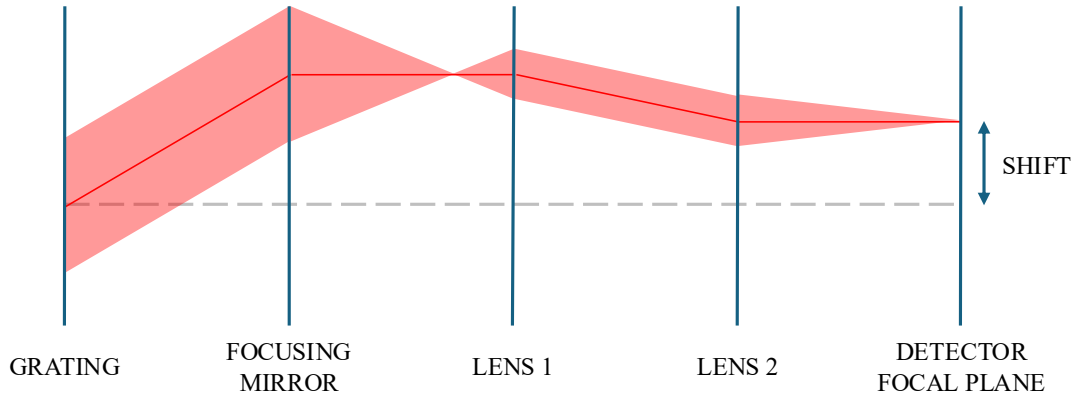

Figure 2.10 Path taken by a beam reflected off of the grating at an angle w.r.t. the optical axis. The initial slope leads to an eventual shift in the focal plane of the detector.

determines the plane in which all light diffracted off of the grating will be contained. For $\alpha_{\mathrm{ROLL}} = 0$ this plane will be horizontal, while for $\alpha_{\mathrm{ROLL}} = 90°$ it will be vertical. The slope of the reflected beam is therefore proportional to $\sin(\alpha_{\mathrm{ROLL}})$ and will increase linearly in $\sin\theta$.

In order to explicitly verify the above reasoning, ray paths were measured inside the spectrometer with a CCD camera. Specifically, beam height was recorded at two different distances from the grating. Fig. 2.11 shows the slope of the reflected beam as a function of θ. The collected data is in agreement with the $\sin\theta$ dependence and reveals a non-zero $\sin(\alpha_{\mathrm{ROLL}})$.

The beam path discussed earlier and shown in Fig. 2.10 demonstrates that, within the paraxial approximation, the resulting shift a_{ROLL} in the detector's focal plane is proportional to the initial slope. The impact of α_{ROLL} can therefore be expressed as:

$$a_{\mathrm{ROLL}} \propto \sin(\alpha_{\mathrm{ROLL}}) \sin\theta. \tag{2.2}$$

Displacement Δx

Spectrometers are designed in such a way that the rotation axis of the turret passes through the surface of the grating. This way, the central point of reflection remains stationary as the

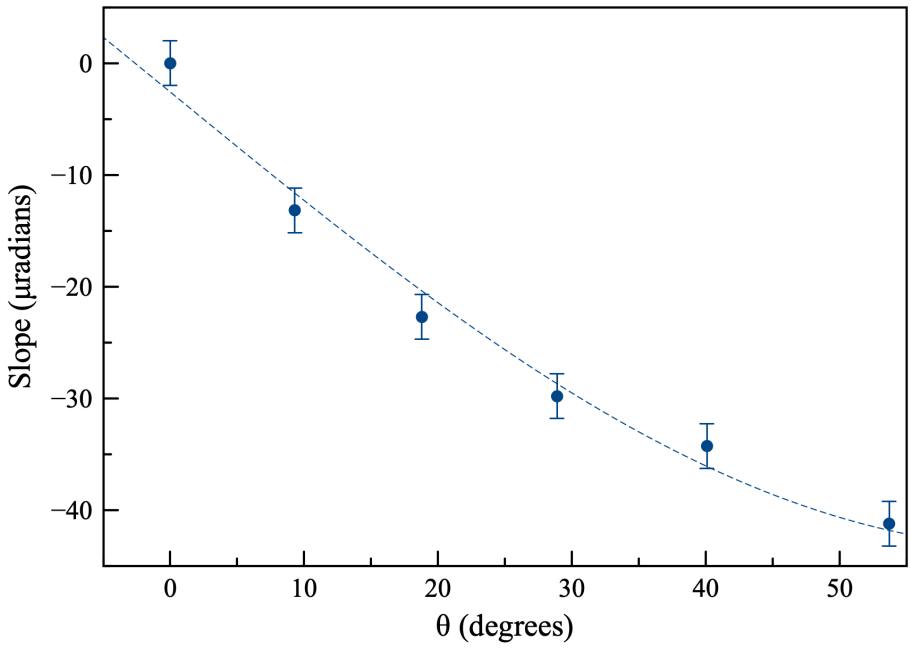

Figure 2.11 Slope of the beam reflected off of a grating as a function of θ. Each data point corresponds to the n$^{\text{th}}$ order reflection of the 532 nm laser. Dashed line represents a sine fit.

grating rotates [32]. This can only be true for one unique position of the grating, defined here as $\Delta x = 0$. If it is translated forwards or backwards from this ideal position, the reflection position moves, affecting the reflected beam trajectory. Fig. 2.12a shows the correct alignment and Fig. 2.12b shows the effect of non-zero Δx.

It is not straightforward to fully model this effect as it does not result in a simple change in the slope, as was the case with the roll of the grating. The exact ray geometry is strongly dependent on the angle and positional coordinates of the incoming beam. Still, within the paraxial approximation, it is reasonable to assume that, to first order, all shifts will be proportional to the shift in the point of reflection on the grating. Fig. 2.12c shows a schematic derivation of its θ- and Δx-dependence. Based on the above assumptions, the vertical shift in the focal plane of the detector should obey:

$$a_{\Delta x} \propto \Delta x \sec\theta \tag{2.3}$$

Data used to calculate slopes in Fig. 2.11 was extrapolated to estimate the position of the reflection point on the grating. The results of this calculation are shown in Fig. 2.13. High

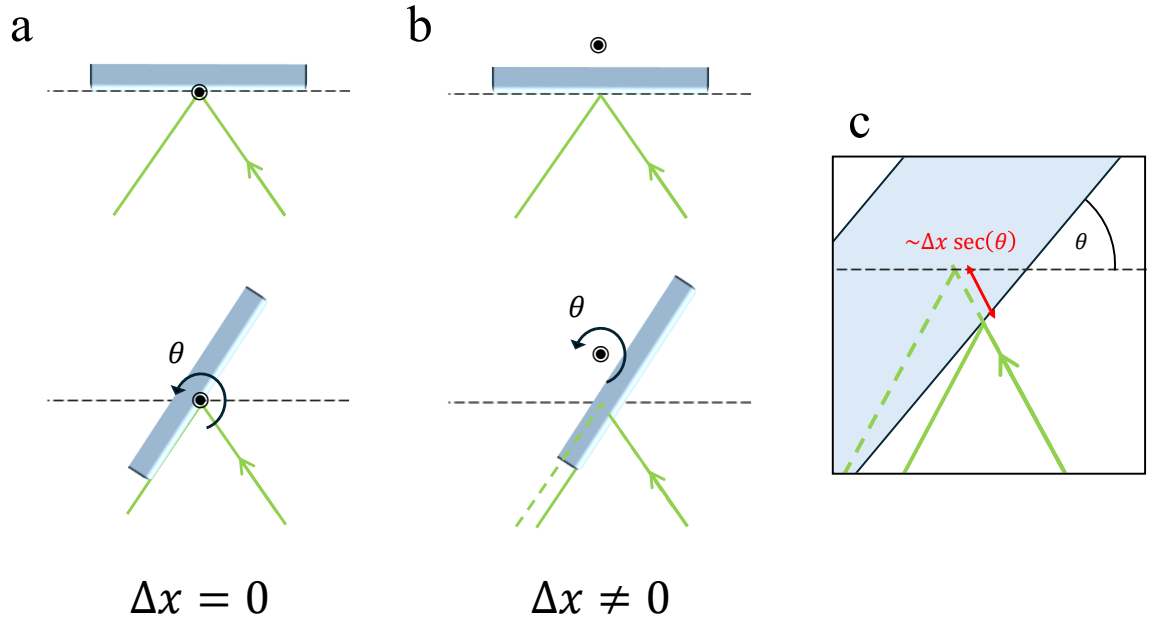

Figure 2.12 Schematic showing a a) correctly and b) incorrectly aligned Δx of a diffraction grating. The derivation of Eq. 2.3 is shown in c).

uncertainties stem from the extent of extrapolation as well as a relatively small scale of the translation of the reflection point (it is proportional to the vertical slope of the incoming beam which is almost eliminated in the alignment process). Still, thanks to the highly non-linear nature of the secant function, the data supports the proposed model in a statistically significant way.

Tilt of the grating

In itself, the tilt of the grating α_{TILT} does not induce any offset a, as its effect is uniform for all angles θ. In practice, depending on the turret design, tilting the grating may simultaneously change the displacement Δx. This happens if the rotation axis of α_{TILT} is near the top, or the bottom of the grating. In such a case, tilt control can be used as a precise way to fine tune Δx.

Angular orientation of the rotation axis

One other alignment aspect which must be considered is the alignment of the rotation axis of the grating turret. The angular orientation of the axis is defined by two angles (with respect

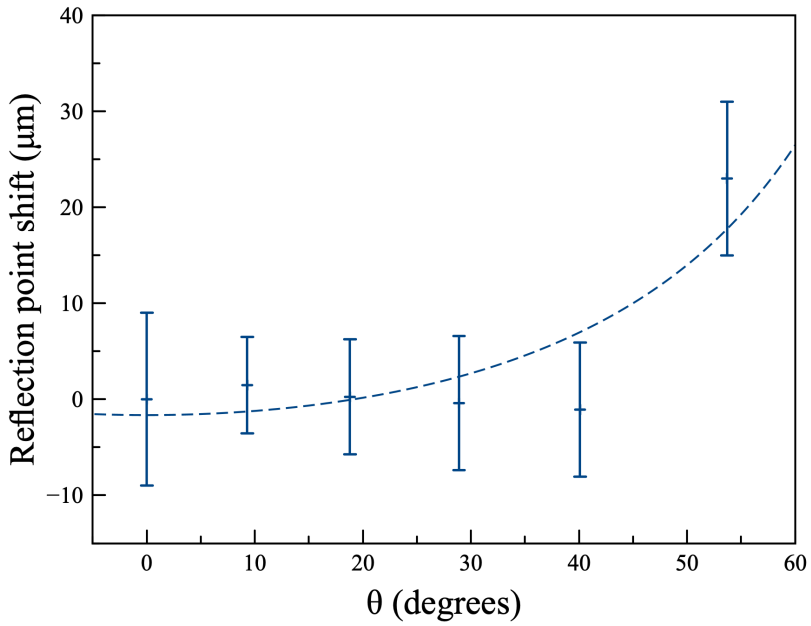

Figure 2.13 Shift in the reflection point on the grating induced by Δx. Dashed line shows a secant fit.

to the vertical) which will be referred to as α_1 and α_2. α_1 is shown in red in Fig. 2.14. If α_1 or α_2 are non-zero, α_{ROLL} and Δx are induced in a highly non-linear fashion. Fig. 2.14 shows schematically how θ-dependent roll arises from a skewed rotation axis. Based on the aspects of the model hitherto demonstrated, a simple trigonometric derivation leads to:

$$a_{\alpha_{1,2}} \propto A \sin(\alpha_1)(\sin\theta)^2 + B \sin(\alpha_2) \sin\theta \sec\theta \tag{2.4}$$

Eq. 2.4 adds a significant level of complexity into the picture. Fortunately, it is straightforward to correct this alignment aspect independently of other degrees of freedom. The procedure for this correction will be discussed in the upcoming Section 2.5.3 and is a necessary step in eliminating the vertical shifts a.

Full model

In light of the above considerations, and assuming that the rotation axis is well aligned, vertical shifts in the plane of the detector can be modelled as:

$$a_{\mathrm{total}} = A \sin(\alpha_{\mathrm{ROLL}}) \sin\theta + B\Delta x \sec\theta, \tag{2.5}$$

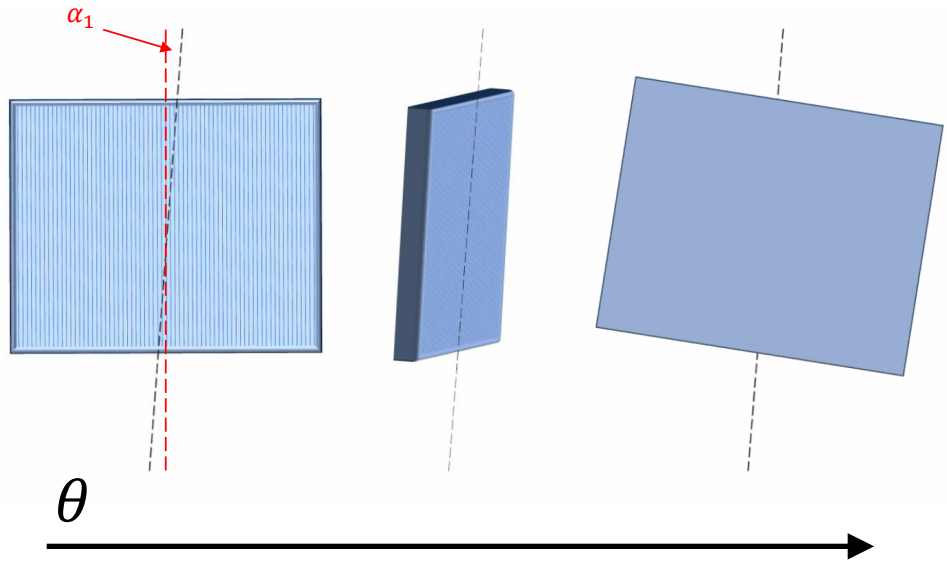

Figure 2.14 θ-dependent roll of the grating induced by the misalignment of the rotation axis.

where A and B are constants dependent on the specifications of optical elements used in the experimental set-up.

2.5.3 Implementation

Rotation axis alignment

Before the alignment of the grating on the turret could be considered, the turret alignment with respect to the optical table was addressed to avoid complications due to non-zero $\alpha_{1,2}$ described earlier. This was achieved by applying the following procedure:

- Mount a mirror on top of the diffraction grating turret
- Illuminate the mirror with a horizontal laser beam of known height h
- Select two θ positions of the turret and two diagonally opposite legs of the spectrometer
- Alternating between the two θ values, adjust leg heights so that the height of the reflected beam matches h
- Iterate until convergence

Shift modeling

Fig. 2.15 shows actual shifts (relative to the 0^{th} order reflection of a 532 nm laser beam) measured by placing a CCD camera in the detector's focal plane. Each curve was measured for a different value of Δx which was controlled by adjusting α_{TILT} (turret design did not allow a direct control of Δx).

The data is well modeled by Eq. 2.5 and coefficient B extracted from the fits is linear in Δx, further validating the model. The fit parameters allow to estimate the required alignment accuracy to limit losses to $< 5\,\%$ which corresponds to shifts within $3\,\mu$m. For the experimental set-up used in this work, the alignment resolution of 0.01ř for α_{ROLL} and $50\,\mu$m for Δx were needed, well beyond the capabilities of the original turret (0.07ř to 0.3ř with no translational control).

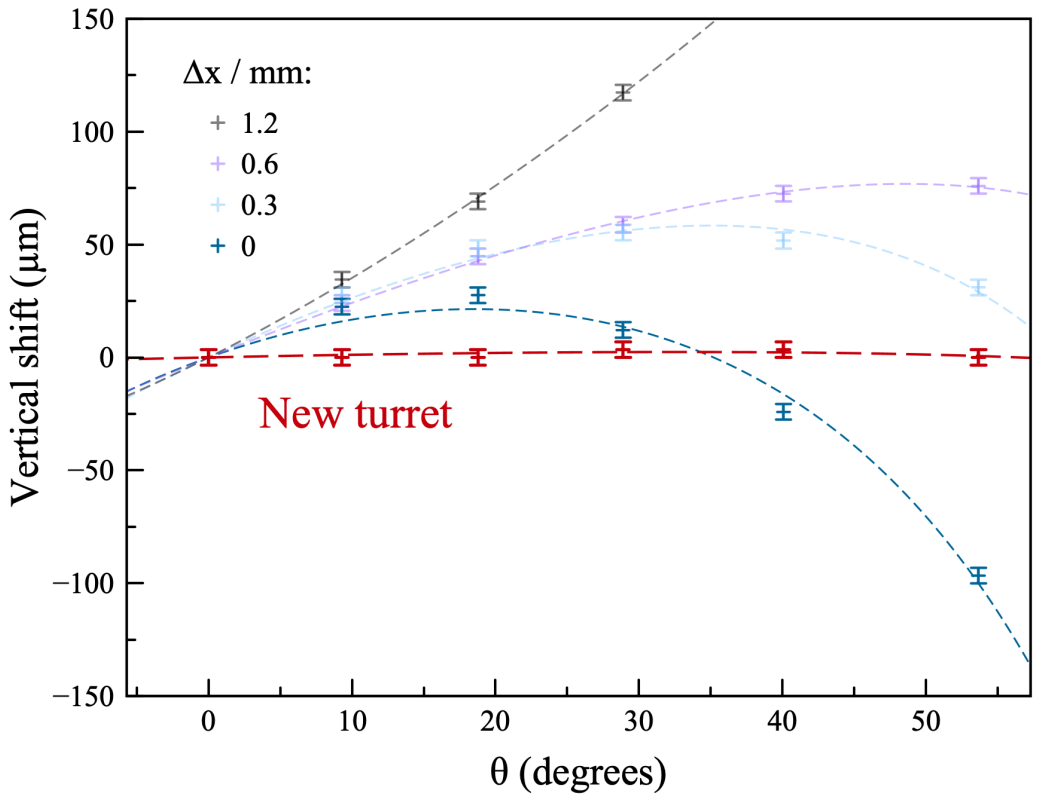

Figure 2.15 Spectrometer-induced vertical shifts of the signal beam in the focal plane of the detector. Δx values were controlled by tweaking α_{TILT} of the grating. The data is successfully modeled by Eq. 2.5. Elimination of vertical shifts by the new turret is shown in red.

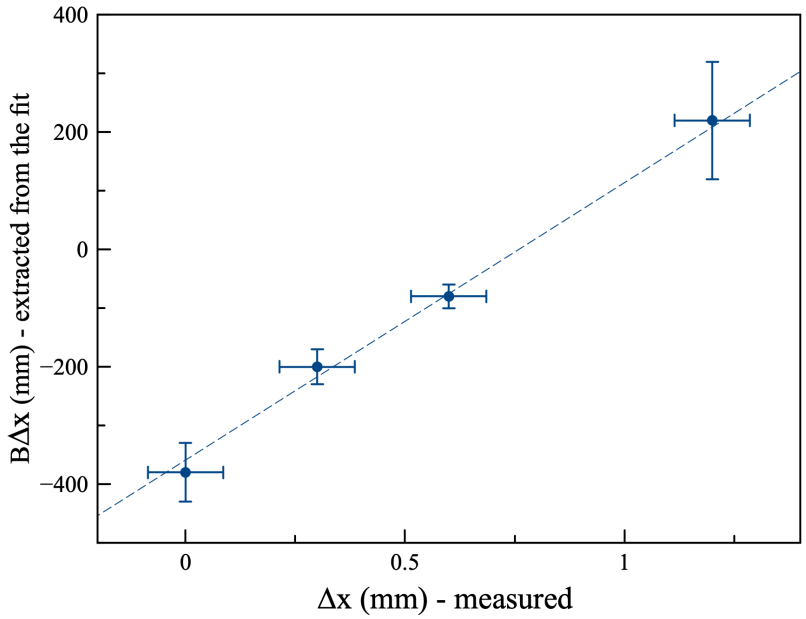

Figure 2.16 Coefficient BΔx (extracted from Fig. 2.15 fit using Eq. 2.5) compared to set values of Δx. Linear relationship provides a strong validation of the model.

New turret

In order to eliminate the shifts, a new turret was designed (Fig. 2.17) with differential micrometer screws which provided sufficient alignment precision.

An alignment procedure was devised for the grating based on Eq. 2.5. It relies on the fact that $\frac{d \sin\theta}{d\theta}$ is largest for small θ while $\frac{d \sec\theta}{d\theta}$ increases towards $\theta = 90$ř, which allows to correct the two degrees of freedom almost independently. The specific steps taken were as follows:

- Send a 532 nm laser through the spectrometer,
- Mount a CCD camera in the focal plane of the detector to monitor shifts,
- Use 0^{th} and 1^{st} order reflections to eliminate roll (by eliminating a relative vertical shift between them),
- Use 0^{th} and 5^{th} order reflections to eliminate Δx,
- Iterate if necessary.

Figure 2.17 New turret design.

Fig. 2.15 shows (in red) data acquired with the new turret after performing the above alignment procedure. Vertical shifts were within $3\,\mu$m across the entire available spectral range. This is sufficient to limit the losses due to spectrometer-induced shifts to $< 5\,\%$. It is also of similar magnitude to the observed jitter due to vibrations (also $\sim 3\,\mu$m, observed in real time using a CCD camera).

2.5.4 Astigmatism

Other than through inducing lateral shifts, spectrometer can also adversely affect coupling efficiency by causing astigmatism [33]. The primary source of this effect is the grating itself and the standard method of correcting for it is through the elliptical shape of the second focusing mirror. However, the extent of astigmatism correction depends not only on the mirror's ecentricity but also on the position of the reflection.

Our system suffered from significant astigmatism when the optical axis was aligned with the center of the 2$^{\text{nd}}$ focusing mirror. Fig. 2.18a shows the offset between the focal points of the laser beam for horizontal and vertical beam widths. To obtain the FWHM values, the beam was recorded with a CCD camera (with the pixel size of $3.6\,\mu$m) and the resulting image was fitted with a Gaussian. The astigmatism was evaluated by displacing the lens installed at the output of the spectrometer, rather than displacing the CCD camera in the detector's focal

plane. This second, more intuitive approach was not possible due to mechanical constraints related to the casing of the CCD camera.

In any case, astigmatism was successfully eliminated by selecting a correct reflection position on the 2nd focusing mirror, which was about 1 cm horizontally off-center. This is evidenced by the overlap seen in Fig. 2.18b, recorded after the correction took place.

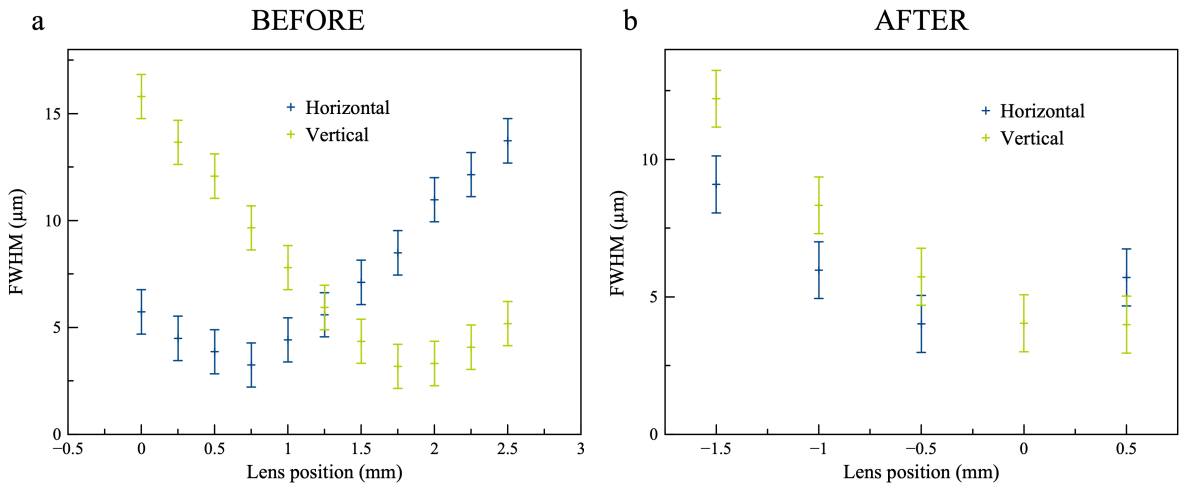

Figure 2.18 Focus scan of vertical and horizontal signal beam widths a) before and b) after the astigmatism correction.

2.6 Conclusions

Multiple aspects of the experimental set-up used in this thesis were investigated in considerable detail. The optimization of alignment techniques and the advanced understanding of the behavior of individual components greatly enhanced the quality of the photoluminescence data presented in subsequent chapters. Many of the subtle aspects of Ge PL could not be successfully demonstrated with an inferior detection system.

Solving the problem of spectrometer-induced shifts in alignment was of particular consequence due to the severity of the underlying issue. It allowed broad spectral scans crucial to this work as well as other projects carried out using the same set-up. It is also notable due to the technical simplicity of the devised solution which addressed the fundamental nature of the problem rather than resorting to more complicated schemes of active alignment control.

The vertical shifts in the focal plane of the detector were reduced from $> 100\,\mu$m, originally provided by the manufacturer, to $< 3\,\mu$m, representing a vast improvement in performance.

CHAPTER 3 THEORY

Before experimental results in this thesis can be discussed, it is vital to introduce three theoretical models. They form the basis for the interpretation of data shown in subsequent chapters and will be referred to frequently. Firstly, this chapter will present the derivation of the theoretical spectral lineshape for phonon-assisted radiative recombination. The resulting equations will be the starting point for modeling all spectra acquired in this work. Secondly, the theory of collisional broadening will be discussed based on the Weisskopf model. It will be explained how collisions manifest themselves in Lorentzian broadening of spectral features. Thirdly, the power dependence of PL will be discussed based on works by Schmidt et al. [25] and Spindler et al. [26]. It will be demonstrated how power exponents can be used to obtain valuable information about radiative and non-radiative processes undergone by charge carriers in semiconductors.

3.1 Theory of phonon-assisted PL

Germanium is an indirect band gap semiconductor in which the dominant radiative process is phonon-assisted photoluminescence. It is shown schematically on the band diagram in Fig. 3.1. An electron in the L valley and a hole in the Γ valley recombine radiatively while a phonon is emitted (or absorbed) in order to compensate for the momentum mismatch.

Four phonon modes are available: longitudinal acoustic (LA), longitudinal optical (LO), transverse acoustic (TA) and transverse optical (TO). Phonon dispersion diagram is shown in fig. 3.2. Comparing their symmetries (at L-valley minimum) to symmetries of relevant electronic states yields selection rules; it turns out that only LA- and TO-assisted transitions are allowed. PL due to forbidden LO- and TA-assisted recombination can still be observed (due to non-zero higher order matrix elements) but their intensity is significantly lower.

3.1.1 Selection rules for phonons

Let us consider the selection rules in more detail within the framework of group theory. The electronic wavefunctions at the L-point transform according to the D_{3d} point group. The hole wavefunctions are more complex due to the spin-orbit (s-o) interaction which splits the 6-fold degenerate valence band maxima into 3 doublets [34]. They include light and heavy hole bands separated by a small splitting of around 1 meV, as well as a split-off band which is

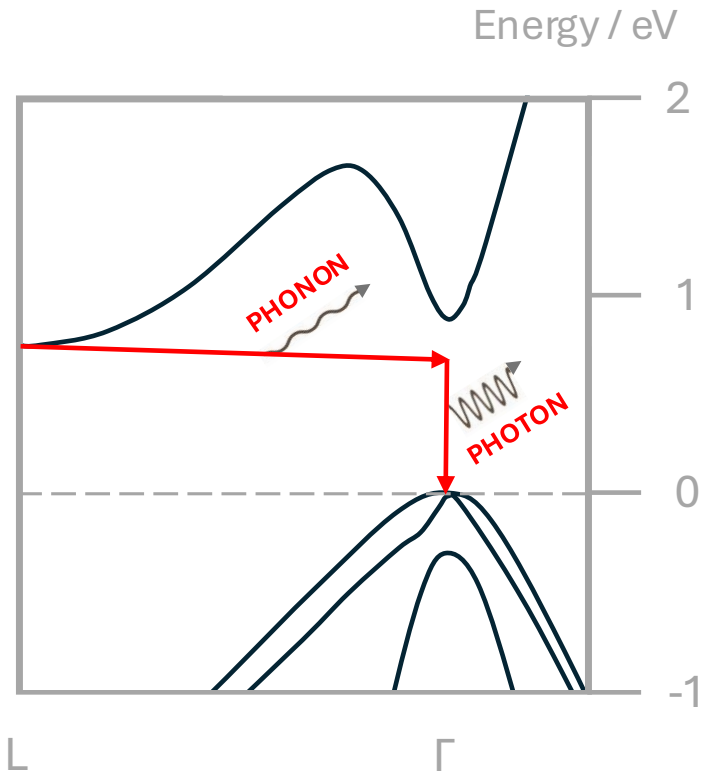

Figure 3.1 Ge band diagram schematically showing indirect phonon-assisted radiative recombination. L-valley electrons and Γ-valley holes recombine in a two-step process which involves emitting a phonon and a photon.

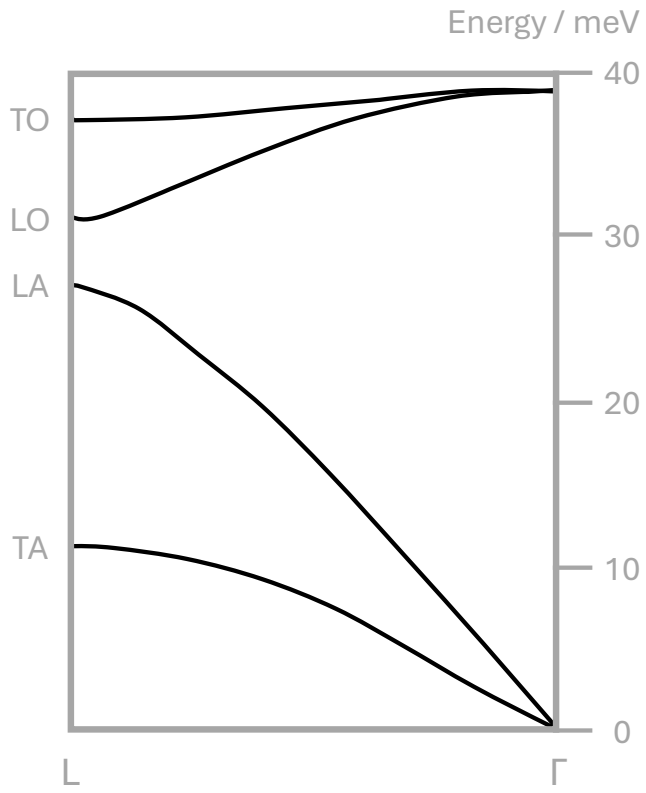

Figure 3.2 Phonon dispersion diagram for Ge. Dispersion data from [5].

at a much higher energy and will be ignored in the following analysis. The $\sim$1 meV splitting will be explicitly included in the modeling of the lineshapes of Ge PL in Chapter 4. For indirect electron-hole pairs, the exchange interaction is very small [35] which means they can be considered effectively spinless and the single group representation can be used. The resulting single group representations for electrons and holes are shown in Tab. 3.1, together with the representations for the four phonon modes, the electron-phonon Hamiltonian $\hat{H}_{e-p}$ and the electric dipole operator $\vec{p}$.

Table 3.1 Single group representations of relevant particles and Hamiltonians in Ge.

Γ_i	Entity	D_{3d} representation
Γ_e	electron	A_{1g}
Γ_h	hole	$A_{1g} + E_g$
Γ_{TA}	TA phonon	E_g
Γ_{LA}	LA phonon	A_{2u}
Γ_{LO}	LO phonon	A_{1g}
Γ_{TO}	TO phonon	E_u
Γ_{e-p}	$\hat{H}_{electron-phonon}$	A_{1g}
Γ_p	electric dipole operator	$A_{2u} + E_u$

The matrix element for a phonon-assisted indirect transition is:

$$\langle \mathrm{f} \,|\, \vec{p} \,|\, \text{phonon} \rangle \langle \,\text{phonon}\, |\, \hat{H}_{e-p} \,|\, \mathrm{i} \,\rangle.$$

In order for the transition to be allowed, the product of all involved representations must include A_{1g}:

$$\Gamma_e \times \Gamma_p \times \Gamma_{phonon} \times \Gamma_{e-p} \times \Gamma_h \supseteq A_{1g}. \tag{3.1}$$

$\Gamma_e \times \Gamma_p \times \Gamma_{e-p} \times \Gamma_h$ has odd parity, which means that only transitions assisted by phonons of odd parity are allowed, namely LA and TO. LO and TA have even parity which means that they are forbidden to first order.

This analysis can be extended to higher-order effects, such as electron scattering between the L- and Γ-valley minima. It turns out that this process is only allowed for LA phonons [36],

which helps to explain why LA-assisted PL is the dominant radiative transition in Ge.

3.1.2 Spectral intensity lineshape

In 1957, R. J. Elliott derived the spectral dependence of optical absorption by excitons in semiconductors [37], establishing a foundational framework for understanding excitonic transitions. While absorption and photoluminescence involve opposite processes (absorption creates excitons while PL involves their radiative recombination) both transitions occur between the same quantum states and therefore share identical transition matrix elements and density of states. This connection enables Elliott's formalism to be directly adapted to modeling photoluminescence spectra [38].

The general expression for phonon-assisted PL intensity in an indirect semiconductor can be written as:

$$I_{PL}(E) \propto \int |M_{cv}|^2 \times \text{JDOS}(E) \times (1 - f_c) f_v \times (N_q + 1) \times \delta(E_c - E_v - \hbar\omega - \hbar\omega_q) d\vec{k}, \quad (3.2)$$

where:

- M_{cv} is the transition matrix element,
- JDOS(E) is the joint density of states for electron-hole-phonon system,
- $(1 - f_c)$ is the probability that a conduction state is occupied,
- f_v is the probability that a valence state is available, and
- $(N_q + 1)$ is the phonon occupation factor.

This expression encompasses all the physical processes involved in indirect PL and forms the starting point for the detailed analysis of each component that follows. Since the objective of this thesis is to analyze spectra resolved in phonon energy, the terms with explicit energy dependence will be of primary interest.

3.1.3 Interaction Hamiltonian

Transition matrix elements are calculated using the interaction Hamiltonian for indirect photoluminescence. It needs to account for two phenomena, namely electron-photon and

electron-phonon coupling.

Electron-Photon The full Hamiltonian for an electron in an electromagnetic field is

$$H = \frac{e}{2m_e}\left(\widehat{p} - e\widehat{A}\right)^2 - e\phi,$$

where $\widehat{p}$ is electron momentum while $\widehat{A}$ and ϕ are vector and scalar potentials of the field. Expanding the squared bracket, subtracting the unperturbed Hamiltonian, setting $\phi = 0$ (Coulomb gauge) and only keeping terms linear in A (thus ignoring multiphoton processes) we arrive at

$$H_1 = \frac{e}{m_e}\widehat{A} \cdot \widehat{p}.$$

Electron-Phonon Phonon deformation potential is a standard measure of the coupling between electrons (holes) and phonons. It quantifies how electronic bands shift in energy when the material is mechanically strained. The relevant Hamiltonian is:

$$H_2 = D_i \nabla u_i,$$

where D_i is the deformation potential constant and ∇u is the strain field.

Full matrix element is then calculated through:

$$|M_{cv}|^2 = \left|\left\langle f \left| \widehat{H_1} + \widehat{H_2} \right| i \right\rangle\right|^2. \tag{3.3}$$

Depending on the symmetry properties of the phonon involved, parity selection rules may or may not be satisfied, leading to allowed (LA and TO) and forbidden (LO and TA) transitions. For the former, eq. 3.3 is well approximated by the leading term in the energy expansion which is independent of energy. For forbidden transitions that term is zero and higher order terms must be considered. Assuming that the first-order term is non-zero, the square of the matrix element is proportional to E. Hence, there will be an additional factor of E in the lineshape function for a forbidden transition, relative to an allowed one.

Other than the selection rules, $\widehat{H_2}$ also determines the relative emission intensities associated

with different phonons. Deformation potential values can explain why two allowed transitions may lead to very different PL intensities.

3.1.4 Joint Density of States

PL transition in an indirect gap semiconductor involves an electron, a hole and a phonon. Joint density of states must therefore include contributions related to all three. The starting point is to use integration to count all states that satisfy energy and momentum conservation:

$$JDOS(E) = \frac{1}{8\pi^3} \iint \delta(E_c(\vec{k_c}) - E_v(\vec{k_v}) \pm E_{ph}(\vec{q}) - \hbar\omega)\delta(\vec{k_c} - \vec{k_v} - \vec{q})d\vec{k_c}d\vec{k_v},$$

where $E_c(\vec{k_c})$ and $E_v(\vec{kv})$ are the conduction and valence band energies respectively, $E_{ph}(\vec{q})$ is the phonon energy with wavevector $\vec{q}$, $\hbar\omega$ is the photon energy, and the two delta functions enforce energy and momentum conservation. Within the parabolic band approximation, a standard calculation yields:

$$JDOS(E) = \frac{1}{8\pi^3} \frac{(2m_r)^{3/2}}{2\pi^2\hbar^3} (\hbar\omega - E_g \pm E_{ph})^{\frac{1}{2}},$$

where m_r is the reduced effective mass, E_g is the indirect bandgap energy, and the $\pm$ sign accounts for phonon emission (-) or absorption (+) processes. The above result shows square-root energy dependence, which is also the case for direct gap semiconductors. However, involvement of phonons relaxes the energy conservation requirements for electron and hole and therefore leads to significantly broader spectral features.

3.1.5 Thermal Distribution of Carriers

Electrons and holes are fermions subject to Fermi-Dirac statistics:

$$f(E) = \frac{1}{e^{\frac{E-E_F}{k_BT}} + 1},$$

where E_F is Fermi energy. However, their densities in semiconductors are sufficiently low that their populations are well approximated by Boltzmann distribution:

$$f(E) = e^{-\frac{E-E_F}{k_BT}}$$

Phonons, being bosons, are not restricted by the exclusion principle. Their occupation factor

F(N_q) follows Bose-Einstein statistics:

$$F(N_q) = \begin{cases} N_q + 1 = \frac{1}{1-e^{-E_{ph}/k_B T}} & \text{for phonon emission} \\ N_q = \frac{1}{e^{E_{ph}/k_B T}-1} & \text{for phonon absorption} \end{cases} \tag{3.4}$$

At low temperature, phonon densities in semiconductors tend to be low and F(N_q) is also well approximated by Boltzmann distribution. This was explicitly confirmed in this work - spectra were fitted using 1.3 as well as Boltzmann distribution, both methods yielding identical results to within 0.01% for all parameters.

3.1.6 Final expressions for PL spectral lineshapes

Complete expressions for PL intensity therefore become:

$$I^{PL}_{allowed}(E) \propto |D_i|^2 \cdot (E - E_g \pm \hbar\omega_q)^{1/2} \cdot F(N_q) \cdot \exp(-(E - E_F)/k_B T)$$

for the allowed processes, assisted by LA and TO phonons and:

$$I^{PL}_{forbidden}(E) \propto |D^{(2)}_i|^2 \cdot (E - E_g \pm \hbar\omega_q)^{3/2} \cdot F(N_q) \cdot \exp(-(E - E_F)/k_B T)$$

for the forbidden LO and TA transitions. Only terms with explicit energy dependence are showcased since the aim of this section is to derive the functional form of spectral lineshapes.

Approximating $F(N_q)$ with Boltzmann distribution, choosing a convenient energy basis and ignoring the remaining constant, one arrives at simplified functional expressions for fitting PL spectra, often seen in literature:

$$I^{PL}_{allowed} \sim E^{1/2} \exp(-E/kT)$$

for the allowed LA and TO transitions and

$$I^{PL}_{forbidden} \sim E^{3/2} \exp(-E/kT)$$

for the forbidden LO and TA transitions.

3.2 Collisional broadening

Free excitons, electrons and holes undergo collisions with each other as well as with atomic sites. Depending on the species involved, these interactions can be mediated by Coulomb forces (electrons and holes) or van der Waals forces (excitons, due to constituent charges screening each other). Exciton-electron collisions have a mixed nature - they are well screened at long interaction distances but approach Coulombic behavior when close.

Impact of a collision on a particle depends on the collision's strength. Weak interactions can be seen as perturbations which cause a momentaneous shift in particle's energy and a disruption of its phase evolution. As interaction becomes stronger, collisions can cause a complete loss of coherence or even induce recombination, destroying the particle entirely.

This section will begin by demonstrating that finite lifetime of a particle causes Lorentzian broadening of its emission profile. Subsequently, it will present Weisskopf theory of collisional broadening and show how it can be adapted to charge carriers in semiconductors. For the purposes of this thesis, the crucial aspect of this model is the relationship between the collisional broadening and the particle density.

3.2.1 Lifetime broadening

It is well known that finite lifetime of charge carriers leads to Lorentzian broadening of spectral features which originate from said carriers. This is a consequence of the uncertainty principle – shorter lifetime means there is less uncertainty in temporal coordinates and therefore uncertainty in particle's energy must increase.

In order to derive the spectral intensity profile, consider time evolution of a wavefunction with a natural decay rate of γ_{nat}:

$$\psi(t) = \psi_0 e^{-i\omega t} e^{-\gamma_{\mathrm{nat}} t/2}. \tag{3.5}$$

In order to convert the expression to the energy basis, a Fourier transform is applied:

$$S(\omega) = \int_0^\infty \psi(t) e^{i\omega t} dt$$
$$S(\omega) = \psi_0 \int_0^\infty e^{-t[i(\omega_0 - \omega) + \gamma_{\text{nat}}/2]} dt$$

For $\gamma_{\text{nat}} > 0$ the integral converges to:

$$S(\omega) = \psi_0 \times \frac{1}{i(\omega_0 - \omega) + \gamma_{\text{nat}}/2}.$$

Spectral intensity $I(\omega) \propto |S(\omega)|^2$ then becomes:

$$I(\omega) = \frac{I_0}{(\omega_0 - \omega)^2 + (\gamma_{\text{nat}}/2)^2}, \tag{3.6}$$

which is the standard form of Lorentz function with FWHM of γ_{nat}.

3.2.2 Weisskopf theory of collisional broadening

Collisions between particles are often the limiting factor for their lifetimes and coherence times. They can be described by Weisskopf theory [39, 40] which was originally developed to quantify collisional broadening of spectral lines emitted by atomic gases. Still, it has been applied to other systems, including plasmas and charge carriers in semiconductors [41, 42].

The central idea of the Weisskopf theory is that "strong" collisions (defined as those which induce a phase shift $\delta\phi$ of more than $\sim \pi$) are all equivalent to each other due to the periodicity of $\delta\phi$: whether $\delta\phi$ falls in the range of, say, $8\pi - 10\pi$ or $18\pi - 20\pi$, the effect on the system is identical and $\delta\phi$ take the form of a uniform distribution. In other words, each event completely destroys coherence and reinitializes the system with a random phase. The problem is thus reduced to simply counting the frequency γ_{coll} of "strong" collisions.

Such interactions are governed by Poissonian statistics. Probability that no collision occurs in time interval dt is

$$P_{\text{survival},dt} = 1 - \gamma_{\text{coll}} \times dt,$$

and probability of no collision during total time $t = dt \times n$ is:

$$P_{\text{survival}}(t) = [1 - \gamma_{\text{coll}} \times (t/n)]^n.$$

In the limit of $n \to \infty$, the above expression converges to

$$P(t) = e^{-\gamma_{\text{coll}} \times t},$$

which is functionally identical to the exponential decay of $|\psi(t)|^2$ from Eq. 3.5. Derivation of Eq. 3.6 can be therefore replicated with $\gamma_{\text{tot}} = \gamma_{\text{nat}} + \gamma_{\text{coll}}$ instead of just γ_{nat} to give

$$I(\omega) = \frac{I_0}{(\omega_0 - \omega)^2 + (\gamma_{\text{tot}}/2)^2},$$

which means that the Lorentzian width of the emission profile is a linear measure of the collision rate.

3.2.3 Collision rate

Standard approach to calculating γ_{coll} is to define Weisskopf radius ρ_c as the critical interaction distance at which the phase shift induced by the collision is equal to π. All collisions at distances of less than ρ_c are defined as "strong" and counted, else they are defined as weak and ignored. Interaction cross-section becomes $\sigma = \pi\rho_c^2$ and the volume swept by a particle in time dt is

$$dV = \pi\rho_c^2 \bar{v} dt.$$

Weisskopf theory assumes that all collisions involve only 2 particles. If we further assumed (incorrectly) that other particles were stationary, the number of collisions would simply become

$$dN = \pi\rho_c^2 \bar{v} n dt,$$

where n is the concentration of colliding particles, and integrating over time would yield

$$\gamma'_{\text{coll}} = \pi\rho_c^2 \bar{v} n.$$

The above expression correctly captures linear dependence of γ_{coll} on $\bar{v}$ and n. However, it ignores the velocity distributions within particle populations as well as the fact that relative

trajectories must be considered in three dimensions. Proper treatment of relative motion between particles must involve integrating over Maxwell-Boltzmann distributions of velocities and over all spatial coordinates. Full derivation yields an additional geometric factor of 4:

$$\gamma_{\text{coll}} = 4\pi\rho_c^2\bar{v}n$$

and, assuming $\gamma_{nat} \ll \gamma_{coll}$, Lorentzian width becomes:

$$\Gamma_L = 4\pi\rho_c^2\bar{v}n \tag{3.7}$$

Weisskopf theory makes a number of strong assumptions which must be born in mind. Only "strong" collisions are counted, multiparticle collisions are neglected, trajectories are treated classically and interaction times must be brief relative to decay times. While the model has been successfully applied to different physical systems and collision mechanisms, caution is prudent when interaction forces are strong and particle densities large.

3.2.4 Energy shifts

Collisions cause not only broadening of spectral features, but also their shifts in energy. This is because interactions between particles perturb their energy levels, displacing them for the duration of the collision. One important difference, compared to broadening, is that shifts are strongly affected by longer-distance interactions which disturb the particle without destroying coherence.

There are two feasible approaches to calculating collision-induced shifts. In the first method, they are treated as Stark shifts and the second-order perturbation theory is applied [41]:

$$\Delta\omega = \frac{n}{2\hbar^2}\int\int \text{Re}\left[\langle 1|\int V(R(t))dt|2\rangle\right]^2 2\pi b\,db\,v\,f(v)\,dv, \tag{3.8}$$

where $V(R(t))$ is the interaction potential, $|1\rangle$ and $|2\rangle$ are energy states in a two-level system, b is the impact parameter and $f(v)$ is Maxwell-Boltzmann velocity distribution. It is noteworthy that $\Delta\omega$ is linear in n which means that ratio $\Delta\omega/\Gamma_L$ is independent of particle density.

Another approach is to follow semi-classical formalism which was used to calculate broadening

in the preceding section but using γ_{tot} which has both real and imaginary parts [40, 43]. It turns out that this approach yields $\Delta\omega/\Gamma_L$ which is independent of either n or T. This ratio is determined solely by the spatial distribution of the interaction potential. This makes it a useful indicator of the nature of interparticle forces (to the extent that assumptions of the semi-classical model hold), which will be explored in Section 4.5.

Van der Waals potential Collisions in atomic gases for which Weisskopf formalism was developed are dominated by van der Waals forces for which $V(r) = Cr^{-6}$. Hence, this type of potential is particularly well discussed in literature. Due to being relatively weak and short range, it is likely to satisfy the conditions of semi-classical formalism. It is also interesting for the scope of this work as exciton-exciton interaction will be mediated by this potential.

Table 3.2 shows the values of the ratio $\Delta\omega/\Gamma_L$ for different exponents m where:

$$V(r) = C_m r^{-m}. \tag{3.9}$$

Naturally, the one of particular interest is m = 6, the other two values not having a clear physical interpretation. Still, they offer an idea of how steeply the ratio changes with m and how representative it is of van der Waals forces in particular.

Table 3.2 Ratio $\Delta\omega/\Gamma_L$ for different interaction potentials [40]

m	5	6	7
ratio	0.250	0.182	0.144

Coulomb potential Interactions between charge carriers are dominated by Coulomb forces, the potential of which decays proportionally to $1/r$. They are more potent than van der Waals forces and remain significant at much longer interaction distances. In fact, to first order, interaction matrices in Eq. 3.8 are independent of the impact parameter. This means that the resulting shifts would be divergent as all interactions would contribute equally, no matter the interaction distance. This would be unphysical and other limiting mechanisms (such as plasma screening) are required to ensure convergence. The calculation is therefore more complex than for m = 6.

Depending on the specific traits of a physical system, ratio $\Delta\omega/\Gamma_L$ can be significantly higher

than that calculated for van der Waals interactions. There is also no reason to expect it to be n-independent, given the importance of screening effects.

Mixed potential Finally, for exciton-electron or exciton-hole collisions, interaction potential is mixed. At short distances it has a more Coulombic character, at large distances it is more reminiscent of van der Waals. Any further conclusions in regard to collisional broadening and shifts would require a detailed study of a particular physical system of interest.

3.3 Power exponents

Laser illumination can induce a variety of phenomena in semiconductor materials. Many such processes exhibit a well-defined power dependence

$$\text{rate} \propto P^k,$$

where P is the laser power and k is the power exponent. This can be a powerful tool to identify the nature of radiative and non-radiative processes occurring in the material. In semiconductors, k-exponents often have integer values since most phenomena involve a discrete number of charge carriers. Examples include:

- Stimulated emission with $k = 1$,
- Two-photon absorption with $k = 2$,
- Auger recombination with $k = 3$.

In practice, various phenomena compete with one another as they rely on the same charge carrier population. $k = 1$ processes such as one-photon absorption and spontaneous emission are likely to dominate at lower excitation powers while multiphoton absorption and Auger recombination can dominate in the high power regime. If power dependence is measured over several orders of magnitude, the full curve is likely to be strongly non-linear with several different exponents present in different parts thereof.

3.3.1 PL intensity power dependence

Of particular interest is power dependence of PL intensity itself. It is best understood within the framework developed by Schmidt et al. [25] and Spindler et al. [26] which is the foundation

of this section's analysis. In a perfect semiconductor under laser illumination we expect that the change in free carrier population is the difference between photogenerated carriers and those which have recombined:

$$\frac{dn_e}{dt} = c_P P - c_x n_e n_h \tag{3.10}$$

where n_e (n_h) is electron (hole) density and c_i are transition coefficients. Several assumptions are made implicitly:

- One-photon processes only
- No multiexcitonic photoemission
- Low and constant temperature
- Negligible transport effects
- P-independent transition coefficients

Note that the $c_x n_e n_h$ term makes no distinction between photoluminescence and non-radiative recombination – it encompasses all mechanisms which require one electron and one hole.

Assuming CW excitation, Eq. 3.10 can be simplified to reflect steady-state conditions ($dn_e/dt = 0$). If we further assume an undoped semiconductor and charge neutrality, we can set $n_e = n_h = n$:

$$c_P P = c_x n^2$$

which means that carrier densities are proportional to $\sqrt{P}$ ($k = 1/2$), even though photocreation rate is linear in P. This sublinear increase in absolute density reflects decreasing lifetime of electrons and holes as they become more abundant and more likely to recombine. Photoluminescence intensity I_{PL} is proportional to $n_e n_h = n^2$ so:

$$I_{\mathrm{PL}} \propto P.$$

The above reasoning can be applied to any mechanism which requires one electron and one hole. This means that the exciton density n_x is proportional to P, as one of each carrier type is needed to form an exciton. This is in contrast to the $\sqrt{P}$-dependence of $n_{e/h}$ and this

difference will be used in Section 4.5 to identify which species is responsible for collisional broadening in Ge.

3.3.2 Role of defects

The presence of defects in a material can provide an additional recombination path for charge carriers. Consider a shallow acceptor state which can capture a free electron. Once charged, it quickly attracts a hole and thus facilitates recombination. Only the first step (electron capture) is rate-limiting and it is independent of n_h. A new term can be added to Eq. 3.10 to account for this process:

$$\frac{dn_e}{dt} = c_P P - c_x n_e n_h - c_{nA} n_e N_A^0 \tag{3.11}$$

where N_A^0 is the density of neutral acceptor defects. Two regimes arise in this scenario:

1. **Low excitation power:** $N_A^0 \gg n_h$

   We can ignore the $c_x n_e n_h$ term and (in steady-state) Eq. 3.11 becomes:

   $$c_P P = c_{nA} n_e N_A^0$$

   Assuming $N_A^0 \approx N_A$ (N_A being the total density of acceptor defects), we obtain $n_e \propto P$ or, equivalently: $k_e = 1$. As to hole density, it is not affected by acceptor states so $n_h \propto \sqrt{P}$ (or $k_h = 1/2$) as before. k-exponents combine additively:

   $$I_{\mathrm{PL}} \propto n_e n_h = P^{k_e} P^{k_h} = P^{k_e + k_h},$$

   and therefore power dependence of PL intensity becomes

   $$I_{\mathrm{PL}} \propto P^{3/2}.$$

2. **High excitation power:** $N_A^0 \approx 0$

   When virtually all acceptor states are occupied, the last term in Eq. 3.11 can be ignored and defects no longer have an effect on the recombination dynamics.

   $$I_{\mathrm{PL}} \propto P$$

This two-regime power dependence is commonly observed in semiconductor PL. Initially PL intensity is suppressed by nonradiative defect recombination but increases superlinearly with $k = 3/2$. Once defects are saturated, linear dependence on P resumes. By extension, if both acceptor and donor states are present then $k_e = 1$ and $k_h = 1$ leading to $k_{\mathrm{PL}} = 2$. As excitation power increases, one of defect types becomes saturated reducing k_{PL} to 3/2 and then to 1 when all defects become occupied.

During the transition from one regime to another, the behavior is nonlinear. This underscores the need to measure power dependence over several orders of magnitude, and with a sufficient resolution in P, as otherwise the results may be strongly misleading.

3.3.3 Common misconceptions

Finally, it is important to explicitly address a common source of confusion in scientific discussions, including the existing literature on Ge PL. It is intuitively appealing to assume that the charge carrier density n in a semiconductor is directly proportional to laser power, based on the fact that the carrier generation rate is, indeed, proportional to P. However, in light of the theory outlined in this chapter, this does not reflect the actual power dependence of n—it was demonstrated in Section 3.3.1 that $n \propto \sqrt{P}$ in the absence of defects.

Consider the carrier population dynamics after photoexcitation. If P is doubled, then the number of initially created charge carriers doubles as well. But now, electrons and holes have a higher probability of encountering each other and their radiative lifetime decreases. Therefore, the absolute carrier concentrations increase by a factor of less than 2—specifically, they exhibit power exponents $k_e = k_h = 1/2$. This is necessary to ensure the power exponent of $k_{\mathrm{PL}} = 1$ for PL intensity, since $k_e = k_h = 1$ would lead to $k_{\mathrm{PL}} = 2$.

Non-radiative recombination adds another dimension to the problem, particularly in an indirect semiconductor such as Ge. Most photoexcited charges recombine in this fashion and their energy is converted to heat. However, this does not necessarily affect k_{PL}, as long as the fraction of non-radiatively recombined carriers remains constant under increasing laser power. This depends on the precise balance between radiative and non-radiative recombination lifetimes. It will be shown in the course of this thesis that the measured Ge PL can exhibit $k_{\mathrm{PL}} = 1$, despite the ubiquitous non-radiative recombination.

CHAPTER 4 INDIRECT PL LINESHAPES

Spectral lineshape of photoluminescence contains a wealth of information about material properties and phenomena induced by laser illumination. Peak positions reveal band structure and defect energies, functional shape is determined by the nature of an optical transition while additional broadening offers insight into photoinduced charge carrier population and their dynamics.

Germanium is among the most scientifically and industrially important semiconductors and yet, literature discussing its PL lineshapes is limited and sometimes inconclusive. Most publications date back to 1970s when existing technology required very long acquisitions times. This meant researchers could only measure a small number of high quality spectra, making it difficult to conduct rigorous analysis resolved in laser power, temperature and other parameters. This often prevented comprehensive analysis that could validate their findings across a range of experimental conditions.

This work made use of a modern high performance detection system to perform such multivariate analysis. The acquired spectra allowed to critically assess prior studies, shed light on contentious issues and develop and validate a more complete model of Ge PL lineshapes. In particular, detailed analysis of Lorentzian broadening proved that collisions with free charges, rather than other excitons, are the dominant coherence-limiting mechanism for excitons in Ge (contrary to earlier claims in literature [42]).

Comprehensive modeling of phonon-assisted photoluminescence spectra of Germanium requires consideration of the following contributions:

- joint density of states and occupation probability (derivation in Section 3.1.4),
- fine structure of the excitonic ground state energy,
- correction for band non-parabolicity,
- collisional (Lorentzian) broadening with excitons and carriers
- broadening due to isotopic disorder (Gaussian) and

- instrumental broadening (Gaussian).

This chapter will present a review of existing literature on the subject, before proceeding to examine each contribution in turn, offering new insights into the physical processes behind them.

All experimental data showcased in this chapter was measured on natural Ge, unless otherwise noted.

4.1 Literature review

One of the first experimental studies that attempted to model indirect phonon-assisted germanium PL was presented by C. Benoit à la Guillaume and M. Voos in 1973 [44]. Their motivation was to obtain a more accurate value of EHD binding energy relative to FE energy. Like all other publications cited in this thesis, they began their modeling with the theoretical lineshape, first calculated by R. J. Elliott in 1957 [37] (see 3.1.2 for detailed derivation). They then accounted for the splitting in indirect exciton ground state, using a value of $\Delta E = 0.8$ meV [45]. To that effect, they added a secondary peak shifted by ΔE and with an amplitude of exp(-$\Delta E/kT$) relative to the primary peak. They interpreted additional broadening as Gaussian in shape, citing the finite lifetime of phonons as a probable cause.

A similar study was performed by T. K. Lo [46], in which ΔE of 0.7 ± 0.1 meV was reported and no extraneous Gaussian or Lorentzian broadening was observed (after correcting for set-up resolution). Thomas et al. [42] offered yet another view on peak width, whereby they ascribed broadening observed in their work to collisions between excitons. They applied Weisskopf theory of collisional broadening and modeled it with a Lorentzian function. They also replaced theoretical density of states (based on parabolic bands) with experimental absorption data. This was done to implicitly account for non-parabolicity of bands and the FE ground state splitting.

Kamerman et al. [38] agreed with and implemented the same approach as Thomas et al. [42]. In addition, they reported Gaussian broadening of 0.25 meV. It was found to be independent of temperature and incident laser power; its origin was not conclusively determined. Later studies tended to simply cite results from the aforementioned publications [47] and, even though several decades have passed, many questions have remained unresolved. These include

the extent and the origin of the Gaussian broadening as well as the mechanism responsible for the collisional broadening.

Among more recent works, a publication by Menendez et al. [36] stands out due to a different approach and a robust theoretical model. They made a detailed calculation of optical absorption in Ge and used the van Roosbroeck–Shockley equation:

$$\frac{1}{V}\frac{dR}{d\Omega d\omega} = \frac{1}{4\pi^3}\left(\frac{n_{op}\omega}{c}\right)^2 \frac{\alpha(\omega)}{\exp\left(\frac{\hbar\omega-\Delta F}{k_B T}\right)-1}, \tag{4.1}$$

to calculate spontaneous emission as a function of photon energy. However, their objective was to obtain a model which works reasonably well across the entire 4–300 K temperature range. For cryogenic conditions, it is preferable to use the older, more explicit model, the assumptions of which are satisfied by low temperature systems.

4.2 Theoretical lineshape

Section 3.1.2 presented the derivation of the spectral shape for indirect photoluminescence in Ge. It resulted in the following expressions for PL intensity I_{PL}:

$$I^{PL}_{allowed} \sim E^{1/2}\exp(-E/kT) \tag{4.2}$$

for allowed LA and TO transitions and

$$I^{PL}_{forbidden} \sim E^{3/2}\exp(-E/kT) \tag{4.3}$$

for forbidden LO and TA transitions.

These expressions and phonon assignments are well established in scientific literature. It must be noted, however, that there is significant visual similarity between forbidden phonon lineshape with limited broadening and strongly broadened allowed phonon lineshape. This means that it can be challenging to experimentally validate how accurate these assignments are. The weak LA-assisted PL peak measured in ^{76}Ge and shown in Fig. 4.1 demonstrates this point well. It should represent an allowed transition, and yet, forbidden lineshape offers a more visually compelling fit.

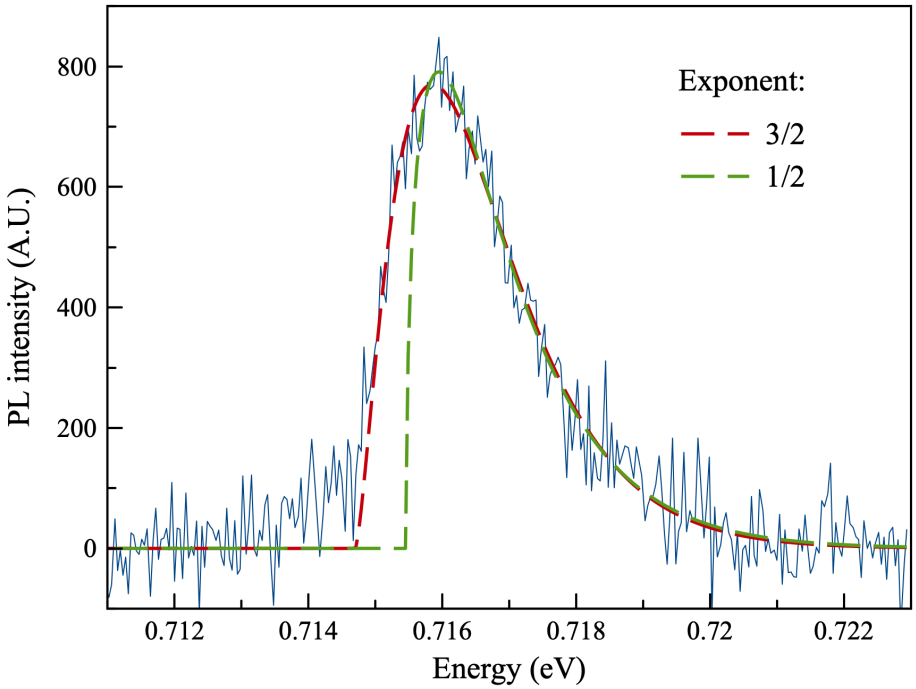

Figure 4.1 Intensity spectrum of LA-assisted indirect PL in ^{76}Ge. It should exhibit allowed lineshape with an exponent of 1/2. Forbidden lineshape with an exponent of 3/2 only appears to offer a more visually compelling fit due to the presence of broadening.

In order to conclusively demonstrate that LA phonons lead to an allowed transition, it is helpful to track the spectral evolution as the temperature T of the sample is changed. Allowed and forbidden PL peaks will evolve differently as the expression for the forbidden lineshape has an additional factor of E. A useful metric is the ratio of the energy position at the intensity maximum E_{max} to $FWHM$ which turns out to be independent of temperature. This makes it a convenient indicator of the nature of the transition. The detailed derivation is presented below, followed by the experimental demonstration.

Derivation

Spectral lineshapes for allowed and forbidden transitions can be expressed in the form

$$I(E) = E^x \exp(-\beta E),$$

where $\beta = 1/kT$ and $x \in \{0.5, 1.5\}$. The energy E_{max}, at which the intensity $I(E)$

reaches its maximum value, can be found by taking the derivative and setting it to zero:

$$\frac{dI}{dE} = xE^{x-1}\exp(-\beta E) - \beta E^x \exp(-\beta E) = 0.$$

This yields

$$E_{\max} = \frac{x}{\beta}. \tag{4.4}$$

Obtaining the expression for FWHM requires a more complex mathematical treatment. Half-maximum energies E_1 and E_2 are defined through:

$$E_{1,2}^x \exp(-\beta E_{1,2}) = \frac{1}{2} E_{\max}^x \exp(-\beta E_{\max})$$

Substituting $E_{\max}$ from Eq. 4.4:

$$E_{1,2}^x \exp(-\beta E_{1,2}) = \frac{1}{2}\left(\frac{x}{\beta}\right)^x \exp(-x), \tag{4.5}$$

The solution can be obtained using the Lambert W function, since Eq. 4.5 can be rearranged in the form $ue^u = z$. The transformation begins with multiplying both sides by $(-\beta/x)^x$, leading to

$$\left(-\frac{\beta}{x}\right)^x E_{1,2}^x \, e^{(-\beta E_{1,2})} = \frac{(-1)^x}{2} e^{-x}.$$

For the left-hand side, the substitution of $u = -\frac{\beta}{x} E_{1,2}$ can be applied, yielding

$$(-1)^x u^x e^{xu} = \frac{(-1)^x}{2} e^{-x}$$

Dividing by $(-1)^x$ and taking the x-th root, one arrives at

$$ue^u = \left|\frac{1}{2^{1/x}} e^{-1}\right|,$$

where the absolute value appears due to the information on the sign being lost when the x-th root is taken. Depending on the value of

$$z = \left|\frac{1}{2^{1/x}} e^{-1}\right|,$$

the Lambert W function can have 0, 1 or 2 solutions. Given the nature of the problem, the 2-solution regime is pertinent, requiring $-e^{-1} \leq z < 0$. This is satisfied for

$$ue^{u} = -\frac{1}{2^{1/x}}e^{-1},$$

as long as $x > 0$, which is always expected. The two solutions of the Lambert W function are then

$$u_1 = W_0\left(-\frac{e^{-1}}{2^{1/x}}\right),$$
$$u_2 = W_{-1}\left(-\frac{e^{-1}}{2^{1/x}}\right).$$

Converting back to energies using $u = -\frac{\beta}{x}E_{1/2}$ gives

$$E_1 = \frac{x}{\beta}W_0\left(-\frac{e^{-1}}{2^{1/x}}\right),$$
$$E_2 = \frac{x}{\beta}W_{-1}\left(-\frac{e^{-1}}{2^{1/x}}\right),$$

leading to

$$FWHM = |E_2 - E_1| = \frac{x}{\beta}|W_{-1}(z) - W_0(z)|, \tag{4.6}$$

where $z = -\frac{e^{-1}}{2^{1/x}}$.

The ratio $r = E_{max}/FWHM$ can then be calculated using Eq. 4.4 and 4.6:

$$r = \frac{E_{\max}}{FWHM} = \frac{x/\beta}{(x/\beta)|W_{-1}(z) - W_0(z)|} = \frac{1}{|W_{-1}(z) - W_0(z)|}. \tag{4.7}$$

Note that the temperature dependence cancels completely, leaving the ratio that depends only on the exponent x. Computing W_k terms leads to the r values of 0.556 for $x = 0.5$ and 0.330 for $x = 1.5$.

In Fig. 4.2, the values of E_{max} are plotted on the y-axis and the values of $FWHM$ on the x-axis. E_{max} values were corrected for the Varshni shifts calculated from the fitted electronic temperatures. The slope correspond to the ratio r derived above and has a value of 0.52±0.03. Note that this is a lower bound, as non-thermal broadening was not subtracted from the measured widths. The slope is in good agreement with a theoretical value of 0.556 for allowed transitions. The analysis presented in this section constitutes a rigorous demonstration that LA-assisted recombination in Ge is, in fact, allowed, with an exponent $x = 0.5$.

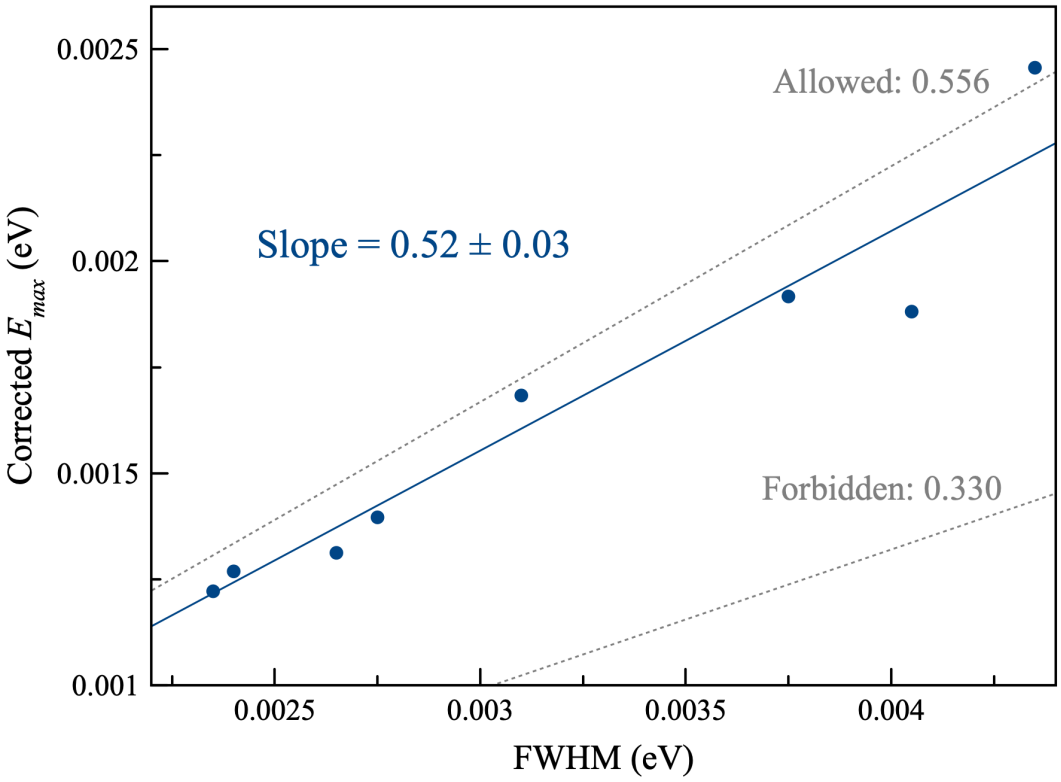

Figure 4.2 Evolution of the maximum position w.r.t. broadening for LA-assisted Ge PL. Slope of 0.52 is consistent with the allowed lineshape. (Note: Varshni shifts were corrected for.)

4.3 Energy splitting

The group theory derivation in Section 3.1.1 briefly mentioned that a spin-orbit interaction in the D_{3d} representation lifts the 4-fold degeneracy of the valence bands in Ge and splits them into two doublets [34]. This leads to an energy splitting ΔE in the ground state of the indirect exciton. It has been described theoretically [48, 49], observed experimentally in

absorption measurements [45, 50] and applied to modeling PL spectra [44, 46].

Fig. 4.3 shows a wavelength modulation absorption spectrum of Ge [50]. $\Delta\alpha$ is calculated by dividing wavelength modulation intensity by total intensity - it is therefore proportional to $d\alpha/d\lambda$, making it sensitive to sharp energy transitions. The spectrum exhibits two prominent features which correspond to x_1 and x_2 - two energy levels of the split indirect exciton ground state.

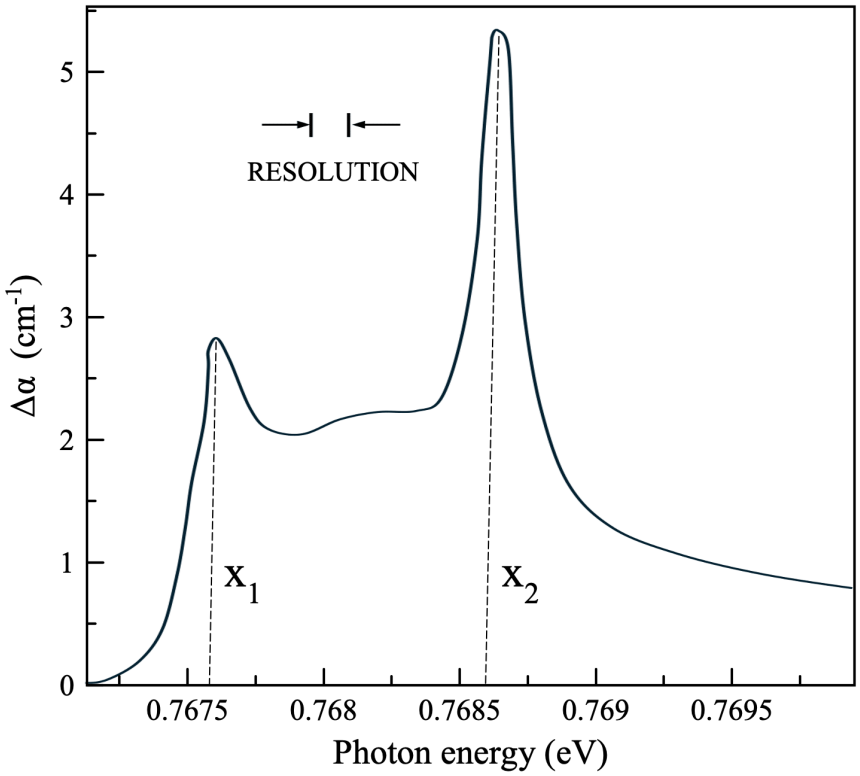

Figure 4.3 Wavelength modulation absorption spectrum of Ge (data from [50]). Two peaks correspond to x_1 and x_2 - energy levels of the split indirect exciton.

The splitting is large enough to significantly affect PL spectra of Ge, particularly at low temperature and low excitation power. In the PL studies discussed earlier in this chapter, the splitting was either ignored or incorporated into the model using earlier literature values for ΔE. In this work, ΔE will actually be extracted from the fits - both explicitly and from the thermal evolution of the ratio of peak intensities.

Sample temperature must be chosen carefully so that the splitting is featured prominently in emission spectra. At very low temperatures (below 4 K) free excitons do not have sufficient thermal energy to significantly populate the higher energy state. Therefore, single peak is expected to offer a satisfying fit for a PL spectrum and the splitting can be neglected. At higher temperatures (above 10 K) thermal broadening becomes overwhelming relative to ΔE. Moreover, assumptions of the theory outlined in section 3.1.2, such as band parabolicity, become increasingly inaccurate. Hence, the splitting becomes negligible compared to other uncertainties in any conceivable model and cannot be extracted from PL data.

At intermediate temperatures (4–10 K), the splitting significantly affects the lineshape of the emission. Fig. 4.4a shows two spectra measured at 5.8 K and 8.0 K (energy splitting and relative amplitudes of the peaks were unconstrained in the fitting procedure). ΔE was obtained from a larger number (18) of spectra, similar to those shown in Fig. 4.4a and measured at different temperatures, yielding an average value of:

$$\Delta E = (0.77 \pm 0.05)\,\text{meV}.$$

The uncertainty of 0.05 meV accurately reflects the spread in the 18 measured values. Fig. 4.4a clearly shows the amplitude ratio r changing with temperature. Population transfer from x1 to x2 is expected to be thermally activated and thus r was modelled as:

$$r = r_0 \ \exp\left(-\frac{\Delta E}{kT}\right)$$

.

Fitting r values measured at different temperatures (Fig. 4.4b) with the above equation gives $\Delta E = (0.7 \pm 0.2)\,\text{meV}$, consistent with the value extracted directly from the fits, although with a higher uncertainty. To our knowledge, this is the first reported determination of ΔE from PL temperature dependence.

Literature values for ΔE are outlined in Table 4.1. They are all within the same order of magnitude but the disparities are still significant. Energy splitting presented in this thesis is in a reasonable agreement with them, considering their spread. In particular, it is very similar to the value reported in [45] and has a slightly lower measurement uncertainty. However, it is $\sim 25\%$ smaller than a low-uncertainty value from [50].

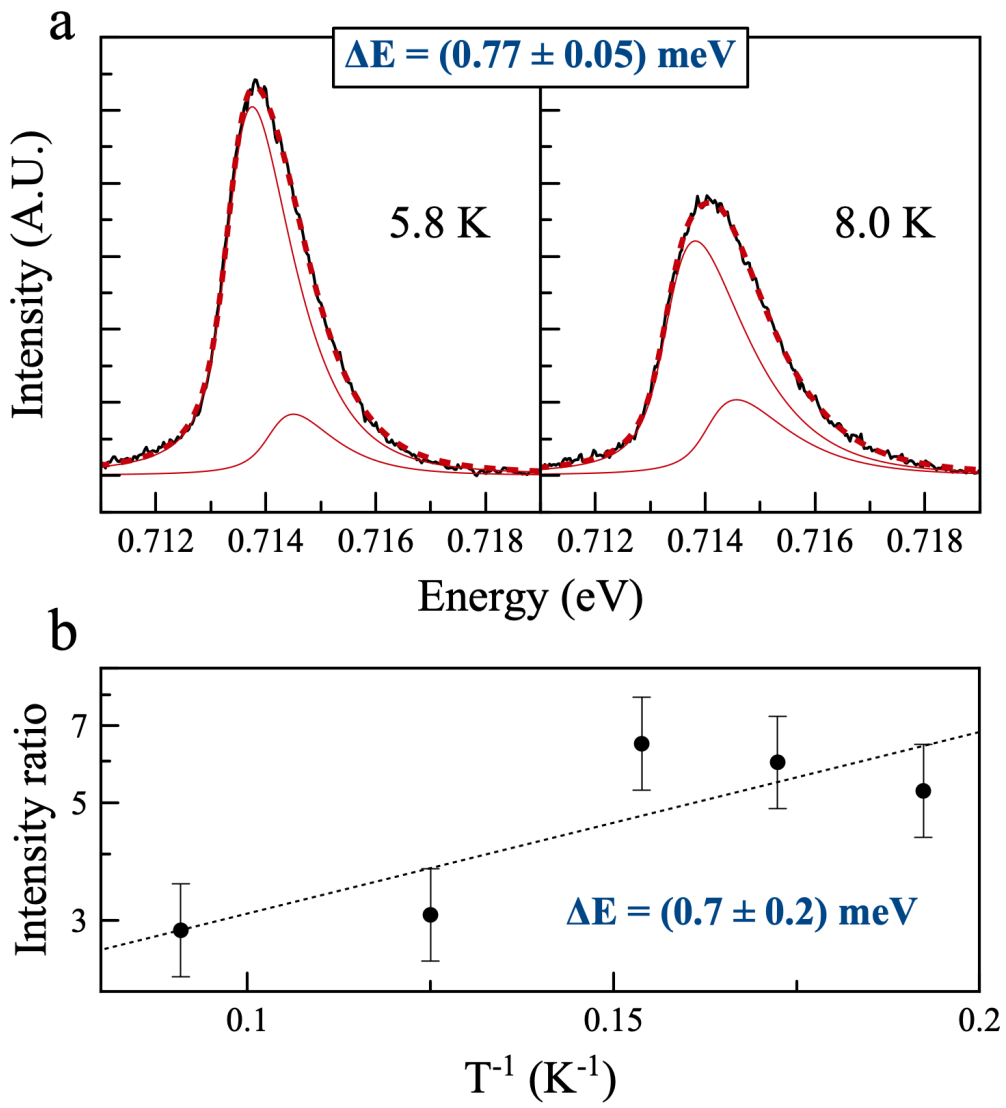

Figure 4.4 Ge emission spectra measured at different temperatures showing the energy splitting in the excitonic ground state. Both estimates for ΔE (extracted (a) directly from spectral fits and (b) from temperature dependence) are in agreement with one another and with [45]

.

Table 4.1 Literature values for energy splitting ΔE in germanium

Reference	Method	ΔE (meV)
[48]	Theory	0.355
[49]	Theory	1.01
[45]	Absorption	0.8 ± 0.1
[50]	Absorption	1.01 ± 0.03
This work	**PL spectra**	$\mathbf{0.77 \pm 0.05}$
	T dependence	$\mathbf{0.7 \pm 0.2}$

In order to assert the validity of the above model, it is worth considering its effect on other fit parameters, compared to a singlet-based fit. When the splitting is included, Lorentzian broadening linewidth is not significantly affected, temperature values decrease and become more consistent with thermometer readings while Gaussian broadening is also lowered and becomes more consistent with the experimentally determined resolution of the set-up. This provides further evidence for the importance of the splitting in modelling Ge PL spectra at low temperatures, as not doing so leads to overestimating electronic temperature and Gaussian broadening.

4.4 Non-parabolicity of bands

The derivation in section 3.1.2 assumed that energy bands were parabolic, leading to JDOS being proportional to $E^{1/2}$ for allowed phonon-assisted transitions. In this work, all fitting models implement this parabolic approximation. It can be expected to work well near the band minima, but it begins to break down as $|\vec{k} - \vec{k_0}|$ increases. There are a variety of factors which can cause this and it is important to be aware of these in order to properly assess any deviations from the model.

Firstly, exciton splitting described in the preceding section leads to non-parabolicity as the energy levels interact with one another. This manifests itself in an anti-crossing [42, 49] shown in Fig. 4.5. It is possible to correct for this effect (as well as for the splitting itself) by replacing JDOS in lineshape expressions with experimental absorption data. Alternatively, one could explicitly use a phenomenological expression for the non-parabolic dispersion, as the one proposed by Frova et al. [50].

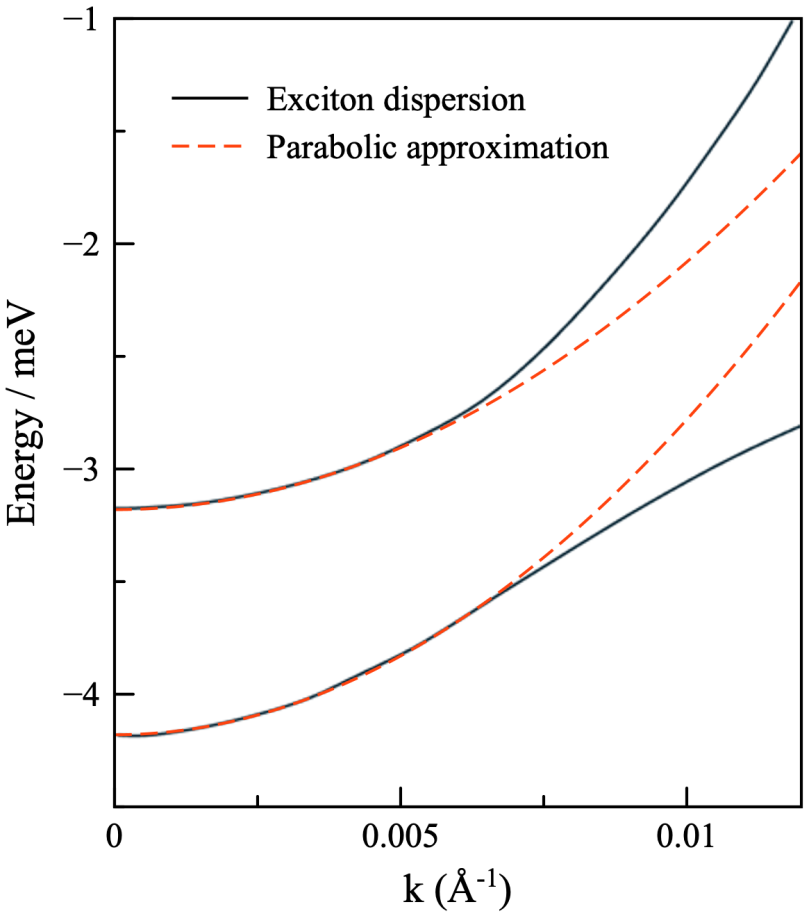

Figure 4.5 Energy dispersion of the split indirect exciton ground state in Ge. Solid black curves show theoretically calculated dispersion (data from [49]) and dashed red lines show parabolic extrapolation. Deviation between the two represents an anti-crossing due to the interaction between the two energy states.

This source of non-parabolicity ought to be important only in the energy range close to the anti-crossing. At lower energies (below ~ 0.3 meV) parabolic approximation is accurate and at higher energies (above ~ 2 meV) mass reversal is complete and bands become quadratic again.

At those higher energies, deviations from first-order $k \cdot p$ theory can be expected. These were discussed in detail in early studies by E. O. Kane [51]. In this work, no corrections are implemented to account for this effect. However, departure from the model was consistently seen in the high-energy tail of indirect PL peaks (see Fig. 4.14). It is most likely caused by phenomena described in Kane's extended $k \cdot p$ calculation.

4.5 Collisional broadening

Charge carriers responsible for photoluminescence undergo collisions with each other which negatively affect their lifetime as well as coherence time. In PL spectra, this is manifested by broadening of the peaks which is described in detail in section 3.2. Within the assumptions of the Weisskopf theory, we expect the collisional broadening to be Lorentzian and have a full width Γ_L of:

$$\Gamma_L = 4\pi\rho_c^2 \overline{v} n, \tag{4.8}$$

where ρ_c is the Weisskopf radius, $\overline{v}$ is the average relative speed of collisions and n is the density of colliding particles. It can be incorporated into the lineshape model using convolution:

$$I_1(h\nu) = \int_{-\infty}^{\infty} I_0(h\nu') \cdot \frac{\Gamma_L/2}{\pi} \cdot \frac{1}{(h\nu' - h\nu)^2 + (\Gamma_L/2)^2}, d(h\nu') \tag{4.9}$$

where I_0 and I_1 are lineshapes without and with the Lorentzian broadening and $h\nu$ is the photon energy.

It is pertinent to demonstrate that the experimental data justifies the use of a Lorentzian to model power broadening, rather than any other functional shape. A significant overlap between TO and LA peaks provides an opportunity to do so. Consider an incorrectly modeled broadening in the LA replica – because of the overlap, it would affect the TO replica fit (particularly its high energy tail) and would lead to inconsistent electronic temperatures

extracted from the two peaks. Comparing T_{LA} (electronic temperature extracted from the LA peak) and T_{TO} can validate the use of Lorentzian broadening in a more compelling manner than a straightforward visual examination.

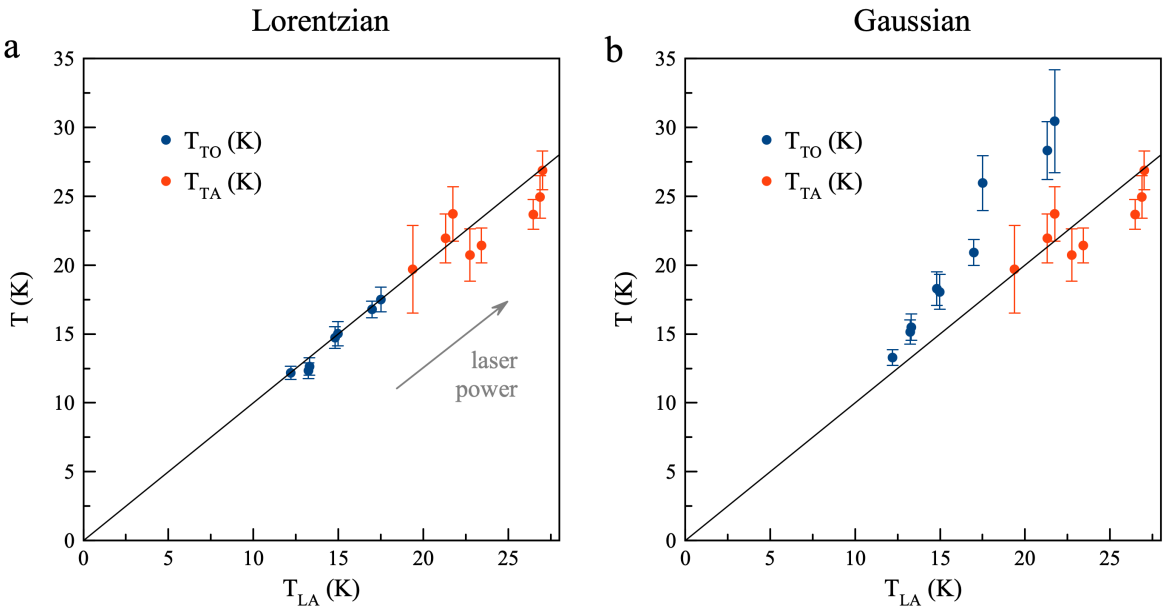

Figure 4.6 Comparison of T_{TO} to T_{LA} when a) Lorentzian or b) Gaussian fit is used to model the collisional broadening. Solid lines have a slope of 1, representing consistent electronic temperatures. Only the Lorentzian model leads to uniform T_{TO} and T_{LA} values (indicated by the solid line with the slope of 1). T_{TA} values (less affected, due to a negligible overlap of TA and LA peaks) are shown in red.

4.5.1 Broadening mechanism

Thomas et al. (1978) ascribe Lorentzian broadening in Ge to collisions between excitons. However, our detailed measurements of Ge PL disprove this claim and demonstrate that the collisions with free electrons and holes have the dominant effect. This can be expected a priori, as electrostatic potential exerted by an exciton is proportional to r^{-6} while Coulombic potential, characteristic of a free charge, falls off with the square of the distance which makes interactions more potent.

A similar result was reported in GaAs single quantum wells [52], where collisional broadening due to exciton-free carrier interactions was found to be 8 times stronger than broadening

due to exciton-exciton collisions. However, it must be noted that there exist two important differences between that physical platform and the bulk Ge. Firstly, GaAs is a direct bandgap semiconductor leading to very different carrier dynamics compared to Ge. Secondly, quantum wells have reduced symmetry relative to bulk crystal which affects the nature of exciton and carrier interactions as well as their spatial distributions.

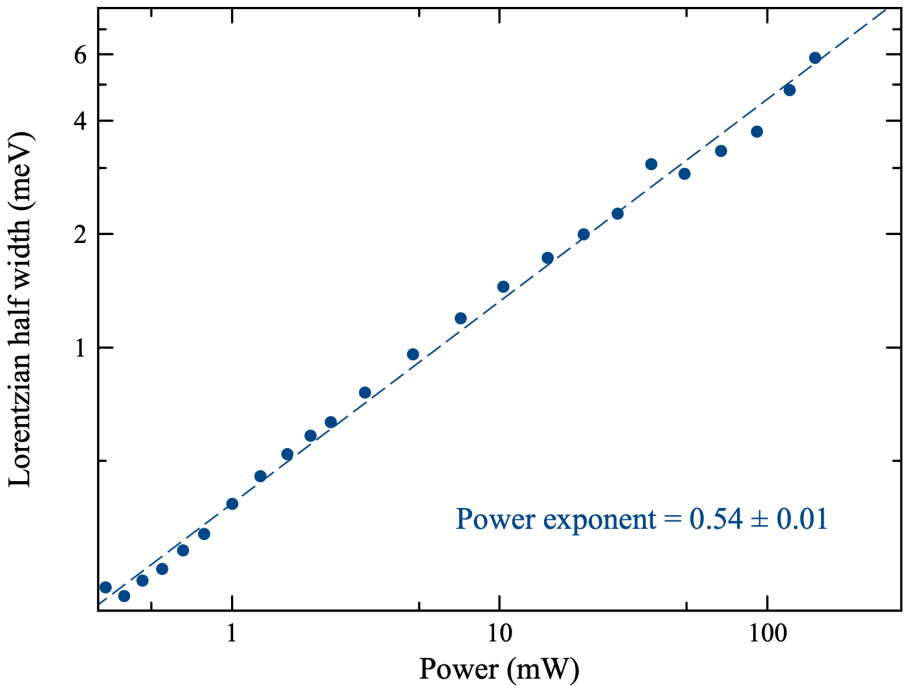

Figure 4.7 Power dependence of Lorentzian broadening. The logarithmic plot shows a straight line with a slope of 0.54 ± 0.01, indicating that collisional broadening is proportional to the square root of incident laser power.

Fig. 4.7 shows the power dependence of the Lorentzian broadening in Ge PL. For the same data set, total PL intensity is directly proportional to P_{laser} (see Section 5.2 for detailed discussion). As explained in Section 3.3 on the theory of PL power exponents, such linearity implies that free electron and hole densities (n_e and n_e) are proportional to $\sqrt{P_{\text{laser}}}$. At the same time, the probability of exciton formation is proportional to $n_e n_h = \sqrt{P_{\text{laser}}}^2 = P_{\text{laser}}$. The trend seen in Fig. 5.3 demonstrates that collisional broadening has power dependence representative of free electrons and holes, rather than excitons and thus:

$$\Gamma_L \propto n_e = n_h.$$

Equivalently, one may link Γ_L directly to PL intensity through:

$$I_{\mathrm{PL}} \propto n_e n_h \propto \Gamma_L^2, \tag{4.10}$$

which is appealing in that it links two intrinsic features of photoluminescence, independently of laser power or any other instrumental parameters.

Under certain excitation regimes, PL intensity may not be linear in $\mathrm{P_{laser}}$ (see section 5.4 for further discussion). Such conditions provide an opportunity to verify the generality of Eq. 4.10. As shown in Fig. 4.8, despite this extreme non-linearity, the relationship between I_{PL} and Γ_L still holds true. Eq. 4.10 is therefore a general relationship independent of excitation regime and it offers strong evidence that Γ_L can be used as a direct measure of free charge density.

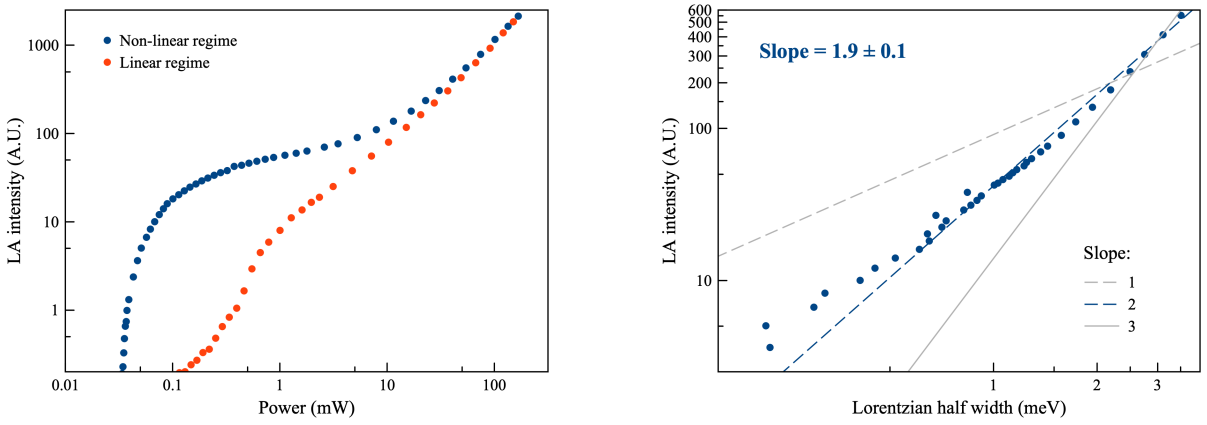

(a) (b)

Figure 4.8 LA-assisted PL intensity (a) as a function of P_{laser} showing strong non-linearity and (b) as a function of Lorentzian width showing approximately quadratic dependence. The relationship $I_{\mathrm{PL}} \propto \Gamma_L^2$ holds true even in excitation regimes where PL intensity is not linear in laser power.

4.5.2 Temperature dependence of collisional broadening

Free exciton binding energy in Ge is 2.7 meV [53], equivalent to thermal energy at 31 K. The ratio R of free electron (hole) density $n_{e/h}$ to a total density of free electrons (holes) and excitons $(n_{e/h} + n_x)$ will exhibit strong temperature dependence near or below this

temperature. This thermally activated dissociation problem can be addressed using the Sacha equation:

$$\frac{n_e n_h}{n_x} = \frac{N_c N_v}{N_x} \exp\left(-\frac{E_x}{k_B T}\right), \tag{4.11}$$

where N_i are the densities of states available for the particles under consideration, and solving for:

$$R = \frac{n_{e/h}}{n_{e/h} + n_x}$$

Assuming $\Gamma_L \propto n_{e/h}$, one can replace excess electron and hole concentrations in Eq. 4.11 with the Lorentzian width. Implicitly, this also assumes that excitons' contribution to collisional broadening is negligible. As explained before, this seems reasonable due to inferior strength of van der Waals forces. There are, however, two additional effects to consider:

- As per Eq. 4.8, Γ_L is proportional to $\overline{v}$ which is in turn proportional to $T^{1/2}$
- Lifetime of charges is T–dependent. Low overall PL yield in Ge indicates that non-radiative recombination is the limiting mechanism. Such processes tend to have T – dependence of between $T^{-1/2}$ to T^{-1} [54].

Approximately, these two effects are expected to cancel each other out. Therefore, to first order, Eq. 4.11 can be applied directly to Γ_L. Fig. 4.9 shows the temperature dependence of Lorentzian broadening, where T values are electronic temperatures extracted from fits. Γ_L increases for temperatures below $\sim 10\,\mathrm{K}$, at which point it begins to saturate. It is well modelled by Eq. 4.11 and yields $E_x = (3.4 \pm 0.3)\,\mathrm{meV}$, consistent with the FE binding energy. The uncertainty in E_x is rather small despite the lack of data points for low and intermediate temperatures. The modeled lack of collisional broadening at very low temperatures corresponds to the fact that, at $T \to 0$, virtually all charge carriers combine to form excitons.

It should be noted that similar plots were made for other T-dependent sets of spectra and the saturation was not always as clear. Usually, Γ_L continued to rise slightly even beyond the initial sharp increase. This demonstrates the limitations of the assumptions made earlier regarding T-dependent carrier velocities and lifetimes. At the same time, the inconsistent behavior shows that devising a more realistic model would be challenging.

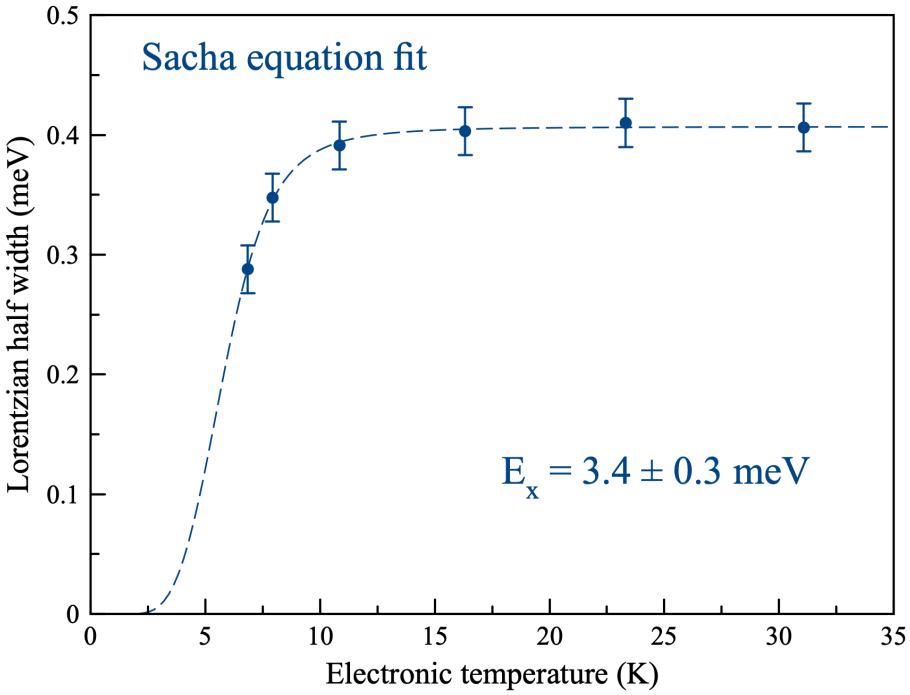

Figure 4.9 Temperature dependence of Lorentzian broadening in natural Ge. The dashed line shows a fit using Eq. 4.11 yielding an exciton binding energy of $E_x = (3.4 \pm 0.3)\,\mathrm{meV}$.

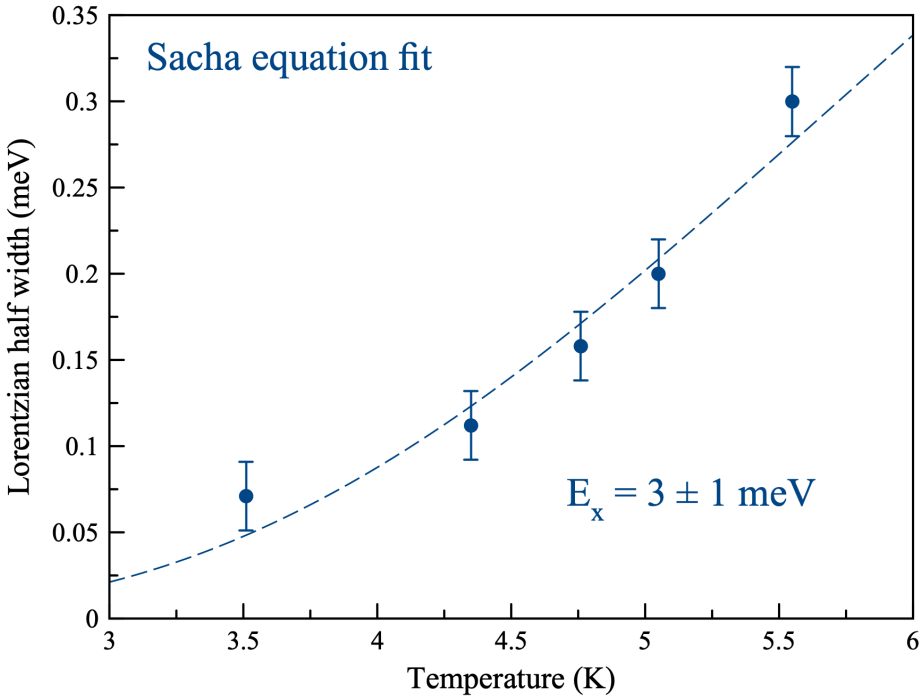

Figure 4.10 Temperature dependence of Lorentzian broadening from Thomas et al. [42] data. The dashed line shows a fit using Eq. 4.11 yielding $E_x = (3 \pm 1)\,\text{meV}$, consistent with the free exciton binding energy in Ge.

Thomas et al. [42] offered a different interpretation for their T-dependent data. Consistent with their model of exciton-exciton collisions, they attributed the increase in Γ_L with temperature to the dissociation of electron-hole droplets (see Section 6.1 for a more detailed discussion of EHD) into free excitons. They used a Boltzmann fit to obtain dissociation energy of 1.8 meV. However, their model is not consistent with power dependence presented earlier in this chapter.

Fig. 4.10 shows the data from Thomas et al. fitted with Eq. 4.11. Compared to Fig. 4.9, their data falls into a slightly lower temperature range. The uncertainty in $E_x = (3 \pm 1)$ meV is substantial but it is consistent with the value obtained from Fig. 4.9, as well as literature. This demonstrates that the data from Thomas et al. can be adequately explained by the collision model proposed in this thesis.

4.5.3 Energy-shift-to-broadening ratio

The semi-classical model of Weisskopf collisions predicts a constant ratio of the energy shift $\Delta\omega$ to the full width Γ_L, only dependent on the nature of the interaction potential governing the collisions. As discussed in Section 3.2.4, for the van der Waals potential, $\Delta\omega/\Gamma_L$ is expected to be 0.182. The ratio is therefore a useful indicator of the nature of the interparticle forces involved in the interactions.

Measured energy shifts are shown in Fig. 4.11, along with the Varshni shifts calculated from the fitted electronic temperatures [55]. To isolate the effect of the collisions, $\Delta\omega$ was calculated by subtracting Varshni shifts from the total measured ones. These corrected values were then used in the ratio evaluation.

Fig. 4.12 shows the values of the ratio $\Delta\omega/\Gamma_L$. The data points exhibit two linear regimes, at low and at high excitation intensities. The increasing ratio indicates the decreasing impact of the short-distance "strong" interactions (which are the primary cause of broadening Γ_L), relative to long-distance interactions (shifts $\Delta\omega$ are less dependent on the impact parameter). The precise meaning of the two linear regimes is unclear. However, the overall trend is very different from the constant ratio of 0.182, expected for van der Waals interactions, providing

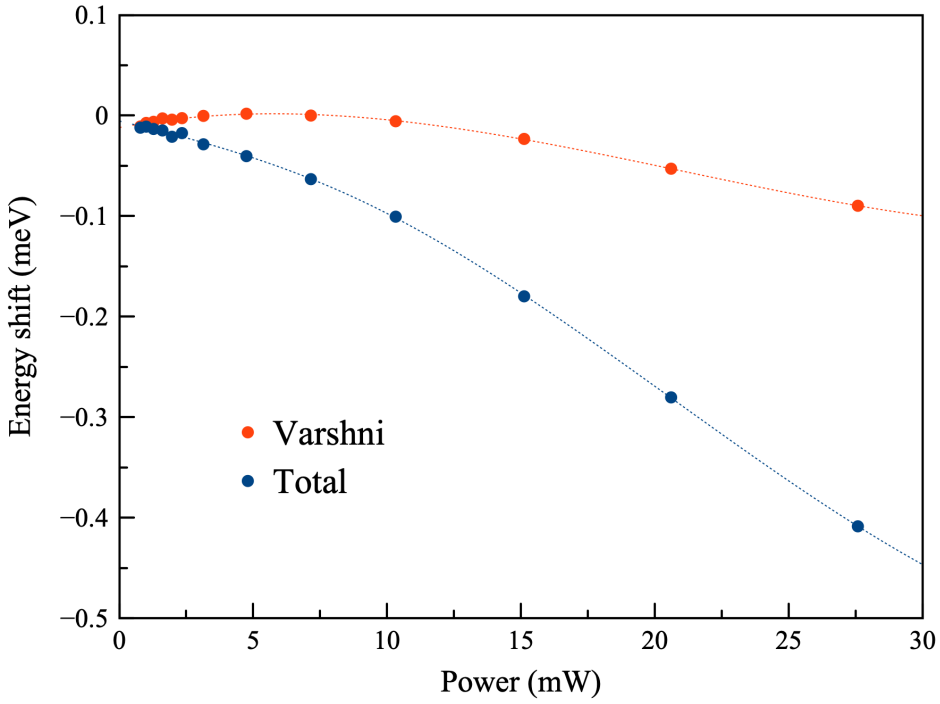

Figure 4.11 Energy shifts in Ge PL peaks as a function of laser power. Blue points show total measured shifts while red points show Varshni shifts calculated from fitted electronic temperature. Dashed lines are intended as a visual guide only.

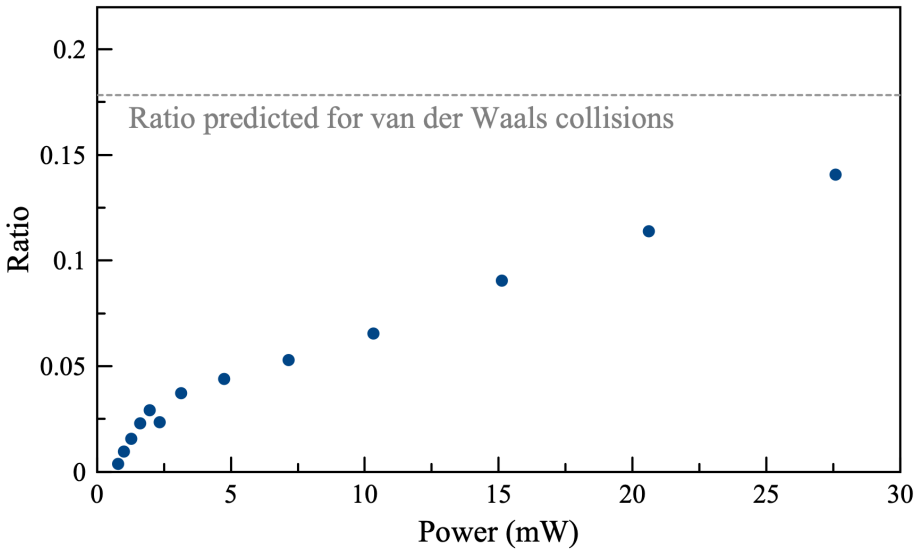

Figure 4.12 Ratio of energy shift to Lorentzian broadening ($\Delta\omega/\Gamma_L$) as a function of laser power. The data is inconsistent with the constant ratio of 0.182 expected for van der Waals interactions.

additional evidence that exciton-carrier, rather than exciton-exciton collisions are the main contributing mechanism.

4.6 Gaussian broadening

Photoluminescence spectra are always limited by spectral resolution due to instrumental constraints. This manifests itself in Gaussian broadening of the peaks and can be incorporated into a theoretical model by convoluting the lineshape with the Gaussian function. Mathematically, this is can be expressed as:

$$I_2(h\nu) = \int_{-\infty}^{\infty} I_1(h\nu') \cdot \frac{1}{\sigma\sqrt{2\pi}} \exp\left(-\frac{(h\nu' - h\nu)^2}{2\sigma^2}\right) d(h\nu'), \tag{4.12}$$

where I_1 and I_2 are lineshapes without and with the Gaussian broadening, $h\nu$ is photon energy and σ is the Gaussian standard deviation.

Other than instrumental broadening, there can also be intrinsic contributions to σ, such as isotopic inhomogeneity and other forms of lattice disorder. Cardona et al. [56] demonstrated, through Raman spectroscopy of isotopically enriched Ge samples, that the isotopic disorder

in natural Ge causes an additional Gaussian broadening of 0.0025 meV. This is discussed in more detail in Section 7.5.

The extent of Gaussian broadening in Ge PL spectra appears to be a rather contentious issue in the subject literature. Estimates for intrinsic Gaussian half width (after correcting for experimental set-up resolution) range from 0.31 [44], to 0.25 [38], to 0 meV [46]. There is also no agreement over the source of this broadening, although most studies hint at phonon related mechanisms (e.g. finite lifetime or dispersion) [38].

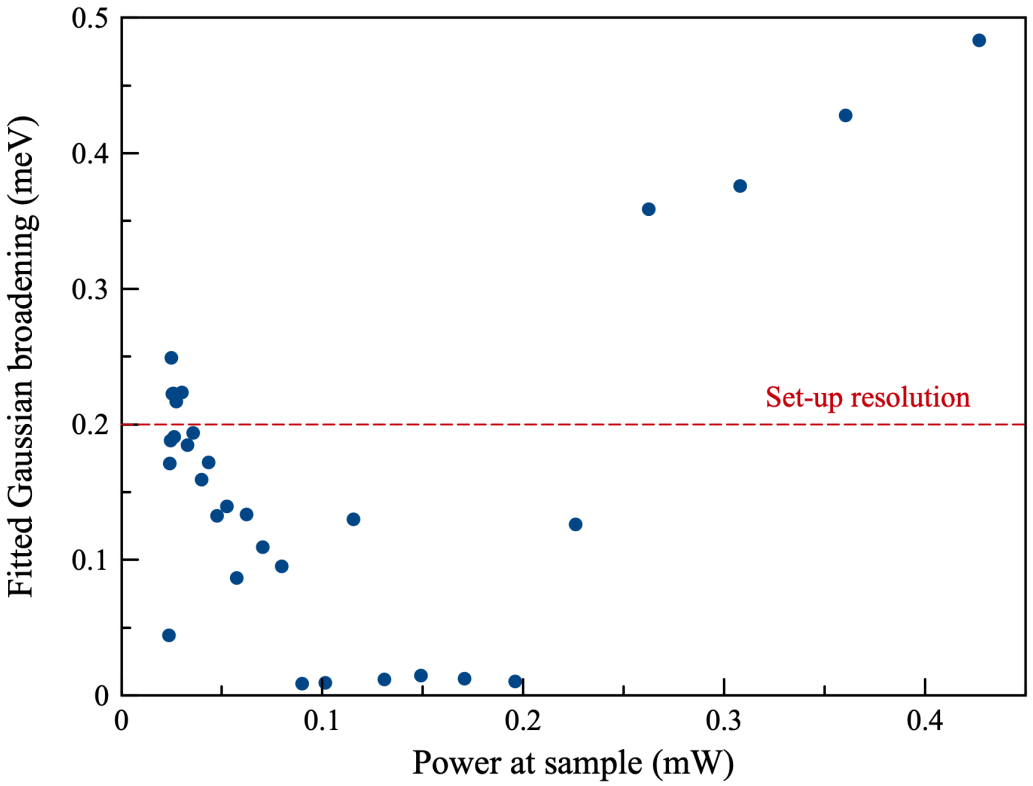

Figure 4.13 Gaussian broadening σ extracted from fits as a function of laser power. The non-physical behavior (including values below instrumental resolution) indicates that variations are artifacts of the fitting procedure.

Fig. 4.13 hints at the possible reason for these discrepancies in the literature. It shows σ extracted from the fits as a function of laser power for spectra measured without varying any other experimental parameters. The values in the plot must include the set-up resolution of $\sigma_{res} = (0.20 \pm 0.02)$ meV, which was not corrected for. At low photon incidence, σ takes the

value of $\sim 0.25\,\mathrm{meV}$, before dropping to almost zero. Then, it rapidly increases, significantly exceeding the initial value recorded at $P \approx 0$.

Typically, mechanisms responsible for Gaussian broadening of PL peaks do not show a strong power dependence. Furthermore, $\sigma < \sigma_{res}$ seen in the middle part of the graph is non-physical, as it would imply the existence of a negative contribution to σ. Regarding the increase at high power, visual examination of fitted spectra indicates that it originates from the fit trying to correct for the non-parabolicity of bands. For these reasons, variations seen in Fig. 4.13 can be deemed artificial and caused by the fitting procedure compensating for the deficiencies of the theoretical model.

There remains a question of how to approach Gaussian broadening while fitting Ge PL peaks. For the above reasons, the most sensible approach is to fix it at a constant value which encompasses the known contributions. The most important of those is the instrumental broadening which is $\sigma_{res} = (0.20 \pm 0.02)\,\mathrm{meV}$ for the spectra presented in this work. The broadening due to the isotopic composition of ^{nat}Ge is smaller by two orders of magnitude (see Section 7.5) and can be neglected for this specific purpose.

4.7 Complete model

Fig. 4.14 shows an indirect PL spectrum of Ge associated with LA, TO and LO phonons. It was fitted with a complete model outlined in this section, with the exception for the non-parabolicity correction. Each phonon mode was modeled as a doublet, to account for the energy splitting ΔE in the excitonic ground state. Intensity ratio of peaks within each doublet was set to $\exp(-\Delta E/kT)$ and each peak was modeled using Eq. 4.2 or 4.3, depending on the relevant selection rules. Lorentzian and Gaussian broadening was then applied using convolutions shown in Eq. 4.9 and 4.12. It should be stressed that the values of temperature T, Lorentzian broadening Γ_L and Gaussian broadening σ were identical for each peak and σ was fixed at the value corresponding to instrumental resolution. Furthermore, the energy splitting ΔE was fixed at 0.77 meV. The fit therefore involved 8 independent fit parameters: 3 peak amplitudes, 3 peak energy positions, Γ_L and T.

The model shows excellent agreement with the experimental data across 3 orders of magnitude. The only departures from the model are seen in the tails, due to the aforementioned non-parabolicity. Contribution to PL due to LO-assisted recombination is seen clearly, de-

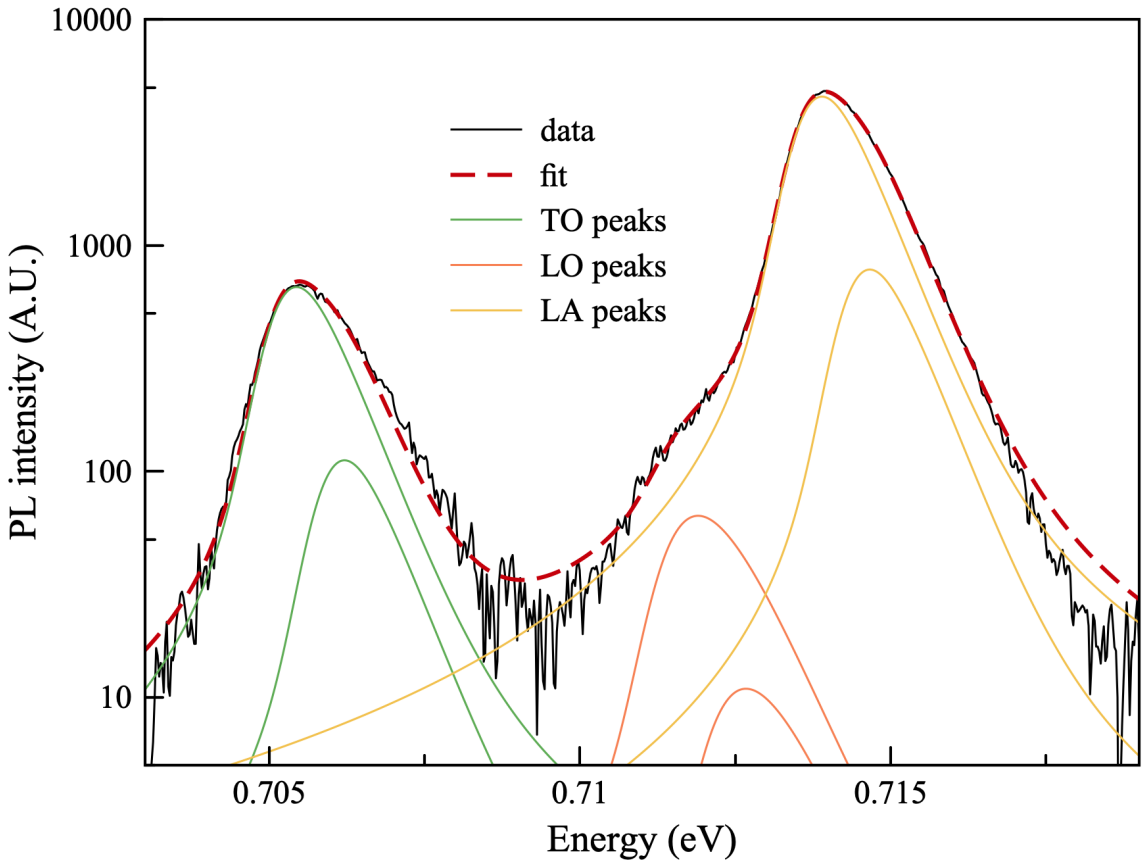

Figure 4.14 PL spectrum of Ge featuring TO-, LO- and LA-assisted emission lines. It was fitted with a complete model discussed in this chapter. The agreement with the theory is excellent with a slight deviation in the tails due to non-parabolicity. Extracted values for Γ_L and T were 0.20 meV and 5.1 K.

spite its proximity to the LA-assisted peaks. Extracted values for Γ_L and T were 0.20 meV and 5.1 K. Overall, the experimental data provides a strong validation of the theoretical model and allows an accurate determination of fundamental properties of Ge photoluminescence.

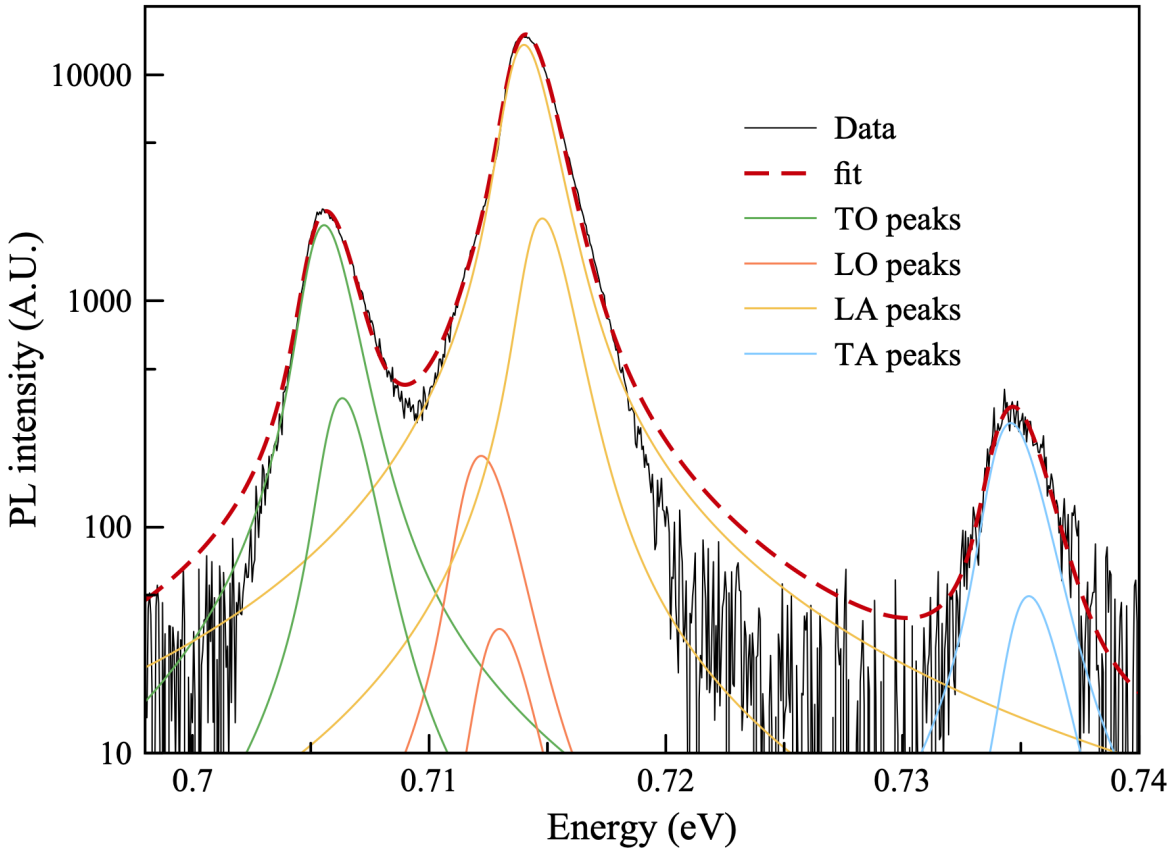

Figure 4.15 PL spectrum of Ge featuring TO-, LO-, LA- and TA-assisted emission lines. It was fitted with a complete model discussed in this chapter. The agreement with the theory is excellent with a slight deviation in the tails due to non-parabolicity. Extracted values for Γ_L and T were 0.51 meV and 6.4 K.

Fig. 4.15 shows an equivalent spectrum measured at higher power and with a broader spectral range. It includes the TA-assisted emission peak while the LO peak becomes less clearly visible due to the increased collisional broadening of adjacent peaks. The agreement with the model is still excellent although increased broadening led to a more pronounced deviation in the tails due to non-parabolicity of bands.

Applying the comprehensive indirect PL model has allowed to extract very accurate spectral information. Energy positions and peak intensities, relative to those of the LA-assisted emission peaks, are shown in Table 4.2. The uncertainties reflect not only the accuracy of a single fit, but were calculated by comparing several spectra. They are in agreement with the values of absolute phonon energies reported by Thomas et al. [57] to within 1 meV, although they did not provide explicit uncertainties.

Table 4.2 Relative energy positions and PL intensities of the peaks associated with different phonon modes in Ge spectra.

Quantity	Value	Uncertainty
$E_{TO} - E_{LA}$ (meV)	8.55	0.05
$E_{LO} - E_{LA}$ (meV)	2.4	0.3
$E_{TA} - E_{LA}$ (meV)	-20.1	0.1
I_{TO}/I_{LA}	0.143	0.005
I_{LO}/I_{LA}	0.017	0.005
I_{TA}/I_{LA}	0.025	0.002

4.8 Conclusions

The model of the indirect PL lineshapes in Ge presented in this chapter has followed the mathematical approaches proposed in various literature sources. The novelty of this work lies in the rigorous examination of each component and offering new insights into their origins. Firstly, new experimental methods were proposed to rigorously validate some established claims, specifically the allowed nature of the LA lineshape and the Lorentzian functional shape of the collisional broadening.

The value of the energy splitting in the excitonic ground state, $\Delta E = (0.77 \pm 0.05)\,\text{meV}$, was accurately extracted, which is notable as the previously reported values are somewhat inconsistent. The new method of calculating ΔE from the temperature dependence of relative amplitudes was possible to implement thanks to the excellent quality of the experimentally measured data. The resulting $\Delta E = (0.7 \pm 0.2)\,\text{meV}$ is consistent with the above value. Its uncertainty is larger, but using two independent methods makes the analysis qualitatively more compelling.

The examination of the collisional broadening led to a conclusion which contradicts the existing literature, namely that it is predominantly caused by the exciton-free carrier, rather than exciton-exciton interactions. The strongest validation of this interpretation comes from the power dependence analysis, particularly from the demonstration of the $I_{PL} \propto \Gamma_L^2$ relationship in the nonlinear I_{PL} regime. Temperature dependence and the behavior of the $\Delta\omega/\Gamma_L$ ratio provide further evidence, the latter being inconsistent with the van der Waals interaction potential. It was also shown that the data from the relevant literature is consistent with this explanation.

Section 4.6 provided some clarification as to why reported σ values show a high level of inconsistency. It was demonstrated that the fitted σ is extremely sensitive to small experimental variations and other fit parameters, leading to effectively arbitrary values. No evidence has been found to report statistically significant Gaussian broadening exceeding the expected value for the set-up resolution.

The detailed understanding of the model and its components was used to analyze carefully measured indirect PL spectra of Ge and extract relative peak positions and intensities. The values were consistent with previous literature reports and offered an improvement in terms of the measurement uncertainties. The model was also the foundation for the comprehensive analysis of other aspects of PL in Ge, presented in the upcoming chapters.

CHAPTER 5 INFLUENCE OF EXCITATION CONDITIONS ON INDIRECT PL IN Ge

The previous section described, in detail, spectral lineshapes of phonon-assisted indirect PL in Ge. It was demonstrated how these lineshapes directly originate from the band structure and from the properties of the charge carrier population induced in the material, particularly carrier densities and temperature. This section will explore the impact of excitation parameters: laser wavelength, incident power, numerical aperture and sample temperature on the resulting carrier populations and, accordingly, on photoluminescence.

Photoexcited charge carriers in semiconductors thermalize to band edges on a timescale of less than a picosecond. This is much shorter than a typical radiative lifetime which falls in the ns–μs range, depending on the sample quality and the nature of the band gap. Consequently, the type of the radiative recombination mechanism is not directly affected by excitation parameters as, by the time recombination occurs, individual carriers have lost any memory of the absorption and thermalization stages.

However, these parameters do have an impact on the efficiency and spectral dispersion of radiative recombination in several important ways. For example, high incident power increases charge density, enhancing PL yield while introducing collisional broadening and potential sample heating. This chapter will discuss such quantitative aspects of PL to complement the qualitative model introduced in Section (ref. to the section on lineshapes).

The first section will quantify the role of illumination NA in determining the spatial distribution of charge carriers and what it reveals about carrier diffusion in Ge. Equipped with this understanding, the following section will discuss the impact of laser wavelength and incident power on photoluminescence spectra. It will be argued that interactions with defects during absorption and thermalization stages are crucial to understanding this impact.. Finally, several temperature-related aspects of PL will be described, including T dependence of I_{PL}, low T condensation of carriers and laser heating.

5.1 Numerical aperture of the excitation

Germanium exhibits very strong carrier diffusion compared to similar semiconductors, such as Si [58]. Even at room temperature, diffusion length for an electron can reach several millimeters [59], depending on the sample quality. This is larger than typical beam waists used for sample excitation in PL measurements. Consequently, the equilibrium spatial distribution of carriers under laser illumination is dominated by lateral out-diffusion, rather than the size of the excitation spot. This has important implications for the overall PL yield as well as the collisional broadening observed in the spectra.

The effect of out-diffusion on PL intensity can be seen experimentally by comparing two curves in Fig. 5.4, specifically the ones labelled "1059 nm + objective" and "1059 nm + lens". Excitation numerical apertures were 0.42 and 0.006 respectively for the objective and the lens. This represents a vast difference in focusing power and, if diffusion weren't the limiting factor, it would lead to an equally vast difference in the induced carrier density. One would then expect to see a much higher signal intensity with the objective due to its focusing power. Instead, PL intensity is comparable for both curves – in fact, using the lens yielded more signal than the objective by a factor of ~ 1.4.

This can be understood within the diffusion model developed by Menendez et al. [36], briefly mentioned in the preceding section. They start with the diffusion equation:

$$-D\left[\frac{1}{r}\frac{\partial}{\partial r}\left(r\frac{\partial n}{\partial r}\right)+\frac{\partial^2 n}{\partial z^2}\right]=G(r,z)-\frac{n}{\tau}, \tag{5.1}$$

where D is the diffusion coefficient, n is the excess carrier concentration, τ is the recombination lifetime and the carrier generation rate $G(r,z)$ is given by:

$$G(r,z)=\frac{\alpha I_{\max}(1-R)}{\hbar\omega}\exp\left(\frac{-2r^2}{w_0^2}\right)e^{-\alpha z},$$

where α is the absorption coefficient, I_{max} is the laser beam intensity, R is the sample reflectance and w_0 is the beam waist at the focal point. They then proceed to calculate the average excess carrier concentration $\overline{n}(z)$ by integrating Eq. 5.1 over the r coordinate and solving the resulting differential equation. The expression thus obtained is:

$$\overline{n}(z) = \left[\frac{(1-e^{-2})P_0}{\pi w_0^2}\right]\left(\frac{L_{\text{eff}}^2}{D}\right)\frac{\alpha(1-\mathcal{R})}{\hbar\omega(\alpha^2 L_{\text{eff}}^2-1)} \times \left[\left(\frac{s_0+D\alpha}{s_0+D/L_{\text{eff}}}\right)\exp\left(-\frac{z}{L_{\text{eff}}}\right)-e^{-\alpha z}\right], \tag{5.2}$$

where s_0 is the surface recombination velocity and L_{eff} is given by:

$$\frac{1}{L_{eff}^2} = \frac{1}{D\tau} + \frac{8}{3w_0^2}.$$

The meaning of Eq. 5.2 is not immediately obvious. Intuitively, it can be understood as follows: tightening of the beam waist ω_0 changes the balance between lateral (r) and inward (z) diffusion, the former becoming more favorable. This is because the lateral spread of the photocreation events becomes smaller, leading to a steeper gradient $\frac{\partial(n)}{\partial r}$. As a result, while the carrier density near the surface becomes elevated, it falls off with z more quickly. $\overline{n}(z)$ values were computed by Simon Michel, a PhD studnet in the Engineering Physics department, for the lens and the objective used in this work. They are shown in Fig. 5.1 for the case of 1059 nm illumination and exhibit the behavior outlined in this paragraph.

Relative PL intensities can be obtained by integrating n^2 over the collection volume and the numerical aperture. In the context of this work, this calculation led to the similar order of magnitude of I_{PL} for both the lens and the objective, although the experimentally measured ratio of ~ 1.4 was not achieved (the calculation yielded 0.4). This discrepancy may be due to factors affecting PL such as surface effects and laser heating which are challenging to simulate. Nevertheless, the diffusion model successfully explained why I_{PL} measured with the objective is not vastly larger than that collected with the lens.

There is, however, a more direct way of assessing the effect of the excitation NA on $\overline{n}(z)$ which relies on the theory of collisional broadening presented in Section 3.2 and experimentally validated in Section 4.5. The Lorentzian half width Γ_L is proportional to the excess carrier density, or, more precisely, to its weighted average over the collection volume.

Fig. 5.2 shows Γ_L as a function of the square root of the illumination power. Two curves correspond to measurements conducted using an objective and a lens. Note that two NA

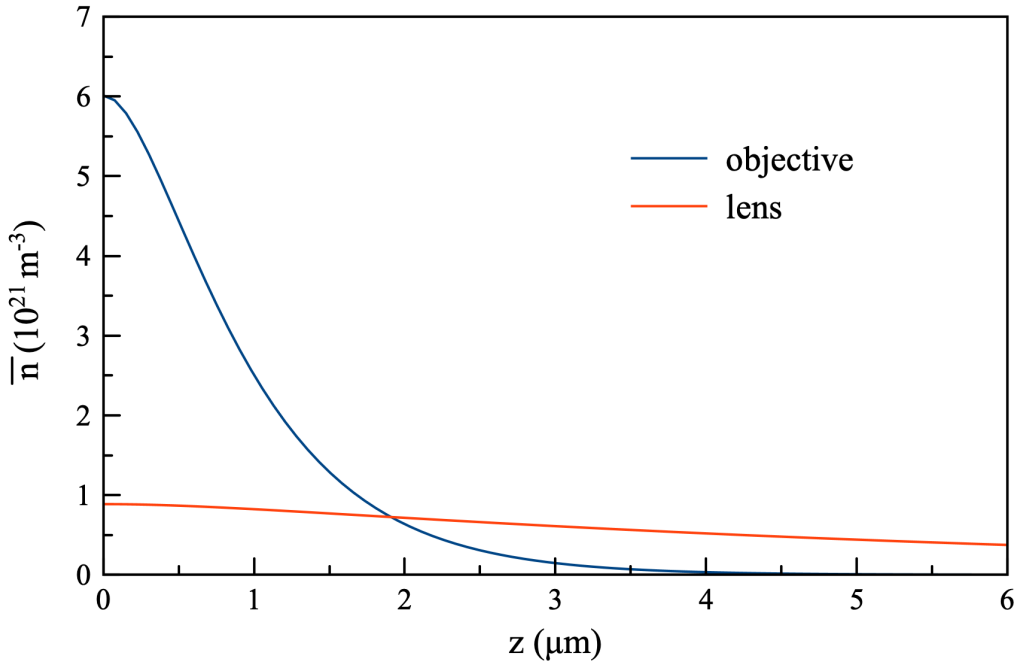

Figure 5.1 Average excess carrier density in Ge under 1059 nm illumination for the objective and the lens used in this work. Values computed using Eq. 5.2 by [60].

values are given for the lens - this is because the width of the incoming beam is much smaller than the lens diameter. Therefore, effective NA values for illumination and PL collection differ. For the objective, the laser beam was adjusted to match the entrance pupil leading to uniform NAs.

As expected for 1059 nm illumination, given the discussion in Section 4.5, Γ_L is proportional to the square root of laser power with the proportionality coefficients of 0.34 meV mW$^{-1/2}$ for the objective and 0.19 meV mW$^{-1/2}$ for the lens. This indicates that the observed collisional broadening is stronger with the objective, by a factor of 1.8. Again, the first conclusion to be drawn is that the difference is quite small compared to the large disparity in NA. Given that Γ_L is a direct measure of the excess carrier concentration, this result constitutes a clear demonstration that carrier dynamics in Ge under laser illumination are chiefly governed by diffusion.

In order to quantitatively compare the theoretical diffusion model to the experimentally acquired data, $\overline{n}$ values in Fig. 5.1 must be averaged over the collection volume. The expression

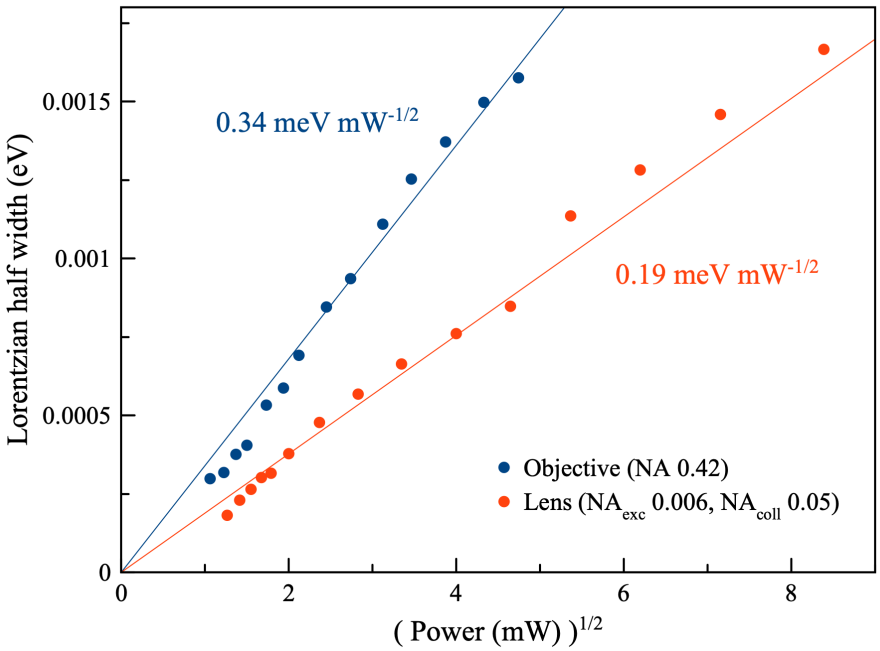

Figure 5.2 Lorentzian half width as a function of square root of laser power measured with an objective (blue) and a lens (red). Two NA values are quoted for the lens as the laser beam was significantly smaller than its aperture.

used for the calculation was

$$\Gamma_L \propto \overline{n}_{av} = \frac{\int_0^\infty \overline{n}(z)^3\, e^{-\alpha z}\, \eta_{\mathrm{coll}}(z)\, dz}{\int_0^\infty \overline{n}(z)^2\, e^{-\alpha z}\, \eta_{\mathrm{coll}}(z)\, dz}, \tag{5.3}$$

where α is the absorption coefficient and η_{coll} is the optical collection efficiency. Eq. 5.3 accounts for several important factors:

- Most PL signal (the intensity of which is proportional to n^2) originates from high carrier concentration regions. Therefore, the average is weighted by n^2.
- Self-absorption is accounted for by modulating the average with $e^{-\alpha z}$.
- Depth of focus depends on the excitation NA so the z-dependent collection efficiency $\eta_{coll}(z)$ is considered.

The ratio of Γ_L values (due to the objective and the lens) calculated using Eq. 5.3 is 7.0. This is significantly higher than the experimentally observed 1.8 which may have been caused by neglecting surface effects in the model. n^2 weighing means that the $\overline{n}_{av}$ value computed for the objective is dominated by the region very close to the sample surface (within $\sim 0.5\,\mu$m). Additional non-radiative recombination channels may be available there, which would mean that the actual contribution to the PL from that region is lower than expected.

In conclusion, the diffusion model correctly accounts for a relatively small impact of the illumination NA on the excess carrier concentration n in Ge. The calculated ratios of PL intensities:

$$\frac{I_{PL}^{lens}}{I_{PL}^{obj}} = 0.4$$

and Lorentzian half widths:

$$\frac{\Gamma_L^{obj}}{\Gamma_L^{lens}} = 7.0$$

both seem to overestimate n due to the objective, as evidenced by the experimentally measured values of 1.4 and 1.8 respectively. The practical recommendation stemming from this section is to use a low NA excitation for photoluminescence from bulk Ge in order to maximize signal yield and minimize collisional broadening.

5.2 Incident wavelength and power

PL measurements in this work were primarily executed using 1059 and 532 nm CW lasers (with an occasional use of 633 and 790 nm). In the course of these measurements, important differences between these wavelengths became apparent in regard to PL yield and its power dependence. This section will present the relevant data, compare them to existing literature and offer new insights into the underlying physical phenomena.

An important observation which must be emphasized before any further analysis is that all PL spectra discussed in this chapter were consistent with the model of phonon-assisted indirect photoluminescence presented in Chapter 4. They varied in amplitude, temperature broadening, collisional broadening and power dependence but otherwise they were functionally identical and it was not possible to determine which laser was used based on a single spectrum. This indicates that the recombination mechanism was unaffected by excitation conditions. Any differences must stem from absorption or thermalization stages which is when charge carrier population is established.

Furthermore, it should be pointed out that the total incident laser power, rather than power density, is discussed throughout this section. This is a deliberate choice which stems from the importance of diffusion in Ge, discussed in the preceding section. Increasing the excitation spot from $\sim 1\,\mu$m to $\sim 100\,\mu$m changes power density by four orders of magnitude but has a very limited impact on the resulting charge carrier distribution, and thus on PL characteristics. Power density can therefore be a very misleading parameter in this particular semiconductor.

The standard approach to characterizing power dependence of PL intensity is via an exponent k defined by the following power law:

$$I_{PL} \propto P^k,$$

where P is the total intensity of incident laser light. Detailed discussion of k exponent theory based on a model proposed by Spindler et al. [26] is presented in section 3.3. This formalism will be used to facilitate the forthcoming discussion.

5.2.1 Experimental results

Fig. 5.3 shows the typical behavior of photoluminescence intensity I_{PL} emitted by Ge samples used in this thesis. Data points were obtained by integrating total intensity associated with four different phonon modes (TO, LO, LA and TA). It should be noted that relative intensities of the peaks did not show any power dependence, indicating that the trends shown in Fig. 5.3 are also representative of each peak individually.

Fitted lines are accompanied by their logarithmic slopes which correspond to k exponents in power dependence. Note that the number of incident photons, rather than total incident power, is plotted on the x-axis. This allows for a more meaningful comparison between different wavelengths as the number of photons is directly correlated with the number of photocreated carriers.

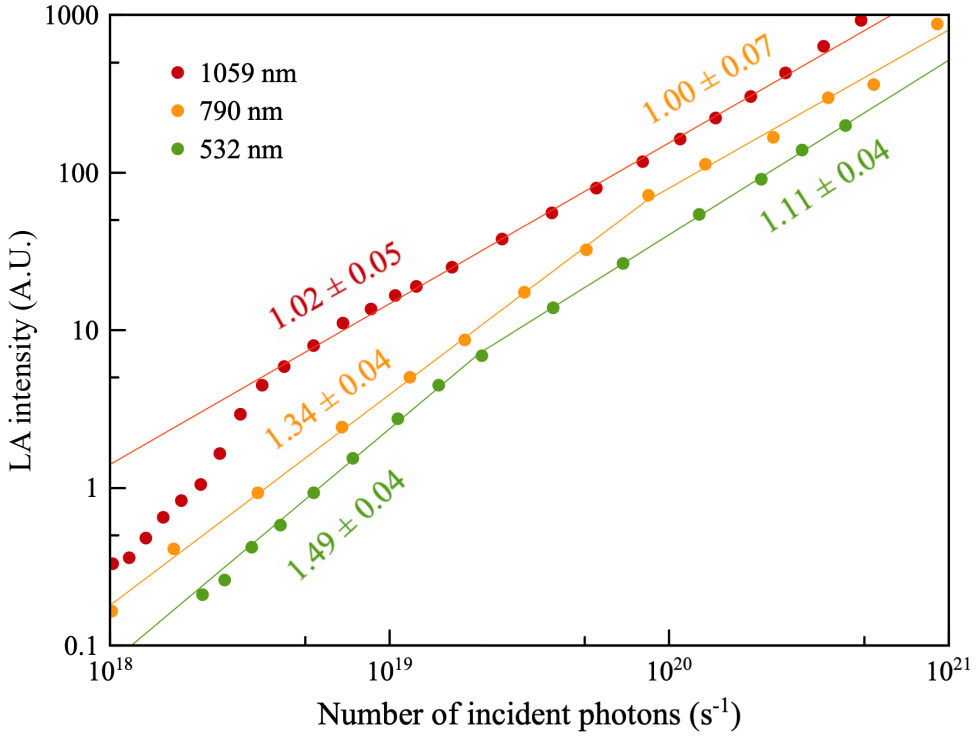

Figure 5.3 Power dependence of total Ge indirect PL intensity for different excitation wavelengths. Logarithmic slopes, which represent power exponents, are shown for trends which were replicable.

One trend which immediately catches the eye is the increase in overall PL yield as the

excitation wavelength increases. The 1059 nm excitation is the most efficient of the three sampled wavelengths. It exhibits a linear power dependence with an exponent k of 1.02, a typical behavior for an exciton-like transition [26]. However, at low number of incident photons, there is a clear deviation from this trend as PL intensity is below the trend line and it rises superlinearly. This is a local effect (associated with local defect density) and its extent varies strongly with the position on the sample. In many measurements, it was not seen at all. As such, it is of less interest than the ubiquitous and replicable linear trend and will not be discussed further.

790 nm and 532 nm illumination leads to a different power dependence. PL intensity is significantly lower and rises superlinearly with power exponents of 1.34 and 1.49 respectively. However, at high incident photon numbers, both exponents are reduced to $\sim$1. Based on multiple measurement runs, it can be reported that the crossover point varies with the position on the sample and possibly also with temperature. Occasionally, it would not occur at all within the available incident power range.

It should be noted that the exponents of $\sim$1 for 1059 nm and $\sim$1.5 for 532 nm illumination (at moderate laser power values) have been replicably observed regardless of the isotopic composition, sample temperature or excitation NA. Fig. 5.4 shows PL power dependence curves obtained from ^{72}Ge using both laser wavelengths while varying other excitation parameters. Between the measurements, the excitation NA was changed from 0.01 to 0.42 and the platform temperature in the cryostat was increased from 5 K to 25 K. Power exponents were unaffected which means that wavelength is indeed central to understanding this disparity.

Attempts to use 633 nm excitation yielded no observable PL, despite using incident power at which the other three lasers produced easily detectable signal. Misalignment was not a likely cause either as an accurate aligning procedure was employed. In it, PL due to 1059 nm was observed in real time as 633 nm beam was scanned across the sample. As the two laser beams coincided, a drop in PL amplitude was seen due to additional laser heating (data thus collected are presented and discussed in Section 5.3). This drop was used as a metric for the overlap between the two lasers. This in turn ensured an excellent overlap between the 633 nm laser and the collection spot and yet, PL signal was never detected.

Lorentzian broadening (which originates from collisions, as explained in Section 3.2) also ex-

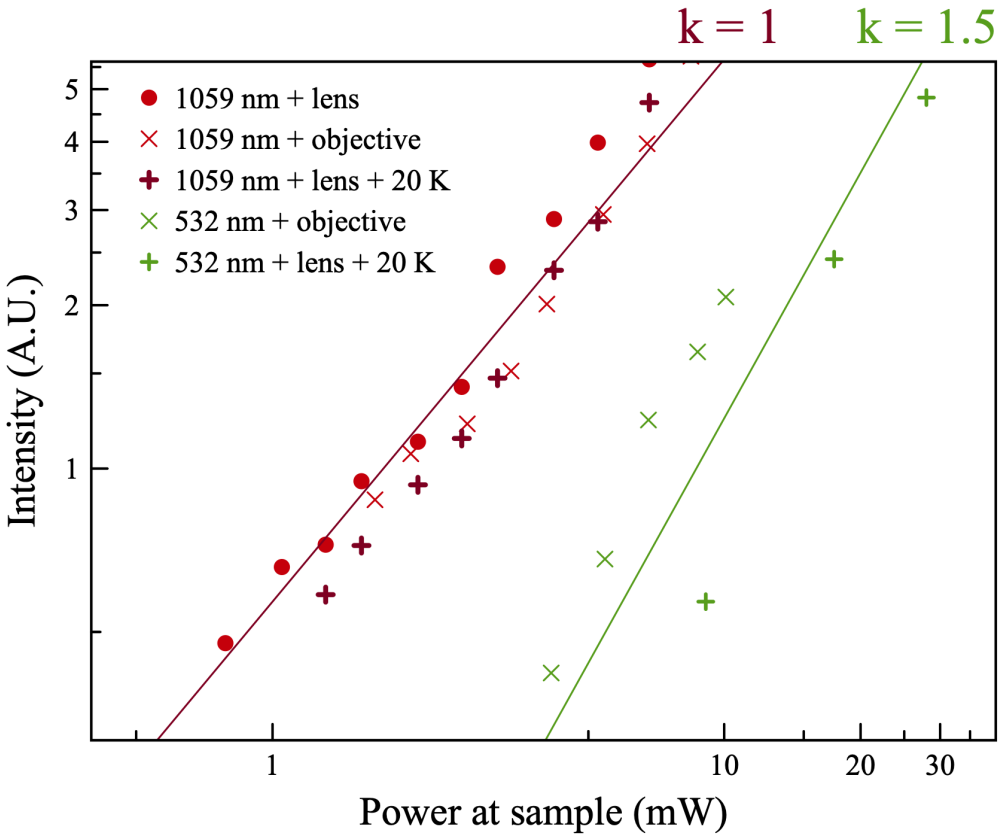

Figure 5.4 Power dependence curves measured on ^{72}Ge under different excitation conditions: 1059 nm or 532 nm laser wavelength, NA 0.01 lens or NA 0.42 objective, 5 K or 25 K platform temperature. Power exponents $k \approx 1$ for 1059 nm and $k \approx 1.5$ for 532 nm are observed irrespective of other parameters.

hibits power and wavelength dependence. As shown in Fig. 5.5, for 1059 nm excitation, broadening increases with a power exponent of 0.54. When the 532 nm laser is used, Lorentzian half width is lower and exhibits an exponent of 0.63.

This concludes the presentation of experimental results pertaining to the impact of incident laser wavelength and power on PL characteristics. The upcoming section will discuss the most commonly referenced models of PL power exponents in semiconductors to provide the initial context for these findings.

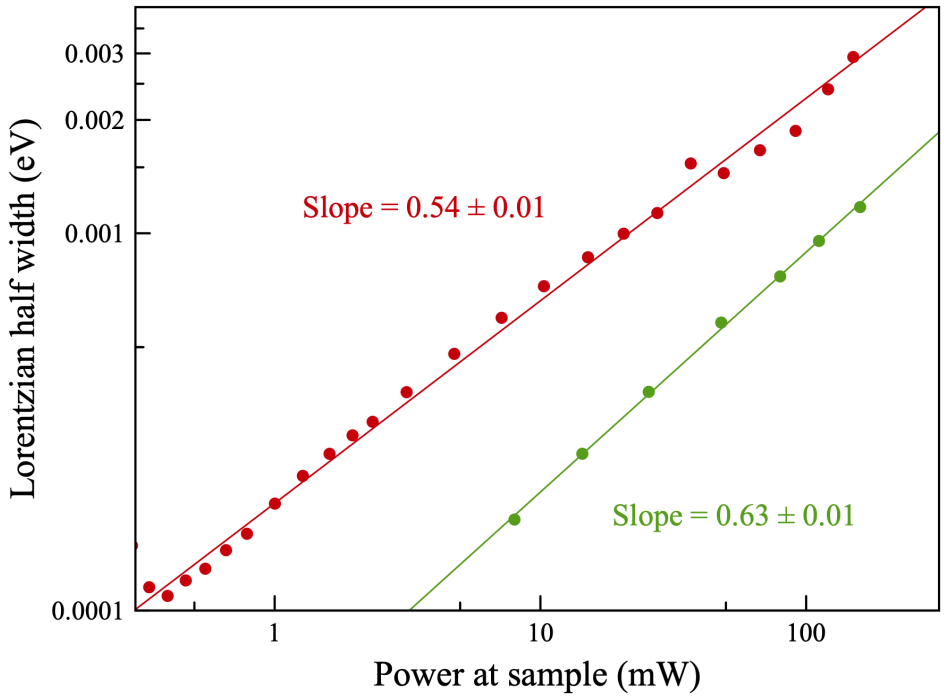

Figure 5.5 Lorentzian broadening comparison for 1059 nm and 532 nm excitation. Power exponents of 0.54 and 0.63 were measured respectively.

5.2.2 Power exponent models

The foundational study for modeling power dependence of semiconductor PL was presented by Schmidt et al. [25] in 1992. In it, they analyzed a set of rate equations representing a variety of possible optical transitions. The model (see Section 3.3 for details) was later augmented by Spindler et al. [26] to include deep defect transitions. This extended framework will form the basis for the interpretation that follows.

Power exponent of $k = 1$ measured for 1059 nm can be easily understood within Spindler model. It is the basic case of an exciton-like transition where power dependence is unaffected by defect saturation. That is not to say that defects play no role - in fact, Ge shows poor radiative efficiency and most carriers do recombine non-radiatively. $k = 1$ still holds true as long as the proportion of carriers recombining radiatively does not change with excitation power.

A transition from $k \approx 1.5$ at low incident power to $k \approx 1$ at high power is another standard case. Inititally, acceptor or donor states are available which efficiently capture charge carriers. As power increases, these defects gradually saturate, increasing the probability of radiative recombination. Eventually, $k = 1$ behavior is recovered when all defects are occupied. This explains the data collected for 532 nm excitation.

790 nm excitation led to an intermediate behavior, both in terms of PL yield and power exponent. According to Spindler et al., k-exponents are multiples of 1/2 and intermediate values indicate the transition between limiting cases of linear power laws. They do not discuss excitation wavelength dependence of k.

Schmidt et al. [25] do offer a possible explanation for increased k at lower wavelengths (they use it to explain CdTe PL spectra [61]). They claim that a high incident photon energy increases the probability of exciton dissociation into a free electron and hole, leading to an increase in the power exponent. Near-resonantly created excitons are less likely to dissociate and exhibit $k \approx 1$. It is important to underline that they don't claim that dissociation intrinsically causes an increase in k. Rather, it makes interactions with defects more abundant, affecting carrier lifetimes and, indirectly, power exponents.

In any case, data presented in this thesis directly contradicts this rationale. Fig. 5.5 showed the power dependence of Lorentzian half width γ under 1059 nm and 532 nm excitation. (Section 3.2 demonstrated that γ is proportional to the free electron/hole density n.) γ, and therefore n, is even higher for 1059 nm excitation than for 532 nm. Explanation offered by Schmidt et al. would require negligible γ to explain $k = 1$. While their explanation may well be correct in other systems, it is not applicable to Ge PL as presented in this thesis.

Having introduced a robust model of power exponents for semiconductor PL, the next section will review the existing literature pertaining directly to the indirect photoluminescence from Ge. It will be compared to the Spindler model as well as the experimental data reported in this thesis.

5.2.3 Literature review of Ge PL

Considering industrial and scientific importance of Ge, studies which discuss power dependence of its bulk PL are scarce and usually offer only a brief discussion. Some works show power dependent spectra but do not present integrated data [62,63] which makes it challenging to compare their results to other sources. No study has been identified which spanned a large enough incident power range to showcase more than one k exponent.

W. Klingenstein and H. Schweizer [64] measured a power exponent of 1 for indirect Ge PL under 1064 nm excitation. This result is in excellent agreement with the data presented in this thesis. Interestingly, they report a different exponent of 1.6 for direct PL. They attribute it to an Auger-like mechanism responsible for populating the Γ valley minimum, from where direct recombination occurs. Auger processes involve 3 charge carriers which leads to an exponent of $3 \times 0.5 = 1.5$ under these experimental conditions.

Lieten et al. [47] obtained an exponent of 2.02 from their indirect Ge PL spectra measured with a 514 nm laser source. They point to a much lower excitation power density they used to explain the difference between their result and $k \approx 1$ [64] discussed in the preceding paragraph. However, some of the data presented in this thesis was measured at a comparable power density at a similar wavelength of 532 nm and yielded $k \approx 1.5$. A more likely explanation for $k = 2.02$ is the fact that the sample used by Lieten et al. was Sb-doped providing more abundant impurities. If an additional defect type was introduced by doping, the power exponent may have been increased by a further 0.5. Indeed, the exponent of an exciton-like transition can reach the value of 2 when two different defect states are present (e.g. acceptor and donor, or shallow and deep acceptor).

Arguirov et al. [65] obtained a power exponent of 1.4 from their measurements of Ge PL. Excitation wavelength is not mentioned in their work although their result is reminiscent of 532 nm and 790 nm curves in fig. 5.3. Incorrectly, they used $k = 2$ as a starting point

to explain their finding - they assumed that electron and hole densities $n_{e/h}$ are linearly proportional to laser power P which would lead to $k = 2$ due to $I_{PL} \propto n_e n_h$. In reality, while photocreation rate is proportional to P, n_e and n_h are proportional to $\sqrt{P}$ - a common source of confusion addressed in more detail in Section 3.3. Subsequently, the authors rather unconvincingly suggested that Auger recombination is responsible for the exponent being lower than 2. In reality, if Auger recombination were dominant, PL intensity would exhibit $k < 1$ [66].

Menendez et al. [36] published a comprehensive and compelling model of Ge indirect PL which includes a discussion of spatial diffusion of carriers in Ge. They derived an expression for excess carrier density which can be used to calculate power dependence of I_{PL}. However, since they assumed P-independent carrier lifetimes, their derivation yielded $n_e \propto P$. This would lead to a $k = 2$ exponent for PL which is not consistent with experimental results of this work. Fortunately, this discrepancy does not affect the validity of the spatial dimension of their model (which will be used later in this chapter).

5.2.4 Discussion

Existing literature can explain many aspects of the power dependence data acquired in this thesis. It does not, however, offer a satisfying explanation for the wavelength variations. This section will attempt to demonstrate that the λ-dependence of penetration depth, leading to a varying degree of defect interactions, offers the most compelling justification for them.

According to the Spindler model, $k > 1$ for an exciton-like transition implies interactions with defects which saturate at stronger excitation power. One can devise an explanation involving lifetime variations or the degree of exciton dissociation but they all ultimately rely on said defect interactions. The key question posed in this section is therefore: why do lower wavelengths tend to interact with defects in Ge more strongly?

A natural starting point is the comparison of optical properties of Ge for different values of λ used in this study. Fig. 5.6 shows a band diagram of Ge calculated using $k \cdot p$ theory at 4 K [3, 36]. Colored arrows represent photon energies associated with the four lasers used in PL measurements. Only the dominant transitions are shown for each λ, determined by the local curvature of bands (low curvature is associated with a higher density of available states).

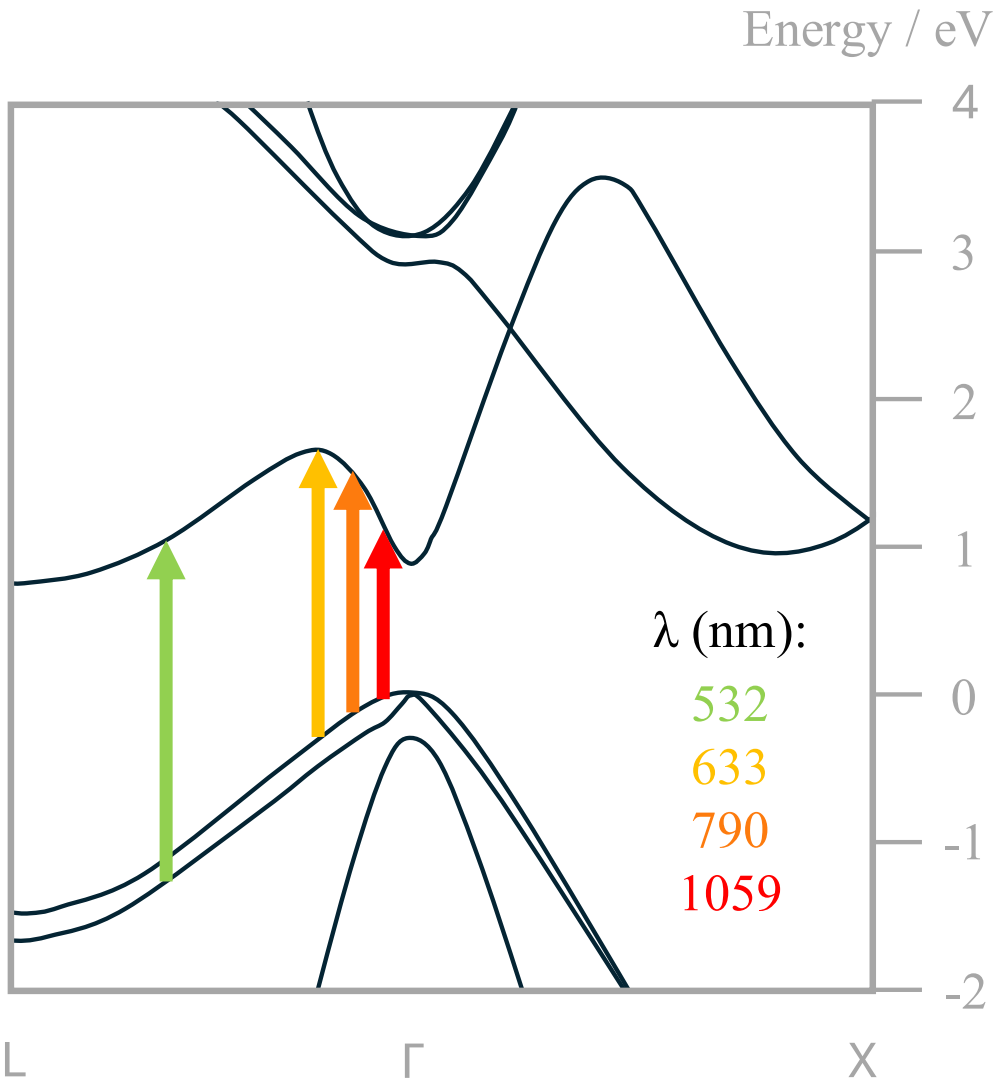

Figure 5.6 Ge band diagram at 4 K (data from [3, 36]) showing dominant absorption routes for 532, 633, 790 and 1059 nm photons.

The main observation is that 532 nm photons can bridge the gap in the L valley. Photocreated electrons can therefore thermalize directly to the L valley minimum. 790 and 1059 nm photons can only bridge the Γ valley and 633 nm excitation creates electrons very close to the local maximum. However, intervalley scattering occurs rapidly with a time constant of 1.2 ps [67] so electrons are expected to efficiently populate the L valley minimum regardless of λ.

Charge carriers are photocreated with excess energy which depends on the incident photon

energy. It is then lost during thermalization which occurs on the picosecond timescale [68]. Lower λ implies that a larger energy range is spanned by charge carriers during thermalization. However, it is unclear precisely how this could lead to a significant difference in the degree of defect interactions. In conclusion, Ge band diagram does not appear to explain λ variations described in Section 5.2.1

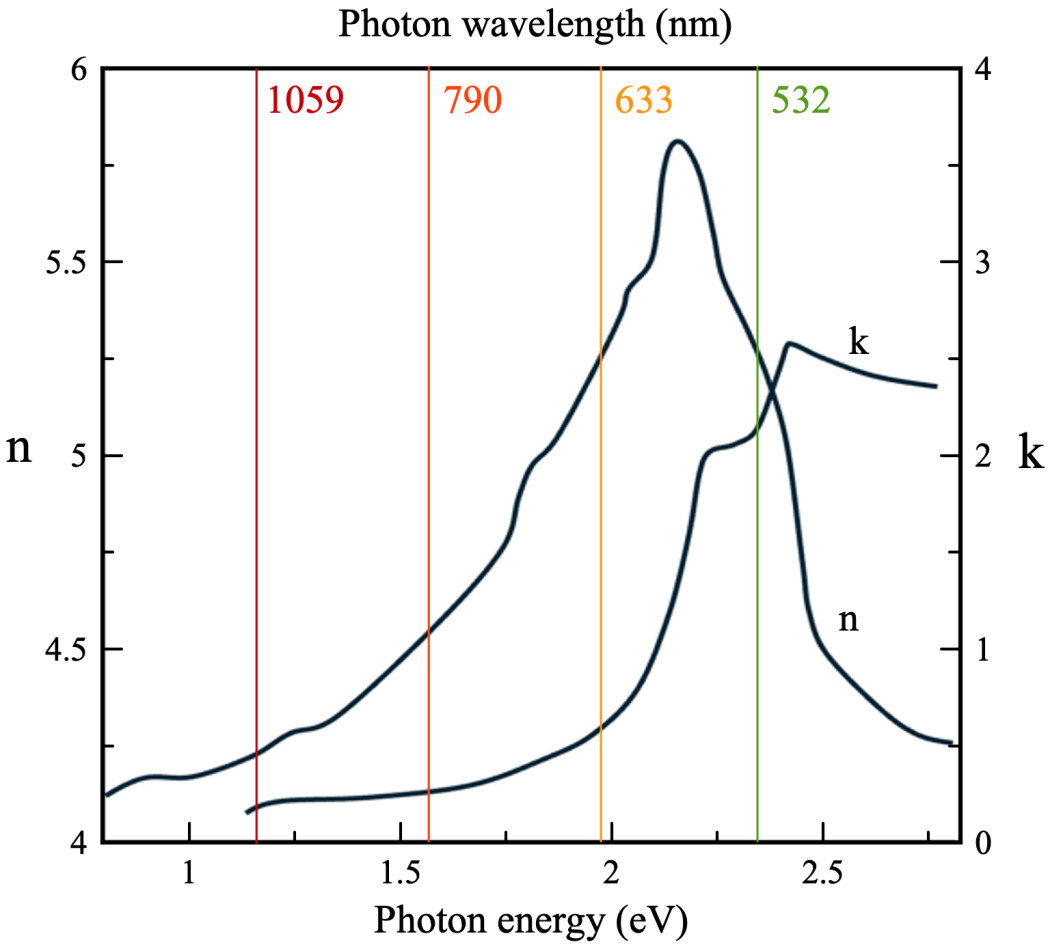

Figure 5.7 Spectral dependence of the refractive index n and the extinction coefficient k for Ge at 120 K (data from [69]). Colored lines represent 532, 633, 790 and 1059 nm photon energies.

Ge absorption varies dramatically in the visible part of the electromagnetic spectrum. Fig. 5.7 shows the spectral dependence of the refractive index n and the extinction coefficient k for Ge at 120 K [69]. Note that, at cryogenic temperatures, absorption features are expected to be narrower and shifted in energy (Varshni shift from 120 to 5 K is $\sim$ 16 meV [55]). The four λ values of interest are indicated on the plot for easier comparison.

From 1059 to 532 nm, n increases by $\sim 25\,\%$. This can (partially) explain differences in PL yield (higher refractive index leads to a higher reflection coefficient) but not the variation in power exponents. Extinction coefficient k changes more markedly in this spectral range, by more than an order of magnitude. This indicates that the penetration depth varies strongly between the four wavelengths. For proper comparison, absorption coefficient α was calculated for each λ value using experimental ε_1 and ε_2 values at 10 K [70]. The results are listed in Table 5.1.

Table 5.1 Ge optical absorption parameters at different wavelengths, calculated using ε_1 and ε_2 values at 10 K from [70].

Wavelength (nm)	ε_1	ε_2	α (μm^{-1})	Penetration Depth (nm)
532	21.5	23	52.7	19
633	27.5	5.9	11.1	90
790	21.3	2.1	3.61	277
1059	19	1	1.36	735

Across the wavelengths used for PL acquisition, penetration depth ranges from 19 to 735 nm. Not only is the variation significant, but it also occurs over depths where surface effects become important contributors to the exciton dynamics. Defect density near the sample surface tends to be much higher than within the bulk material - this can be particularly relevant in Ge which exhibits an unstable and defect-prone native oxide. Therefore, charge carriers excited by 532 nm photons encounter more defects in their absorption volume than those created with higher wavelengths. 1059 nm photons penetrate deep into the bulk where surface effects become negligible, leading to a power exponent of ~ 1. 790 nm photons probe both regions which explains an intermediate power exponent of 1.34. Variation in overall PL yield can likewise be justified through defect interactions which provide a competing non-radiative recombination path.

Observed trends in the power dependence of Lorentzian broadening Γ_L follow directly from those seen in PL intensity. Both quantities are related to free carrier density $n = n_e = n_h$ through:

$$\Gamma_L \propto n \quad \text{and} \quad I_{PL} \propto n^2. \tag{5.4}$$

It is therefore expected that power exponents of Γ_L will be half of those observed in Fig. 5.3. This is true for 1059 nm excitation where power exponents of 0.54 (broadening) and 1.02 (intensity) are noted. The relationship does not hold as well for 532 nm excitation with exponents of 0.63 and 1.49 respectively. Nevertheless, considering the many simplifications made in the derivation of 5.4, even this degree of correlation constitutes a strong evidence for the models presented throughout this thesis.

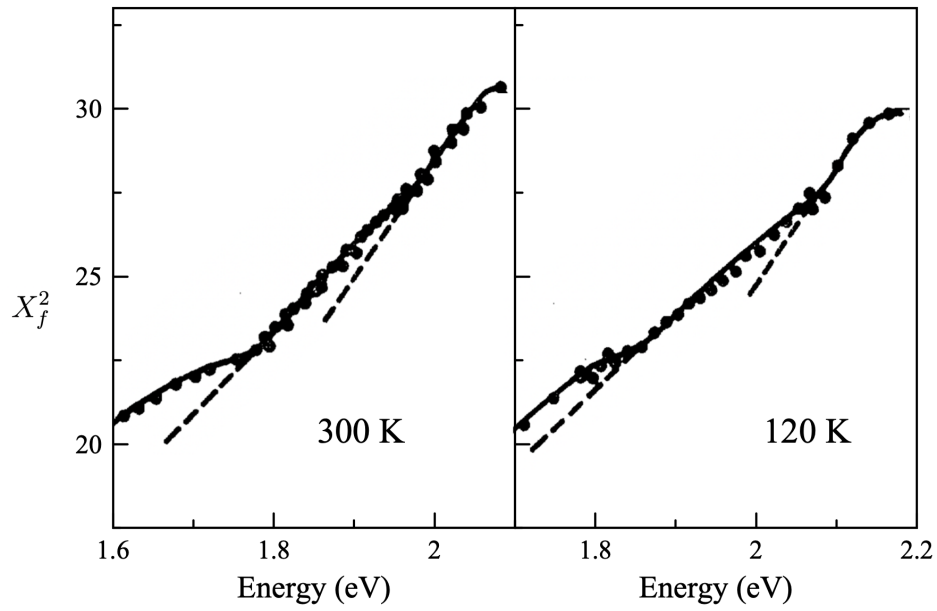

Figure 5.8 Spectra of X_f^2 (a reflectometry quantity calculated from the Brewster angle using Eq. 5.5) at 300 K and 120 K. Data from [69]. Structures in the spectra correspond to unidentified electronic transitions in Ge.

There remains a matter of the lack of PL emitted under 633 nm excitation which cannot be explained within the framework proposed above. However, 633 nm photon energy matches absorption features reported by R. J. Potter [69]. They are not visible in Fig. 5.7 (from the same work) but were resolved in the underlying reflectometry measurement. Fig. 5.8 shows spectral plots of the quantity X_f^2 at two different temperatures. It is calculated from the Brewster angle ϕ_b using the following expression:

$$X_f^2 = \sin^2 \phi_b \, \tan^2 \phi_b. \tag{5.5}$$

Two structures seen in the X_f^2 spectra correspond to the electronic energy transitions in Ge.

At the time, they were interpreted as transitions between L_1 and L_3' points in the Ge band diagram (direct absorption at L). Modern $k \cdot p$ calculations contradict this identification of the band structure transition but the presence of these absorption features remains a fact. It is possible that 633 nm photons resonantly interact with this unidentified transition limiting the number of carriers which can recombine radiatively.

In conclusion, surface defect interactions convincingly explain the data presented in this section. In order to further verify the validity of this model, measurements with an enhanced resolution in λ should be performed and quantitatively compared to penetration depth estimates. Such approach would also shed more light on the anomalous 633 nm excitation. Another potential future research direction is to study the impact of surface treatments on the power dependence of PL under 532 nm illumination.

5.3 Laser heating

The electronic temperature affects the PL lineshapes in several important ways. Firstly, it determines the Boltzmann distribution of carriers leading to thermal broadening inherent to indirect PL, as explained in Section 3.1.2. Secondly, it affects the population balance between the two levels of the excitonic ground state. It also impacts the total PL intensity, due to the thermal dissociation of free excitons. Other effects explored in this thesis include the variations in the collisional broadening with T and condensed phases of the exciton gas which can exist at low temperatures. A rigorous study of Ge photoluminescence must be able to discern between these mechanisms in order to isolate the phenomena of interest. It is therefore imperative to understand how experimental conditions affect the electronic temperature.

The electronic temperature is determined by the global sample temperature and laser heating. It became apparent in the course of measurements presented in this thesis that the quality of the thermal contact between the sample and the cryostat platform was extremely relevant. If the ability to extract heat from the sample was compromised, laser heating became very pronounced. This can be seen in Fig. 5.9 which shows electronic temperature (extracted from spectral fits) as a function of both platform temperature and laser power. T_{platform} sets the starting point at P=0, although not directly. For example, $T_{elec}(P = 0) \approx 10\,\text{K}$ when $T_{\text{platform}} = 5\,\text{K}$ owing to inefficient heat extraction. As the laser power is ramped up, heating increases linearly in laser intensity. The slope is dependent on the quality of the

thermal contact and T_{platform} as these two factors determine the thermal conductivity out of the sample.

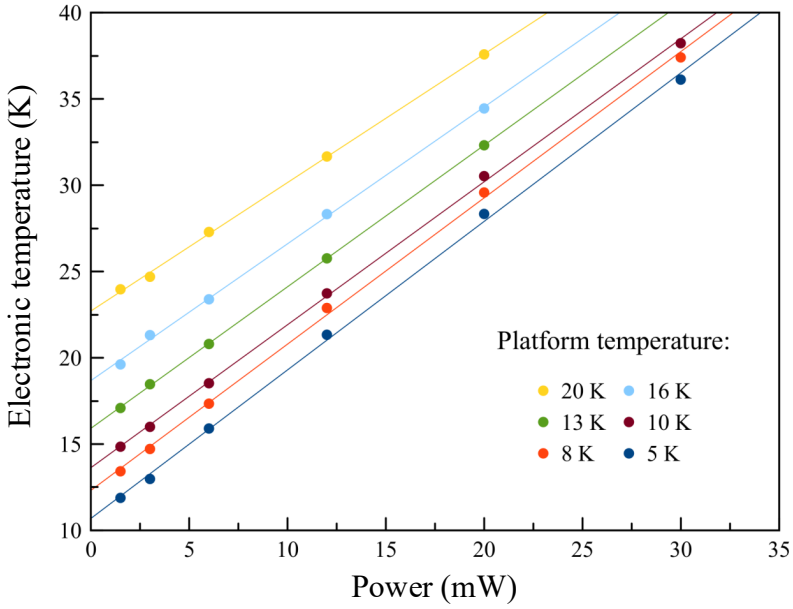

Figure 5.9 Electronic temperature as a function of the platform temperature and the laser power.

The linear dependence of the heating on laser power (rate of energy delivery to the sample) is expected. Only a small fraction of incident photons lead to the eventual radiative recombination in Ge. A constant fraction of them is reflected and the remaining majority is absorbed, before recombining non-radiatively and thus contributing to heating.

The aforementioned case of 633 nm illumination offered an interesting case to explore laser heating as it led to no observable PL but it did increase the temperature of the sample. This effect was observed via two-laser illumination – PL due to a fixed intensity of 1059 nm light was used as a probe for laser heating, as the 633 nm intensity was increased. Fig. 5.10a shows spectra recorded in this manner – there is a clear decrease in intensity and an increase in broadening. Detailed fits revealed that Lorentzian broadening did not increase (in fact, it reduced slightly) and temperature rise is the sole reason for the additional broadening of the peaks.

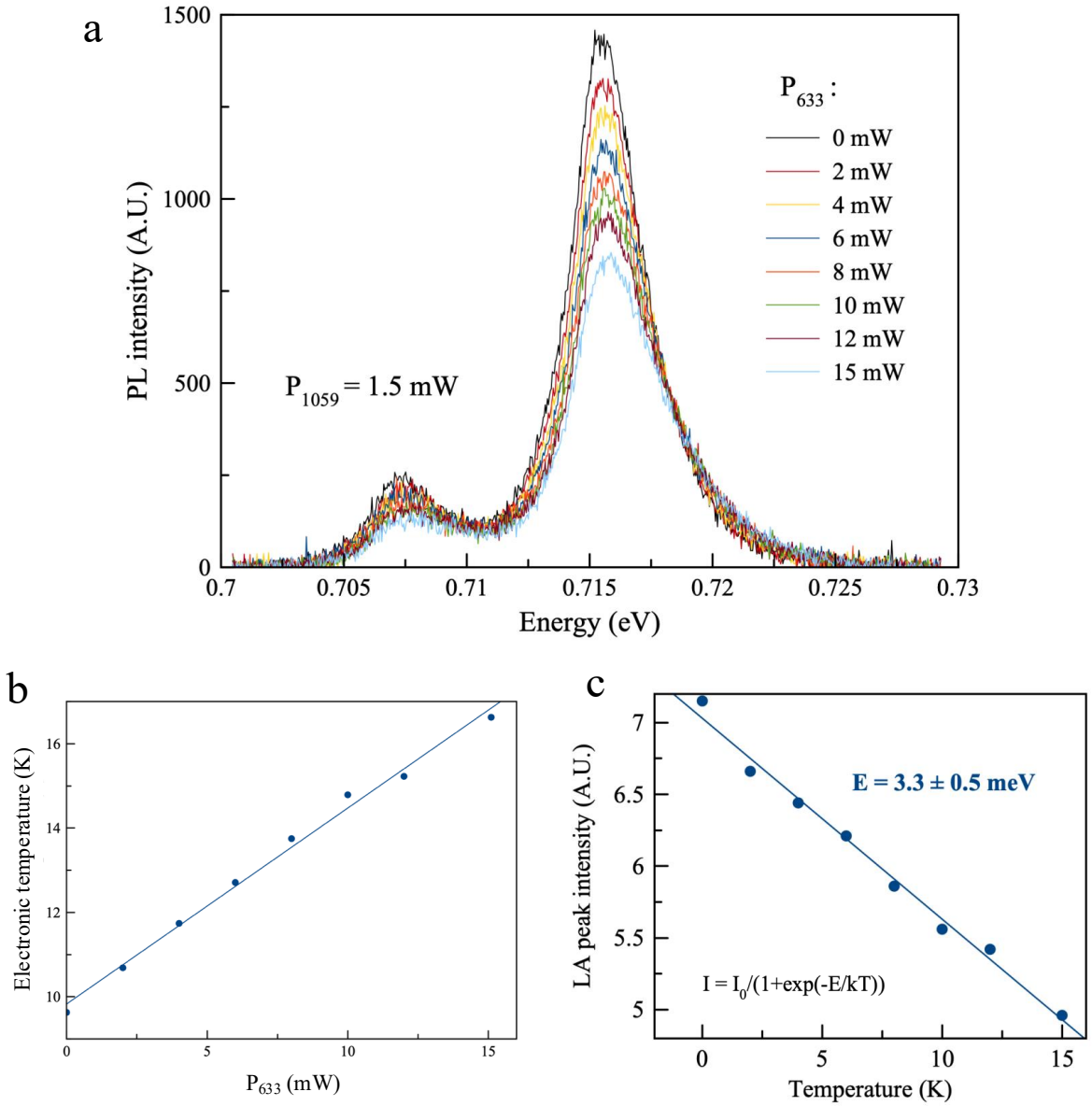

Figure 5.10 a) Spectra of natural Ge acquired via two-laser illumination, with a constant 1059 nm power of 1.5 mW and a varying level of 633 nm illumination. b) Electronic temperature extracted from lineshape fits showing a linear increase in P_{633}. c) Temperature dependence of PL intensity yielding $E_a = 3.3 \pm 0.5$ meV, consistent with the FE binding energy.

Electronic temperature increased linearly in P_{633} as shown in Fig. 5.10b. The decrease in PL intensity provided further evidence for the attribution of this effect to heating – the temperature dependence in Fig. 5.10c was fitted using the Arrhenius equation:

$$I(T) = \frac{I_0}{1 + A \exp\left(-\frac{E_a}{k_B T}\right)},$$

where I_0 is PL intensity at 0 K, A is a dimensionless constant and E_a is the activation energy of the quenching process. It yielded an E_a value of 3.3 ± 0.5 meV, consistent with the free exciton binding energy.

Significant laser heating, regularly observed in the PL measurements, was problematic as it limited the ability to consistently sustain low temperatures under illumination. Furthermore, it introduced a degree of variability between measurements performed on different samples and in different cryostat cooldowns. The results described in this section were crucial as they made it possible to rigorously monitor thermal effects throughout the research project.

5.4 Nonlinear carrier localization regime in low-power PL

An intriguing phenomenon has been regularly detected during the PL measurements in the course of this research project. Ge PL power dependence would deviate from the behavior discussed in Section 5.2 as the PL intensity would be greatly increased at low excitation power. This effect is shown in Fig. 5.11 (blue) alongside a more typical curve (red). As can be seen, at laser power of ~ 0.1 mW, the PL yield is enhanced by more than two orders of magnitude. This is a dramatic difference, and of particular interest in Ge, given its unexceptional light-emitting properties.

The enhancement is strongly nonlinear, starting with a steep increase at what appears to be a threshold laser power value. Rapidly, the disparity reaches its maximum value at ~ 0.1 mW. As the illumination intensity increases further, the two curves begin to converge with each other. In the strong excitation regime, there is virtually no difference between them.

Several important clues have been determined which shed light on the nature of this phenomenon, in addition to the power dependence discussed above. This section will present

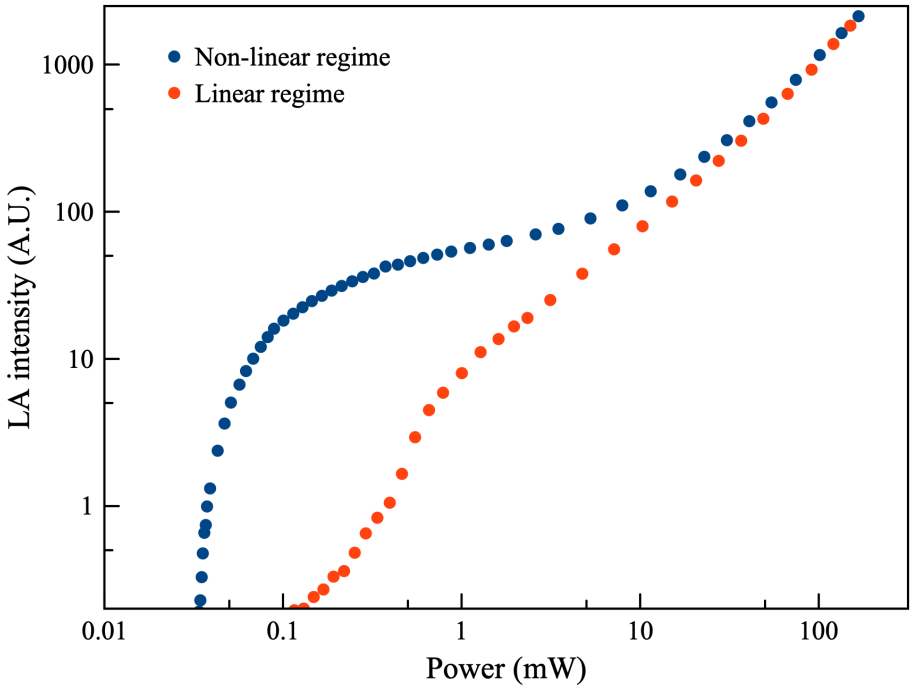

Figure 5.11 Nonlinear PL enhancement at low excitation power (blue) compared to a more typical linear behavior (red).

these clues and offer a tentative explanation for the low power PL enhancement.

1. Indirect PL lineshapes are not affected

It is crucial to note that the PL increase does not seem to have any impact on the lineshapes of the emission. The theoretical model discussed in Chapter 4 remains valid and the extracted fit parameters show no anomalous behavior. This means that the radiative recombination mechanism is unchanged. Furthermore, no new peaks are detected which was verified by performing a broad spectral scan over the range of $1500 - 2000\,\text{nm}$ (corresponding to $0.62 - 0.82\,\text{eV}$). The resulting spectrum is shown in Fig. 5.12, along with a fit confirming the unaffected nature of the emission lineshape.

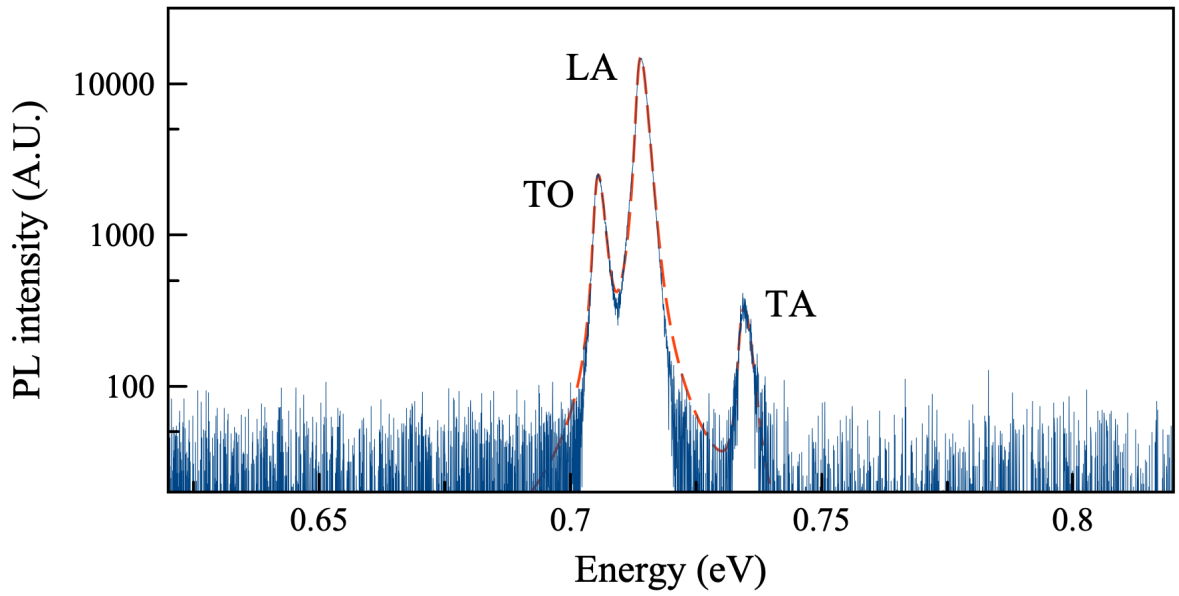

Figure 5.12 Broad spectral scan of Ge PL in the nonlinear regime, showing a good agreement with the indirect PL model and no additional peaks.

2. The behavior is binary

The PL enhancement has been observed multiple times on different Ge samples. However, intermediate behavior was not - the power dependence always exhibits one of two behaviors shown in Fig. 5.11. This indicates that the effect is triggered by a sudden effect, rather than through a gradual process.

3. The enhancement is uniform throughout the sample

The enhanced PL was observed on the samples which would exhibit linear power dependence in other measurement runs. This could lead to a suspicion that the effect is a local one, associated with a high defect density or a different type of a lattice anomaly. However, it was independent of the position on the sample (verified over several mm) and must therefore be a bulk effect.

4. The effect is caused by carrier localization

Fig. 5.13 shows the PL intensity I_{PL} as a function of the Lorentzian broadening Γ_L, extracted from the same data set as the one seen in Fig. 5.11. Since $\Gamma_L \propto n$ and $I_{PL} \propto n^2$, the relationship between the two quantities is expected to be quadratic. Despite a strongly non-linear power dependence, $I_{PL} \propto \Gamma_L^2$ holds to a very good approximation. This is a crucial piece of information as it demonstrates that the increased PL is not due to a change in the radiative efficiency of carriers. Instead, the carrier concentration itself is enhanced in the collection volume.

Since the effect is not related to local defect densities (which could, in principle, lead to an increase in the local carrier concentration), the most likely explanation is a suppressed lateral out-diffusion. As Section 5.1 demonstrated, the vast majority of photocreated carriers in Ge migrate outside of the excitation area and, even if they recombine radiatively, their PL cannot be detected. Limiting the extent of diffusion can explain the carrier localization in a compelling manner.

5. The effect is extremely sensitive to temperature

Fig. 5.14 shows ^{73}Ge spectra acquired at three different laser powers when the PL enhancement was observed (blue). The lowest selected value of P_{laser} corresponded to the maximum disparity seen between the two regimes. Spectra shown in red were acquired in the exact same manner after the temperature of the cryostat platform was increased very slightly by 0.2 K. The temperatures displayed beside the spectra were recorded by a thermometer installed on the sample holder.

This minute increase in the global temperature was sufficient to entirely eliminate the PL enhancement. This strongly indicates that the underlying mechanism is triggered by a phase-

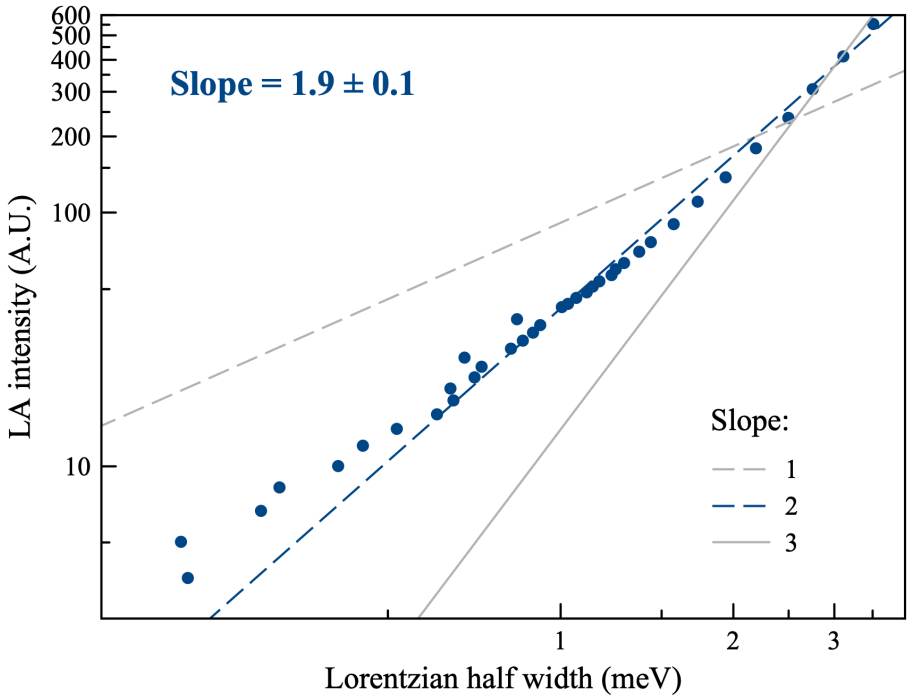

Figure 5.13 Relationship between the PL intensity and the Lorentzian broadening in the nonlinear intensity regime. The quadratic dependence (the slope of 2) holds to a very good approximation.

like transition with a sharp temperature dependence. Also, it explains the non-linear power dependence - at higher excitation densities laser heating becomes sufficient to increase the local temperature and suppress carrier localization, as clearly seen in Fig. 5.14.

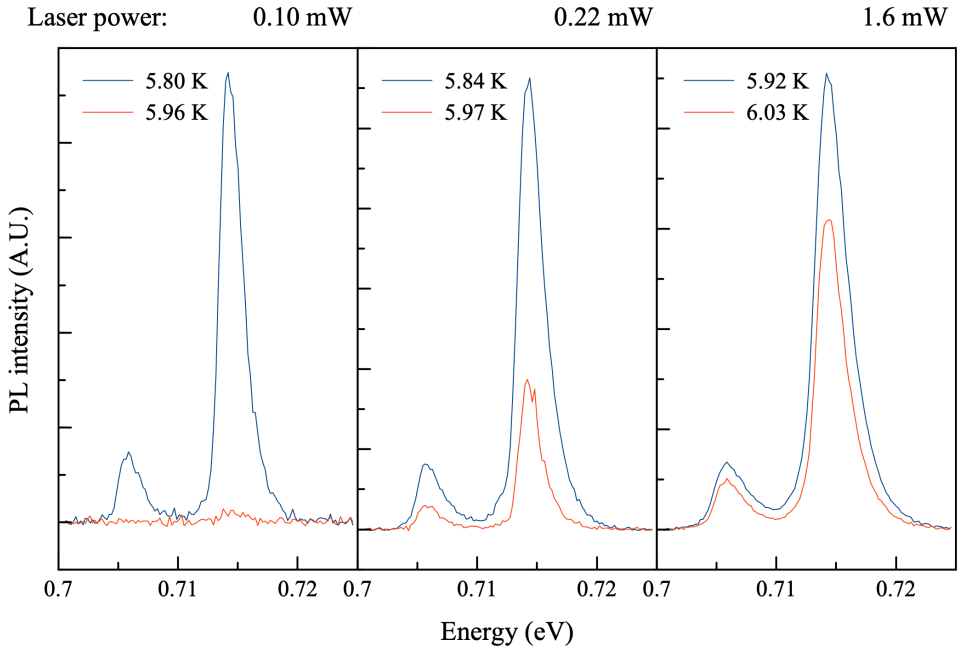

Figure 5.14 ^{73}Ge spectra acquired at three different laser powers and two platform temperatures. Temperature values displayed on the plots were measured with a thermometer attached to the sample holder. Changes in PL intensity induced by a small temperature increase demonstrate a threshold behavior of the PL enhancement.

Interpretation

While this work does not offer a detailed and compelling model explaining PL enhancement, it does propose that it is related to condensed phases of the excitonic gas, which are known to exist in Ge at low temperatures. Condensation of carriers would indeed limit the extent of out-diffusion and exhibit sharp thresholds in both temperature and laser power. However, as explained in the discussion of electron-hole droplets in Section 6.1, such condensed phases typically lead to PL features which are absent in this case. Still, this general interpretation seems plausible given the nature of the evidence gathered and outlined in this section.

5.5 Conclusions

This chapter has explored a number of aspects of Ge photoluminescence. The experimental data was collected under a wide variety of experimental conditions and resolved in several parameters. The model of PL lineshapes from Chapter 4 permitted an advanced multivariate analysis of PL spectra, particularly through the information provided by the Lorentzian broadening of peaks.

Due to this comprehensive nature of the overall investigation, new insights were offered in areas which suffer from inconsistent or incomplete literature. This is particularly pertinent to the analysis of the influence of the laser wavelength and power. Most studies in the literature relied on limited data which offered a constrained perspective. The wealth of spectra collected in this work allowed to rigorously examine various assertions made in earlier studies and propose a compelling explanation based on interactions with defects. Further measurements involving intermediate laser wavelengths would be helpful in validating it.

The diffusion model successfully explained the trends caused by varying the excitation NA to within an order of magnitude. Discrepancies stem from surface effects, which were not considered here. Laser heating was demonstrated using a data set collected with a particularly poor thermal contact. Understanding it was vital in ensuring high data quality for spectra presented throughout this thesis.

PL enhancement due to carrier localization is a particularly interesting phenomenon due to the dramatic increase in the PL yield. While the explanation of it offered here is tentative, the evidence presented in Section 5.4 offers grounds for an informed discussion. It was also useful for other aspects of this thesis, offering a way to increase SNR and providing further evidence for the interpretation of Lorentzian broadening in Section 4.5.

CHAPTER 6 EHL AND BOUND EXCITONS IN ^{76}Ge

So far in this thesis, only one PL mechanism has been discussed, namely phonon-assisted indirect PL from free excitons. However, other radiative recombination channels are expected in Ge, particularly at very low temperatures and at significant defect densities. This chapter will discuss two such mechanisms which were observed in Ge^{76} spectra.

The first of these is luminescence due to electron-hole liquid (EHL). It is commonly referred to as electron-hole droplets (EHD) as it often takes shape of macroscopic spherical clusters within a dilute exciton gas. EHL is a condensed phase of excitons which forms in semiconductors at low temperatures and at high charge carrier densities. It leads to spectrally broad PL features due to the inherent complexity and stochasticity of such a multi-body system.

The other mechanism is bound exciton (BE) PL associated with excitons attached to neutral impurities in Ge. These are localized quantum states with well-defined energies which lead to narrow emission peaks. In this work, their presence was detected in Ge^{76} (and, to a lesser extent, in Ge^{74}), even though samples used in this thesis were not intentionally doped with any impurity atoms.

This chapter will first discuss EHL and BE photoluminescence in Ge based on existing literature. Of particular interest will be the BE emission lines observed in phosphorus-doped Ge, as they bear strong resemblance to data obtained in this work. The chapter will then present Ge^{76} spectra featuring peaks which stem from both aforementioned phenomena. It will be demonstrated that they are consistent with peaks earlier reported in P-doped Ge. The spectra will be complemented by a detailed temperature and power dependence analysis. Finally, isotopic shifts in P-doped Ge will be reported for the first time.

6.1 Electron-hole liquid

To understand the collective behavior of excitons in semiconductors at low temperatures, several interaction mechanisms must be considered. Constituent charges interact through Coulomb forces - attractive for electron-hole pairs and repulsive for like charges. The nature of these interactions varies with intra- and interexciton separation as screening effects evolve

with distance. Another important factor is thermal energy which determines whether excitons can escape from weakly binding potentials. When wavefunction overlap becomes significant, exchange and correlation energies must also be considered. The interplay of these multiple competing mechanisms creates a complex many-body problem to address.

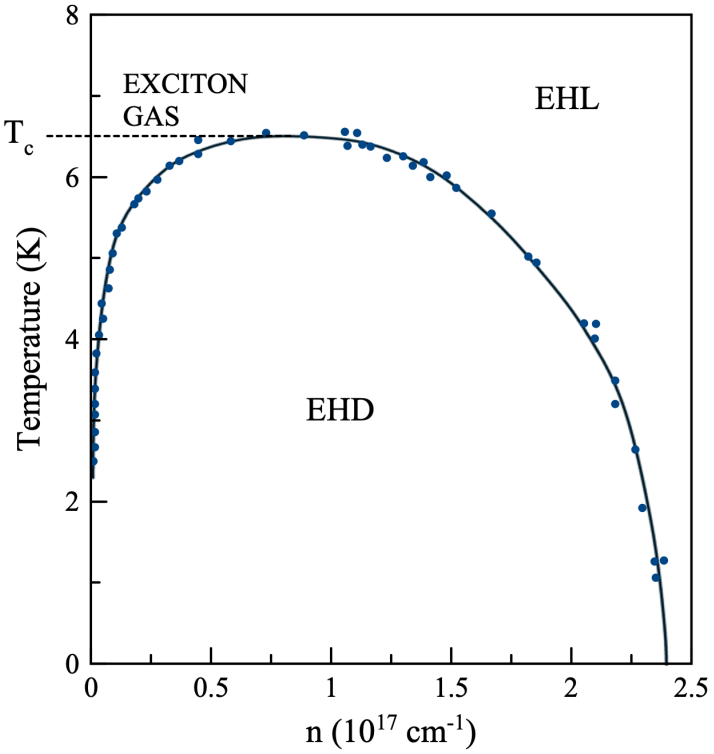

Figure 6.1 Phase diagram showing the behavior of excitons in Ge as a function of temperature and carrier density. Above critical temperature T_c, their appearance ranges gradually from a dilute exciton gas to plasma-like electron-hole liquid (EHL). Below T_c, two distinct phases can coexist in the form of macroscopic electron-hole droplets (EHDs) within exciton gas. Blue dots show experimental data from [71].

Detailed studies have shown that at low temperatures T (when kinetic energies are small) and at high carrier densities n (when multi-body interactions become important) excitons form a condensed phase called electron-hole liquid (EHL) [72–74]. It is a quantum state which arises from a delicate balance between the interactions mentioned above. It can form through a gradual transition from exciton gas to plasma-like EHL, or, below the critical temperature T_c, it can precipitate from exciton gas in the form of macroscopic electron-hole droplets (EHDs). Fig. 6.1 shows a $T - n$ phase diagram of EHL in Ge [71].

EHDs in Ge have been detected through a number of methods including measuring photocurrent noise [75], light scattering [76] and photoluminescence [42, 77]. In PL spectra, EHDs lead to broad peaks which are found at energies below corresponding FE peaks. Fig. 6.2 shows a spectrum of the LA-assisted FE emission line accompanied by the LA-assisted EHD peak [42]. The value of $\phi(0)$ (the binding energy of EHL at 0 K) is indicated on the plot. EHD peaks show strongly non-linear power dependence. Above $T \approx 2$ K, they only appear above a cut-off incident laser power (as per the phase diagram in Fig. 6.1), beyond which their intensity grows rapidly. They also exhibit hysteresis in power, underscoring non-Markovian behavior which stems from an energy barrier impeding the creation and dissociation of EHDs.

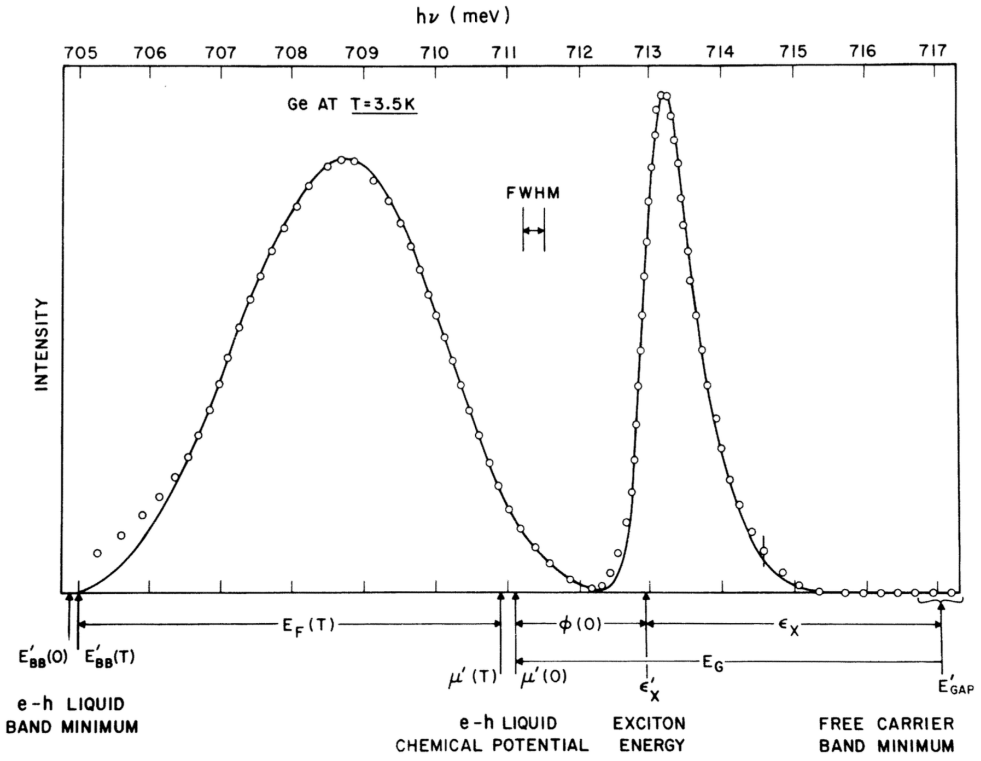

Figure 6.2 PL spectrum of Ge showing LA-assisted transitions of both FE and EHD. EHD peak is broader than the FE line and appears at a lower energy. $\phi(0)$ represents the binding energy of EHL at 0 K. Figure reprinted from Thomas et al. [71]

6.2 Bound excitons in Ge

Defects present in semiconductors disrupt the symmetry of the lattice and create a local distortion in the electrostatic potential experienced by electrons, holes and excitons. In some

cases, a localized bound state may be available in such a local potential, in which case a charge or an excitonic complex can be trapped by a defect. This is of great interest to science and technology as it constitutes a relatively isolated quantum system that can be controlled through optical means.

In Ge, bound exciton (BE) peaks have been observed in samples doped with elements such as P, As, In and Sb [78–80]. They have also been reported in cases where no impurities had been deliberately added during fabrication [81]. As such, their intensity can be used as an indication of the purity of a Ge sample.

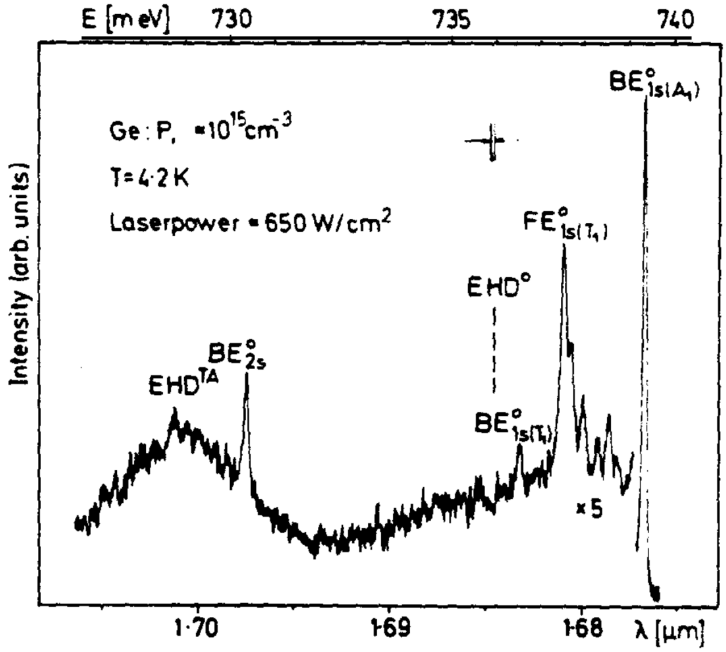

Figure 6.3 PL spectrum of P-doped Ge showing BE emission lines. Reprinted from R. W. Martin [78]

.

Fig. 6.3 shows a PL spectrum of phosphorus-doped Ge [78]. It shows a number of peaks associated with BE emission which share several common characteristics. One is the proximity to the gap energy which makes them very sensitive to temperature – bound excitons escape readily when the thermal energy exceeds a few meV. Furthermore, they all have a relatively small width because their available energy states are discrete and because they are less prone to many broadening mechanisms. Compared to free excitons and charges, they are less exposed to collisional broadening due to screening effects and smaller collision

cross-sections.

Peak labels in Fig. 6.3 describe the electronic transitions from which they originate. BE and FE refer to bound and free exciton transitions, 1s and 2s denote the electronic state of the donor electron while A_1 and T_1 refer to valley-orbit splitting states in the conduction band of Ge. A_1 is the lower symmetric state while T_1 is antisymmetric and higher in energy.

Mayer et al. [79] also reported PL spectra of P-doped Ge. Their measurements agreed with R. W. Martin's but they offered a different interpretation for them. They took advantage of the Kirczenow shell model [82] which treats bound excitons in a manner similar to atoms with multiple electrons in surrounding orbitals. In particular, Mayer et al. disagreed with the attribution of the $\mathrm{FE}^0_{1s(T_1)}$ peak, instead assigning it to one of the excited states of the bound exciton itself.

Implanting Ge with other elements than phosphorus leads to qualitatively similar spectral features at various energies. These will not be explored further as only the results for P-doped Ge are pertinent to spectra presented in this thesis. The remainder of this chapter will be devoted to the discussion of these spectra.

6.3 Experimental results

Fig. 6.4 shows low and high power PL spectra of Ge^{76}. They feature a number of prominent peaks in addition to indirect phonon-assisted PL. At $\sim 0.74\,\mathrm{eV}$, there is a pair of narrow peaks associated with bound exciton recombination. These were typically seen on this sample, although their intensity varied strongly with position and temperature. Furthermore, at high incident laser power, broad features due to EHD appear. It was unusual to see them in the course of the measurements presented in this thesis. Their general absence was most likely caused by the limited ability of the sample cryostat to maintain low temperatures under strong laser illumination, which are the required conditions according to the phase diagram in Fig. 6.1. They will be discussed briefly, followed by a detailed analysis of the BE peaks.

6.3.1 EHD peaks

EHD peaks exhibited a strong power dependence, as shown in Fig. 6.5. They were absent at low incident power but rapidly increased in intensity under excitations above $\sim 1\,\mathrm{mW}$.

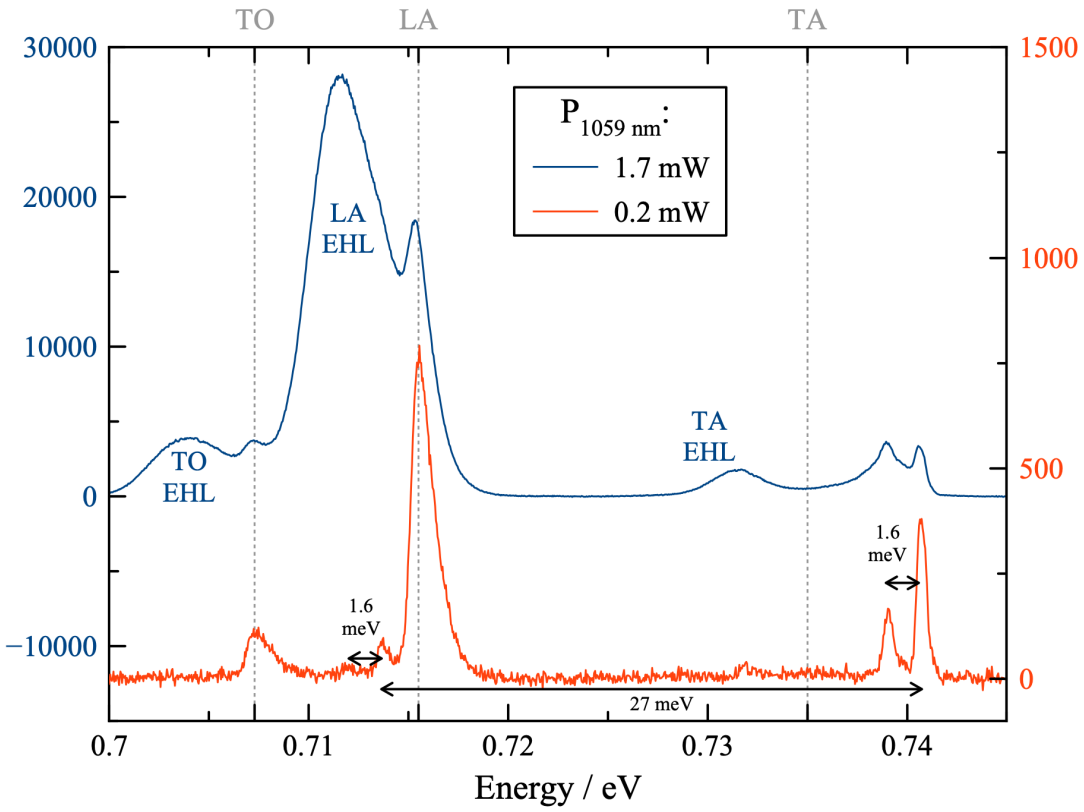

Figure 6.4 Spectra showing phonon-assisted PL from free excitons, electron-hole liquid and bound excitons in ^{76}Ge. FE peak energies are marked with gray dotted lines. BE peaks include a doublet near 0.74 eV separated by 1.6 meV and a number of less intense features. EHD peaks only appear at high laser power (blue spectrum).

Hysteresis and saturation at high power provide further evidence for attributing these spectral features to EHD PL.

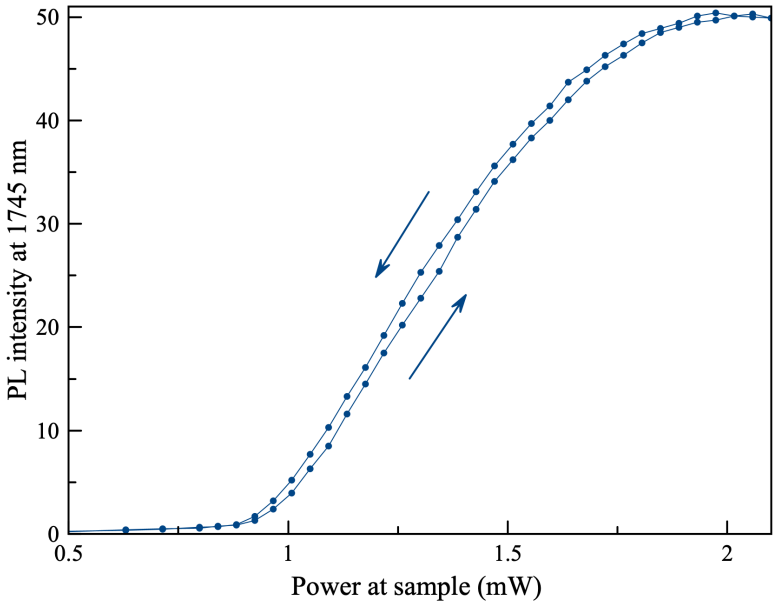

Figure 6.5 Power dependence of LA-assisted EHL peak amplitude showing threshold behavior and hysteresis.

The spectral positions of EHD peaks, as well as their shapes, are sensitive to temperature. Since these features were not the focus of this thesis, detailed fits to extract fundamental parameters (such as the binding energy at 0 K) were not performed. It is only noted that peak positions relative to FE peaks are consistent with literature to within 1 meV.

6.3.2 BE peak positions

Fig. 6.6 compares obtained spectra (shown in full in Fig. 6.4) to traces from [78] (shown earlier in Fig. 6.3). All energies are shifted due to the different isotopic compositions of the studied samples. However, the relative positions of the three most intense peaks do match. The broadening of the middle peak, especially on the high energy side, is also consistent with the presence of less intense peaks which are visible in higher resolution spectra. This provides strong evidence that the Ge^{76} sample discussed here was unintentionally doped with phosphorus.

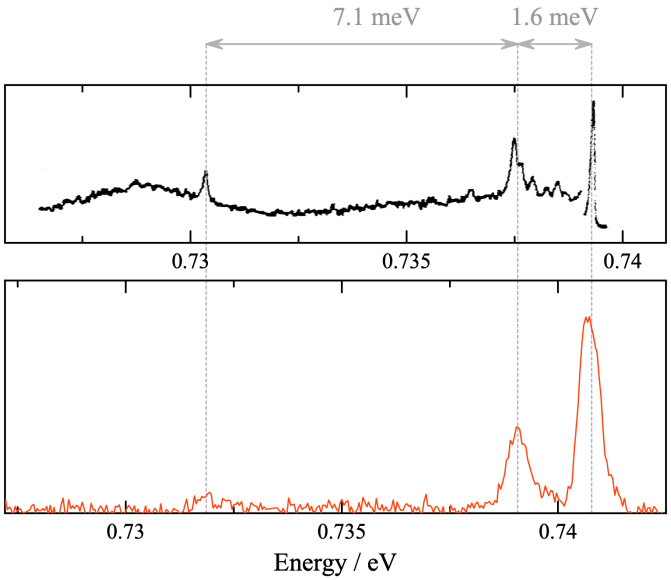

Figure 6.6 Comparison of the Ge^{76} spectrum presented in this thesis (bottom) to the P-doped Ge spectrum from [78] (top). Despite an isotopic energy shift between the two, relative BE peak energies are consistent, hinting at the same origin thereof.

Fig. 6.7 shows the energy separation of the 0.74 eV pair of peaks more accurately as a function of the sample platform temperature. It does not appear to vary with $T_{platform}$ and has a value of 1.640 ± 0.005 meV. As can be seen in Fig. 6.4, these two peaks have a replica near the energy of 0.713 eV. Signal-to-noise ratio for the replica is poor but sufficient to confirm that the peak separation is consistent with the main pair. This means that they are an LA phonon replica of the peaks at 0.74 eV. It is worth noting they are at a lower energy than the LA line of the free exciton band. This confirms that narrow peaks discussed in this chapter cannot originate from FE or indirect gap transition and must arise from BE emission, as has been assumed.

The presence of the LA replica of the pair allows to directly measure the LA phonon energy of 27.0 ± 0.2 meV as well as BE energies (relative to FE band) of 1.4 ± 0.1 meV and 3.0 ± 0.1 meV.

6.3.3 Temperature dependence

PL intensity was recorded as a function of temperature to obtain further information regarding the underlying processes. Fig. 6.8 shows temperature dependence of the pair of BE peaks, referred to as peak 1 and peak 2, as indicated in the inset. They both show steep drop

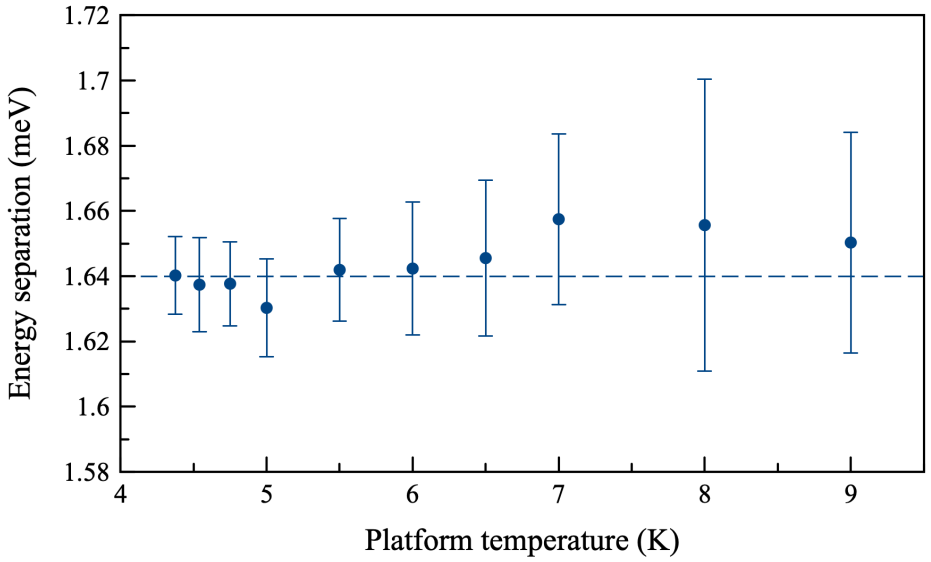

Figure 6.7 Energy separation of two intense BE peaks at 0.74 eV as a function of sample platform temperature. Best fit horizontal line yields a value of 1.640 ± 0.005 meV. No significant temperature dependence is observed.

off with $T_{platform}$ which explains why they are only prominent when sufficiently low sample temperature is obtained. Intensity $I(T)$ was fitted using the Arrhenius equation

$$I(T) = \frac{I_0}{1 + A \exp\left(-\frac{E_a}{k_B T}\right)}, \tag{6.1}$$

where I_0 is PL intensity at 0 K, A is a dimensionless constant and E_a is the activation energy of the quenching process. The extracted values for E_a are 2.92 ± 0.28 and 3.05 ± 0.15 meV for peak 1 and 2 respectively. Fig. 6.9 shows a similar plot for the LA-assisted FE peak which yielded the activation energy E_a of 3.0 ± 0.6 meV. The relatively large uncertainty stems from a slower decrease in PL intensity with temperature.

Notably, all three energies are consistent with one another and with the FE energy in Ge. E_a values for two BE peaks do not correlate with their relative energy positions. This indicates that, at sampled temperatures, quenching process is dominated by the dissociation of free excitons. This process determines the overall abundance of excitons in the material. Obtaining data at even lower temperatures could shed light on other quenching processes which are more pertinent to the nature of BE transitions themselves.

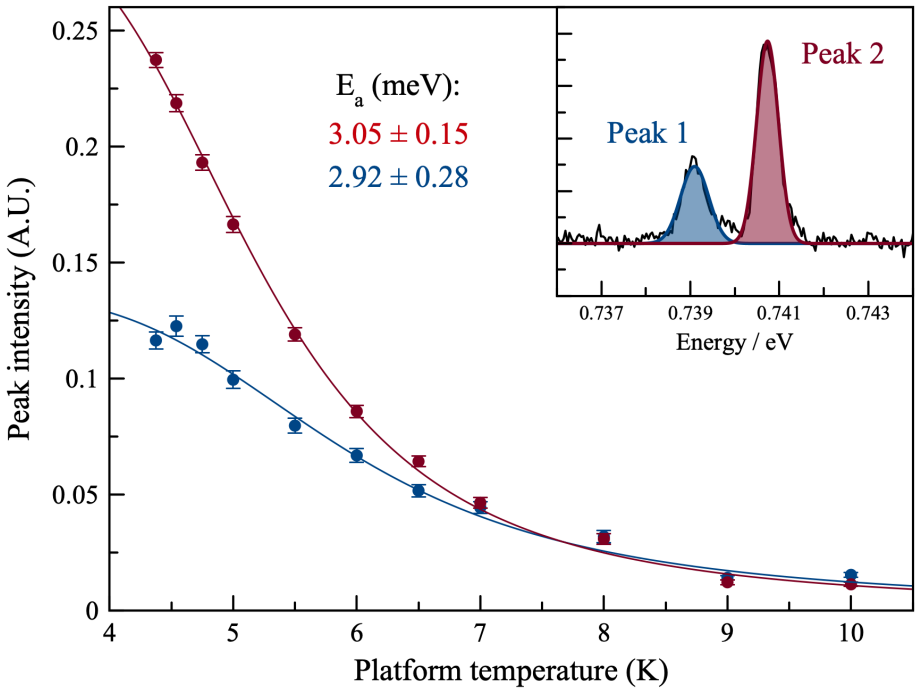

Figure 6.8 Temperature dependence of BE PL intensity. Both peaks show strong variation with T and similar activation energies E_a of $\sim 3\,\text{meV}$.

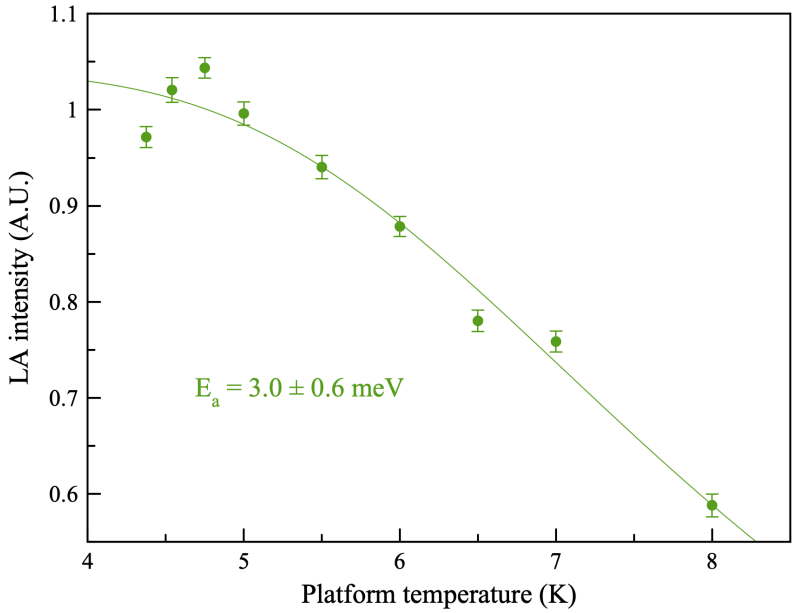

Figure 6.9 Temperature dependence of PL intensity of the LA line of FE. It yields activation energy E_a of $3.0 \pm 0.6\,\text{meV}$, consistent with literature values for FE binding energy.

6.3.4 Power dependence

Power dependence of BE peak intensities is shown in Fig. 6.10 and reveals the same exponent of ~ 1.5 for both peaks. This appears to indicate that the exciton capture process actually involves three charges, rather than just one electron and one hole. It could also mean that there are other non-radiative recombination channels being saturated but the initial slope of ~ 1 for LA-assisted FE peak seems to contradict this interpretation. The exponent of less than 2 also proves that both peaks are associated with a single bound exciton rather than multiexcitonic complexes. Fig. 6.10 also includes power dependence of LA-assisted FE emission for comparison. It shows a departure from typical behavior seen in the absence of BE peaks, when the k-exponent is 1. Exponent of ~ 1.8 indicates that FE-related transitions compete with other recombination mechanisms which saturate with power. The coincidence of strong BE peaks and the increased exponent suggests that BE-related transitions are responsible for this effect.

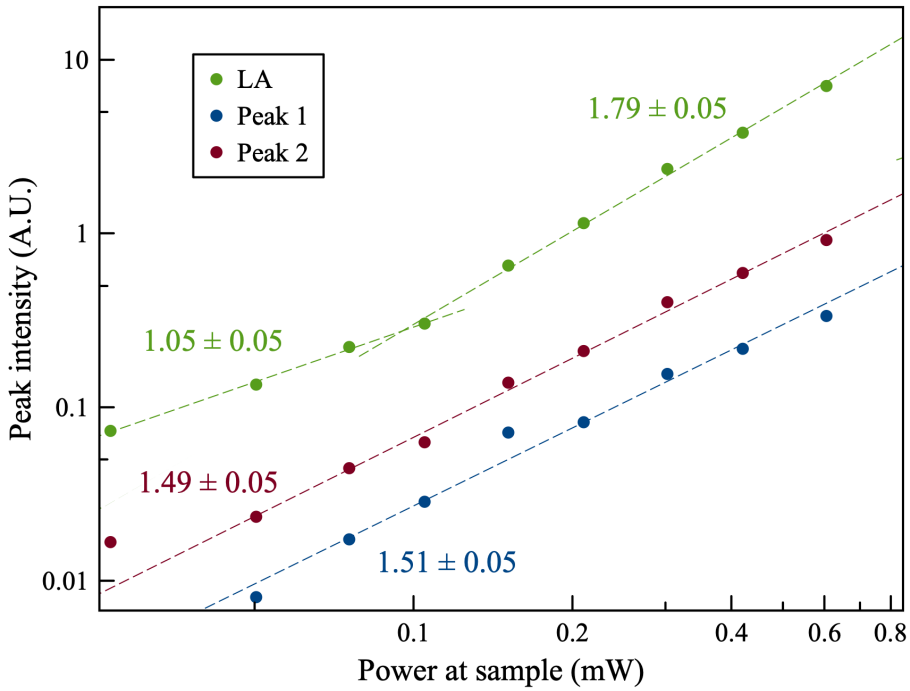

Figure 6.10 Power dependence of bound exciton peaks and LA-assisted free exciton emission showing departure from typical linear behavior. BE peaks exhibit a power exponent of ~ 1.5. The sample was illuminated with a 1059 nm laser.

6.3.5 Two-laser illumination

During the data acquisition, it was observed that the simultaneous illumination of the sample with two lasers did not necessarily increase PL yield, relative to one-laser illumination. Fig. 6.11 shows spectra measured using a constant incident power of the 1059 nm laser (P_{1059}) with differing amounts of 532 nm laser power (P_{532}). While the green laser increases PL yield from FE phonon replicas, it quenches the emission from BE peaks. Furthermore, quenching of the higher energy peak is significantly more pronounced.

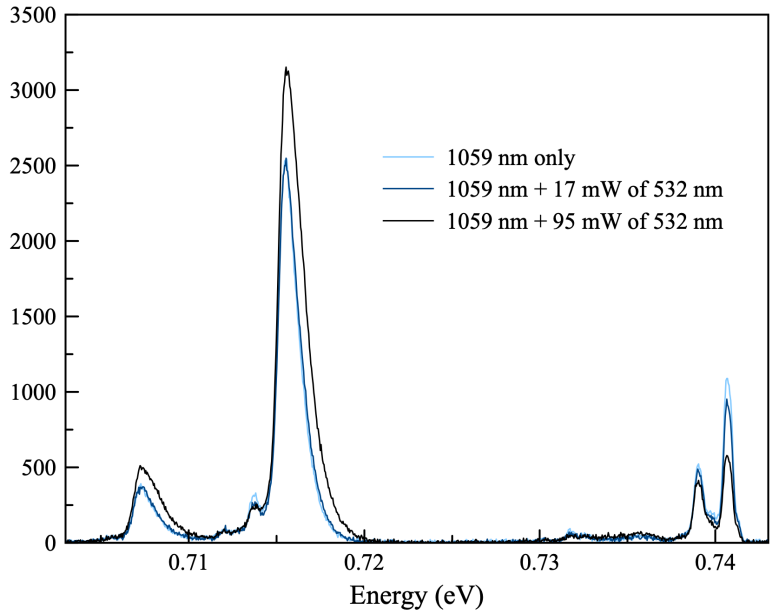

Figure 6.11 Two-laser illumination spectra showing quenching of BE peaks by 532 nm laser while enhancing FE phonon replicas.

Two possible explanations exist for this phenomenon. The first one is simply the laser heating of the sample. It was shown in Section 6.3.3 that the intensity of BE peaks falls steeply with increasing temperature. This would explain why the impact of the second laser is more pronounced for them compared to the FE-related peaks. The second possibility is that P_{532} interacts with defects in a different manner to P_{1059} leading to BE emission quenching through charging the defect population.

In order to verify if laser heating offers a satisfactory explanation, a simple model for the quenching effect was devised:

$$A = a + bP^{3/2} - cAP^{x},$$

where $P = P_{532}$, A is the total BE peak amplitude and a represents a constant contribution to PL_{BE} due to fixed P_{1059}. The term $bP^{3/2}$ represents the contribution due to P_{532}. A power exponent of 3/2 was chosen based on typical bulk PL behavior seen for this laser. $-cAP^{x}$ is the quenching term, proportional to the total amplitude A and P_{532} raised to an exponent x to be determined. The value of x can act as an indicator of the nature of the quenching mechanism. It was demonstrated in Section 5.3 that the temperature rise due to laser heating is directly proportional to laser power. To first order in Eq. 6.1, this would lead to $x = 1$.

Solving for A leads to:

$$A = \frac{a + bP^{3/2}}{1 + cP^{x}}. \tag{6.2}$$

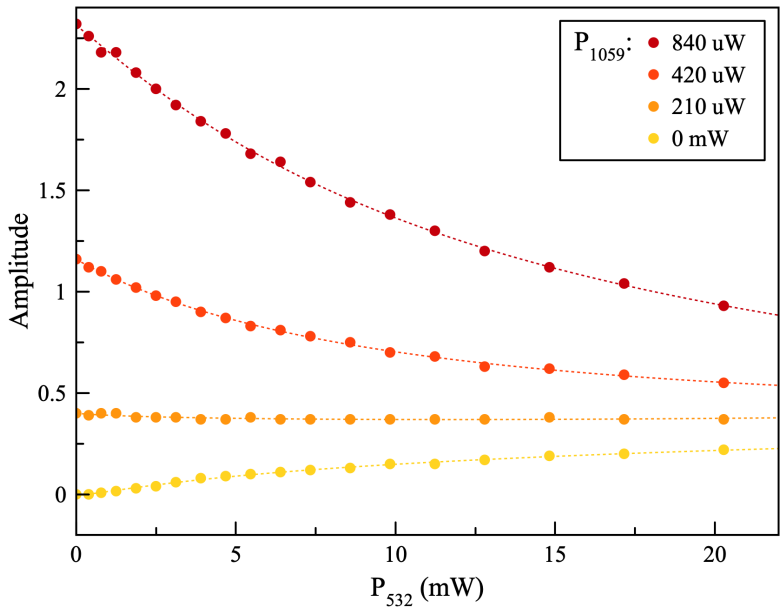

Figure 6.12 Amplitude of the high energy BE peak as a function of P_{532} for different values of P_{1059}. Data was fitted with eq. 6.2 to represent PL quenching.

Fig. 6.12 shows PL quenching as a function of P_{532} for four different values of P_{1059}. Note that only amplitude was recorded, rather than the total intensity, ignoring thermal or power

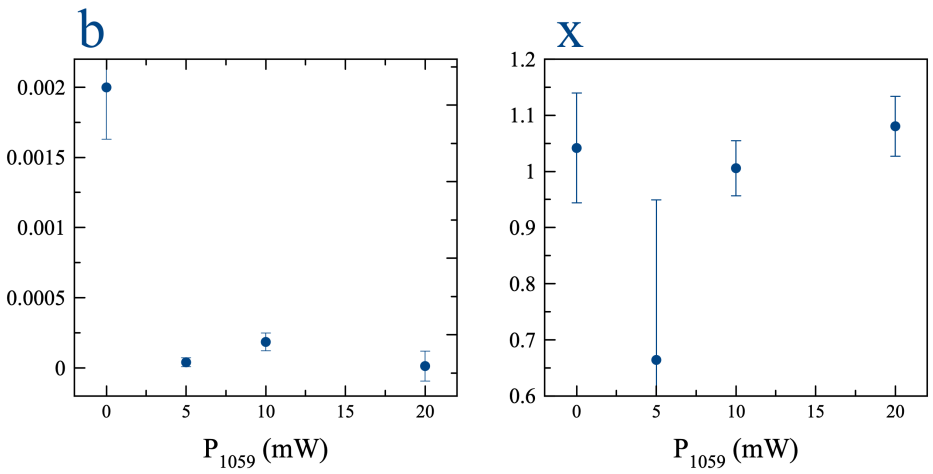

Figure 6.13 Model fit to experimental data showing PL quenching as a function of P_{532} for different values of P_{1059}.

broadening. Overall, the experimental data is in good agreement with eq. 6.2. Fig. 6.13 shows coefficients b and x extracted from the fits. Exponent x shows a consistent value of ~ 1 indicating that quenching is linear in P_{532} (an outlier for $P_{1059} = 5\,\mathrm{mW}$ can be explained by negligible curvature of that data set which led to a very high uncertainty in fit parameters, see Fig. 6.12). The data is therefore consistent with the proposed explanation of laser heating.

Coefficient b varies strongly with P_{1059}, a likely effect of the simplifications inherent to the model. The assumption of k_{532} of 3/2 is based on FE PL and needn't be the case for BE photoluminescence. Furthermore, PL components due to 1059 and 532 nm are added linearly, neglecting any cross-correlation. The fact that b is by far the largest for $P_{1059} = 0$ indicates that 532 nm illumination has a limited effect on the charge carrier population when a more efficient 1059 nm laser is applied simultaneously.

6.3.6 Isotopic shifts

Similar BE peaks were also observed in Ge^{74} samples, although their intensity was far lower than of those seen in Ge^{76}. Fig. 6.14 shows the comparison of the BE peaks from both isotopes. Energy spacing, relative intensities and widths are all consistent within the measurement uncertainties. The value of the isotopic energy shift was found to be $0.94 \pm 0.05\,\mathrm{meV}$. This is of the expected order of magnitude although higher than the value of $0.57 \pm 0.04\,\mathrm{meV}$, reported by Etchegoin et al. [81]. It must be noted that they only observed one BE peak and

did not indicate what was the likely origin of it. Still, BE peaks are expected to scale with the gap energy and thus the disparity between the two values is surprising.

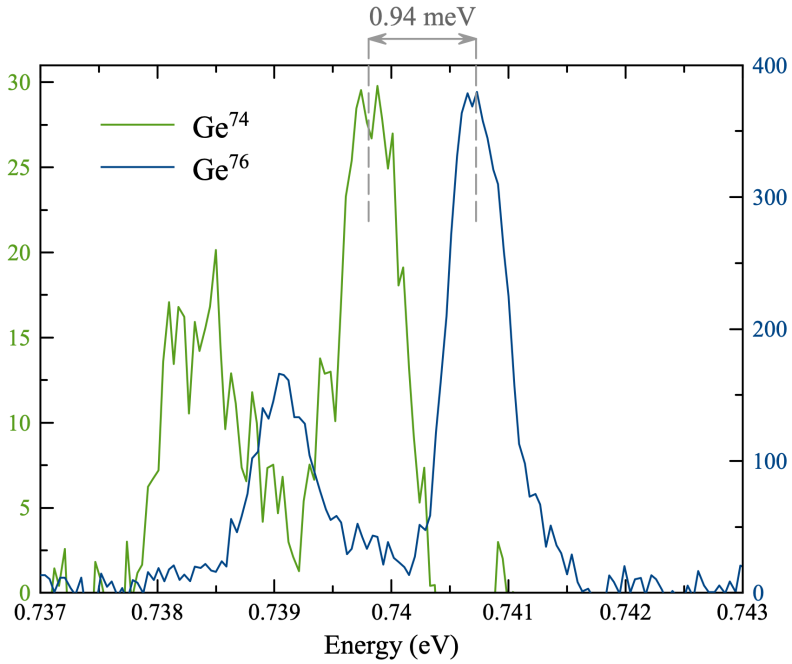

Figure 6.14 Comparison of bound exciton peaks from ^{74}Ge and ^{76}Ge samples showing consistent energy spacing and relative intensities.

6.4 Conclusions

The resemblance of spectra reported here and in [78, 79] leaves little doubt that phosphorus impurities are responsible for BE peaks discussed in this chapter. Perhaps the most intriguing result of the comprehensive study of these peaks is the power exponent of ~ 1.5. It offers a new insight into the mechanism of defect population in Ge, indicating that three charges may be involved in the process.

The isotopic energy shift of phosphorus BE, between Ge^{74} and Ge^{76}, is reported to be 0.94 ± 0.05 meV. This is somewhat inconsistent with the literature value for similar peaks [81]. In addition to the shift, the presence of a BE LA replica allowed to measure the absolute LA phonon energy in Ge^{76} of 27.0 ± 0.2 meV.

CHAPTER 7 ISOTOPICALLY ENRICHED Ge

The interest in isotopically purified materials has been on the rise due to the requirements posed by quantum technology applications. In order to achieve longer coherence times in a physical system, any source of disorder needs to be reduced. Variations in the atomic mass are one such source which underscores the importance of precise understanding of isotopic trends. This is particularly relevant for important semiconductors such as germanium.

Natural germanium contains a number of stable isotopes with atomic masses ranging from 70 to 76, with a mean isotopic mass of 72.63 [83]. They are listed in Table 7.1 along with their natural abundances. This spread and the availability of high quality samples makes Ge a perfect platform to study the effect of isotopic disorder (and lack thereof) on material properties. Thermal conductivity [84], IR absorption [85], Raman scattering [86], indirect PL [81] and other properties have been investigated using isotopically enriched Ge.

Table 7.1 Stable isotopes of germanium and their natural abundances

Isotope	**Natural Abundance (%)**
^{70}Ge	20.38
^{72}Ge	27.31
^{73}Ge	7.76
^{74}Ge	36.72
^{76}Ge	7.83

In indirect photoluminescence, the effect of the isotopic composition can be seen in several ways. The most prominent of those is the shifting of the peaks in energy, due to the changes in the electronic (excitonic) bands as well as phonon energies. Broadening can be affected too if isotopic disorder introduces additional uncertainty in exciton and phonon energies. Relative intensities of peaks associated with different phonon modes may vary as they are determined by phonon distortion potentials. These quantify band energy shifts under strain and are thus inherently linked to the vibrational properties of the lattice.

This chapter will present a detailed analysis of indirect PL spectra acquired from high-purity ^{72}Ge, ^{73}Ge, ^{74}Ge and ^{76}Ge. Work presented in the preceding chapters directly enhanced the

quality of this analysis. Mastering the stability and efficiency of the experimental set-up (Chapter 2) led to acquisitions with very low signal-to-noise ratio. Understanding the role of excitation conditions (Chapter 5) allowed the selection of optimal experimental parameters to increase PL yield and minimize broadening. The in-depth model of indirect PL in Ge (Chapter 4) permitted the comprehensive examination of acquired spectra and subtle variations they comprised.

Firstly in this chapter, the isotopic energy shifts will be discussed based on existing theory. Afterwards, PL spectra of isotopically enriched Ge will be presented. The analysis of the observed energy shifts will follow, during which absolute values for phonon and indirect gap energies will be reported. Finally, other isotopic effects will be discussed, including changes in the relative intensities of phonon-assisted peaks and additional broadening due to isotopic disorder.

7.1 Theory of isotopic energy shifts

Let us consider the isotopic energy shifts in more detail. The most conceptually straightforward way in which they occur is through changes in vibrational amplitudes due to the changing atomic mass, which effectively modulates the lattice spacing that electrons experience. The impact of this effect on the electronic band structure can be evaluated by making a comparison to thermal expansion of the lattice. At low temperatures, these shifts are of the order of tens of μeV [87], which is much smaller than experimentally observed shifts. This contribution will therefore be neglected in the remainder of this chapter.

The dominant cause of the isotopic energy shifts in semiconductors is the electron–phonon (e-p) interaction [88]. Lattice vibrations distort the potential felt by electrons which leads to both shifting and broadening of electronic bands. In order to quantify this effect, two interaction mechanisms must be evaluated from the e-p Hamiltonian:

$$H_{e-p} = \sum_{k,q} V(q) c^{\dagger}_{k+q} c_k e^{iq \cdot u(R)}, \tag{7.1}$$

where $V(q)$ is the electron-phonon coupling matrix element, $c^{\dagger}_{k+q}$ and c_k are electron creation and annihilation operators, and $u(R)$ is the atomic displacement at position R. Firstly, there is a Debye-Waller term which describes the electron-two-phonon interaction. Secondly, an electron can emit and reabsorb a phonon, a process described by the self-energy term. Both

mechanisms are represented in Fig. 7.1 by their Feynman diagrams.

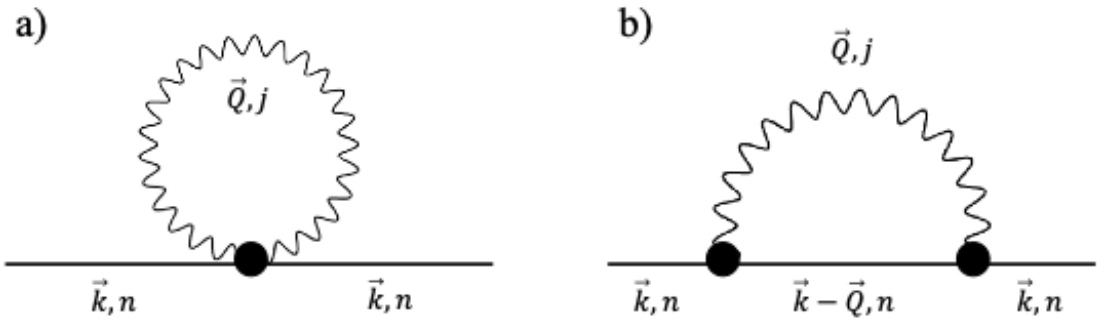

Figure 7.1 Feynman diagram representations for a) Debye-Waller electron-two-phonon interaction and b) self-energy interaction.

Mathematically, the Debye-Waller term stems from the second-order e-p interaction Hamiltonian. In order to avoid a tedious first-principle calculation, Empirical Pseudopotential Method (EPM) can been used [88, 89]. It begins with the electron's Hamiltonian:

$$\widehat{H} = -\frac{\hbar^2}{2m}\nabla^2 + \sum_G V(G)e^{iG\cdot r},$$

where G is a reciprocal lattice vector. Subsequently, the pseudopotential for factors $V(G)$ are multiplied by a Debye-Waller factor $\exp(-\frac{1}{6}G^2\langle u^2\rangle) \sim 1 - \frac{1}{6}G^2\langle u^2\rangle$ evaluated from Eq. 7.1:

$$V(G) \;\rightarrow\; V(G)\left(1 - \frac{1}{6}G^2\langle u^2\rangle\right).$$

This leads to a corrected Hamiltonian $\widehat{H} + \Delta\widehat{H}$:

$$\widehat{H} + \Delta\widehat{H} = -\frac{\hbar^2}{2m}\nabla^2 + \sum_G V(G)\left(1 - \frac{1}{6}G^2\langle u^2\rangle\right)e^{iG\cdot r}.$$

The energy shift can then be calculated from $\Delta\widehat{H}$:

$$\Delta E_{DW} = \langle\psi|\Delta\widehat{H}|\psi\rangle$$

$$= -\frac{1}{6}\langle u^2\rangle \sum_G G^2 V(G)\langle\psi_0|e^{iG\cdot r}|\psi_0\rangle$$

The key result is that the energy shift is proportional to the mean squared phonon amplitude $\langle u^2\rangle$.

The self-energy contribution is calculated by applying second-order perturbation theory to the first order e-p Hamiltonian. Its numerical evaluation is more mathematically complex [88,90] but, for the purposes of this thesis, it suffices to know that ΔE_{SE} is also proportional to $\langle u^2\rangle$. Therefore, if the small effect of the lattice expansion is neglected, the isotopic energy shifts of electronic bands are proportional to the mean squared phonon amplitude.

In the quantum mechanical description of crystal lattices, atomic displacements are expressed in terms of phonon creation and annihilation operators. The displacement field at a specific wave vector Q_j is:

$$|u(Q_j)| = \sqrt{\frac{\hbar}{2M_v N\omega_{Q_j}}}(a_{Q_j} + a^{\dagger}_{Q_j}),$$

where M_v is the average atomic mass, N is the number of atoms per unit cell, ω_{Q_j} is the phonon frequency, and a_{Q_j}, $a^{\dagger}_{Q_j}$ are phonon annihilation and creation operators. Thermal averaging over the Bose-Einstein distribution yields:

$$|\langle u(Q_j)\rangle|^2 = \frac{\hbar}{2M_v N\omega_{Q_j}}[1 + 2n_{Q_j}(T)],$$

where $n_{Q_j}(T)$ is the Bose-Einstein distribution function. At low temperatures $n_{Q_j}(T) \ll 1$, leading to:

$$\Delta E \propto \langle u^2\rangle \propto \frac{\hbar}{2M_v N\omega_{Q_j}}.$$

And, since $\omega_{Q_j} \propto M_v^{-1/2}$, electronic energy shifts due to variations in isotopic mass obey:

$$\Delta E_{electronic} \propto M_v^{-1/2}.$$

Peaks associated with phonon-assisted emissions are also affected by changes in the energy of the phonon itself. Assuming perfect harmonicity, phonon energies $\hbar\omega_{Q_j}$ are:

$$\hbar\omega_{Q_j} = \sqrt{\frac{k_{Q_j}}{M_v}},$$

where k_{Q_j} is the force constant (which is implicitly assumed to show no mass dependence). This means that the total energy shift ΔE, comprising both electronic and phonon energies shifts, is proportional to the inverse square root of the isotopic mass:

$$\Delta E \propto M_v^{-1/2}. \tag{7.2}$$

Etchegoin et al. [81] were first to report isotopic energy shifts in Ge PL. They used first-order Taylor expansion of Eq. 7.2 to model their data. The same approximation was used by Davies et al. [91] to analyze the isotopic shifts of bound exciton (BE) PL peaks. The resulting linear dependence of ΔE on M_v is a good approximation due to the small spread of isotopic mass relative to the mean value $\overline{M_v}$. The comparison between the full expression and the linear approximation is shown in Fig. 7.2, using data for bound exciton peaks from [81].

7.2 Spectra of isotopically enriched Ge

Detailed indirect PL spectra of high-purity ^{72}Ge, ^{73}Ge, ^{74}Ge and ^{76}Ge have been acquired in the course of this thesis. Fig. 7.3 shows spectra measured at very low excitation power, so that collisional broadening and laser heating would be minimal. The data is presented on both linear (a) and logarithmic (b) scales. It includes contributions of TO, LO and LA to the phonon-assisted indirect PL and showcases significant isotopic shifts in energy. The LO-assisted peaks become visible due to low broadening, particularly in the ^{72}Ge spectrum. However, background noise fluctuations over the course of these long acquisitions make quantitative analysis of the LO peak challenging.

The detailed analysis of isotopic effects in this chapter will instead be performed with spectra acquired using slightly larger incident laser power. They are shown in Fig. 7.4 and include the TA-assisted peak as well. The overlap between LA and LO peaks is more significant due to increased broadening but higher signal-to-noise ratio makes these spectra less sensitive to

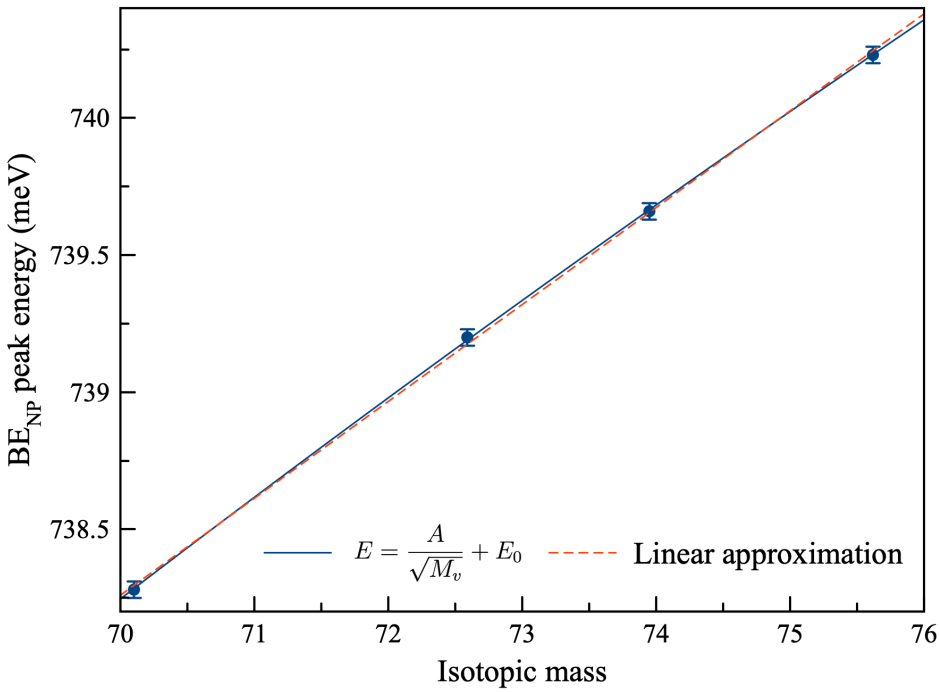

Figure 7.2 Comparison of a fit using Eq. 7.2 fit (solid blue) and a straight line (dashed red) showing close agreement in the atomic mass range of Ge isotopes. BE peak energy position values are from [81].

background fluctuations. The presence of additional peaks near the TA peak in ^{76}Ge must be noted. These are associated with bound exciton emission (see Chapter 6 for details) and indicate a higher defect density in the ^{76}Ge sample, compared to other samples.

The lineshape theory of indirect PL in Ge presented in Chapter 4 was used to model spectra from Fig. 7.4. Detailed fits for each isotope are shown in Fig. 7.5. They show good agreement with the experimental data, with some divergence seen in the tails due to band non-parabolicity. The BE peaks in ^{76}Ge were fitted with a Voigt function in order to isolate the contribution of the TA peak. This is shown in more detail in Fig. 7.6. The spectra are very similar to natural Ge PL shown earlier in Fig. 4.15 with the isotopic energy shifts being the main differentiator.

The excellent quality of the experimental data and the comprehensive fitting model allowed the extraction of PL parameters, such as transition energies and integrated peak intensities, with significantly lower measurement uncertainties than those reported in existing literature. The upcoming sections will present a detailed analysis of energy shifts, relative peak amplitudes and broadening. As the results are progressively introduced, they will be compared to earlier studies, particularly [81].

It must be remarked that the subsequent analysis neglects any temperature effects. While all spectra were obtained in the same cooldown of the cryostat, the quality of the thermal contact between samples and the sample holder can vary. According to spectral fits, the spread in electronic temperatures recorded in the four samples was within 0.5 K. The sample thermometer indicated the average bulk temperature of 5.9 K.

7.3 Isotopic energy shifts

Fig. 7.7 shows the fitted LA peak energy positions as a function of the isotopic mass. In accordance with the results from Section 7.1, they have been fitted using:

$$E = \frac{A}{\sqrt{M_v}} + E_0 \tag{7.3}$$

where A is a constant encompassing the contributions of Debye-Waller, self-energy and phonon energy terms and E_0 is LA-assisted transition energy at $M_v \to \infty$. The agree-

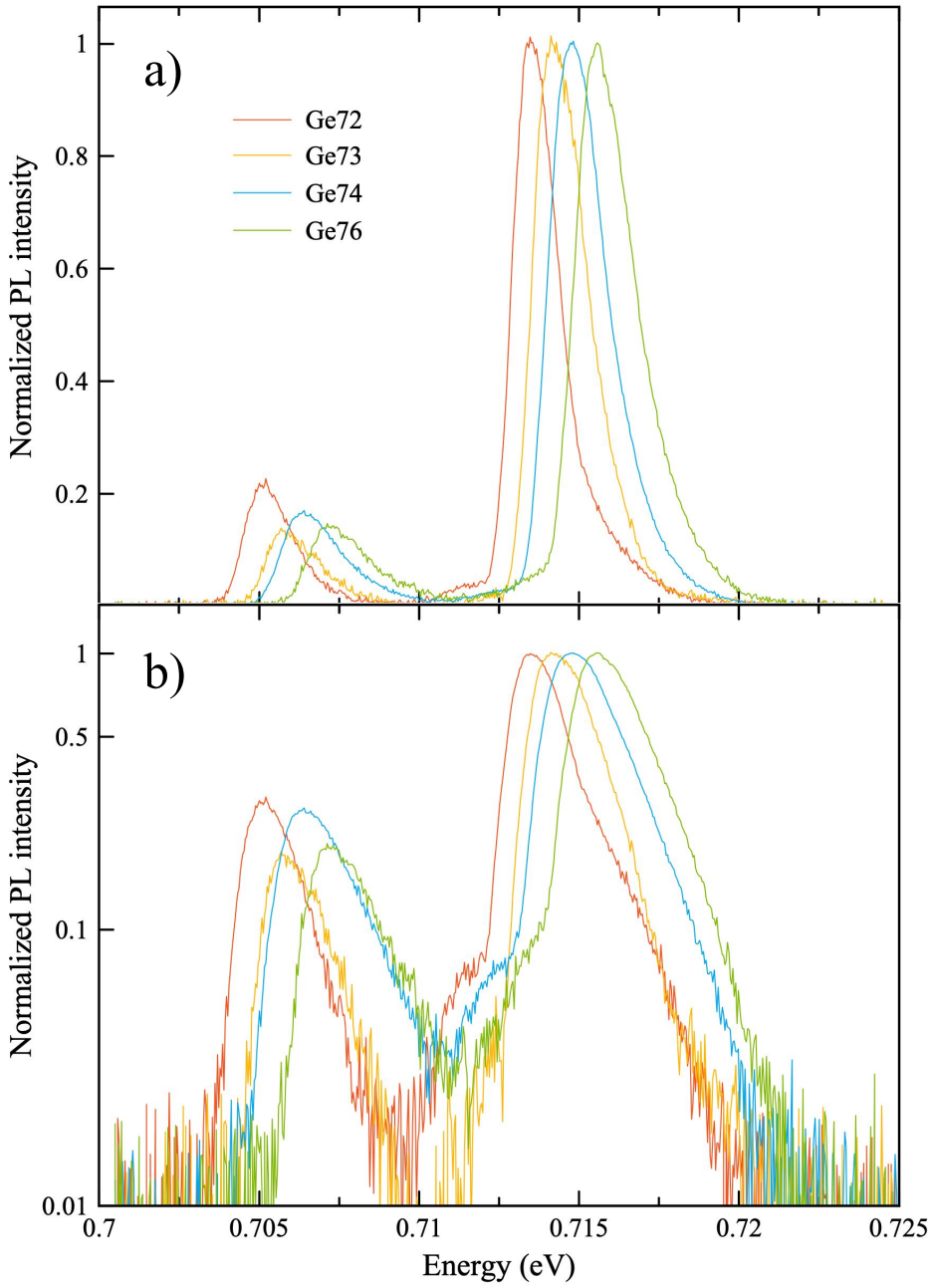

Figure 7.3 Low excitation power PL spectra of isotopically enriched Ge, plotted using a) linear and b) logarithmic scales. TO-, LO- and LA-assisted PL peaks are seen.

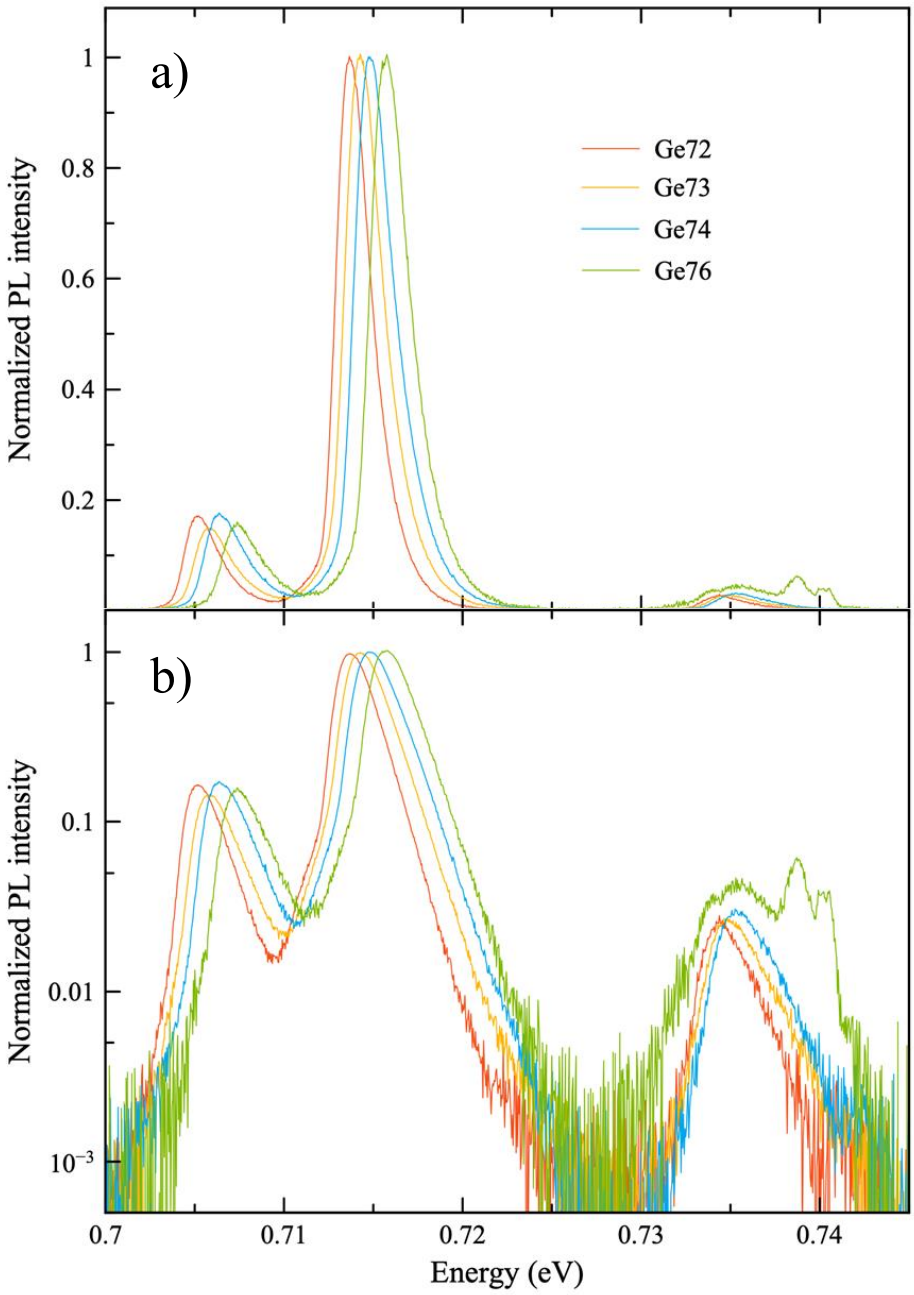

Figure 7.4 PL spectra of isotopically enriched Ge, plotted using a) linear and b) logarithmic scales. TO-, LO-, LA- and TA-assisted PL peaks are seen. Additional peaks seen in ^{76}Ge are due to bound exciton (BE) transitions.

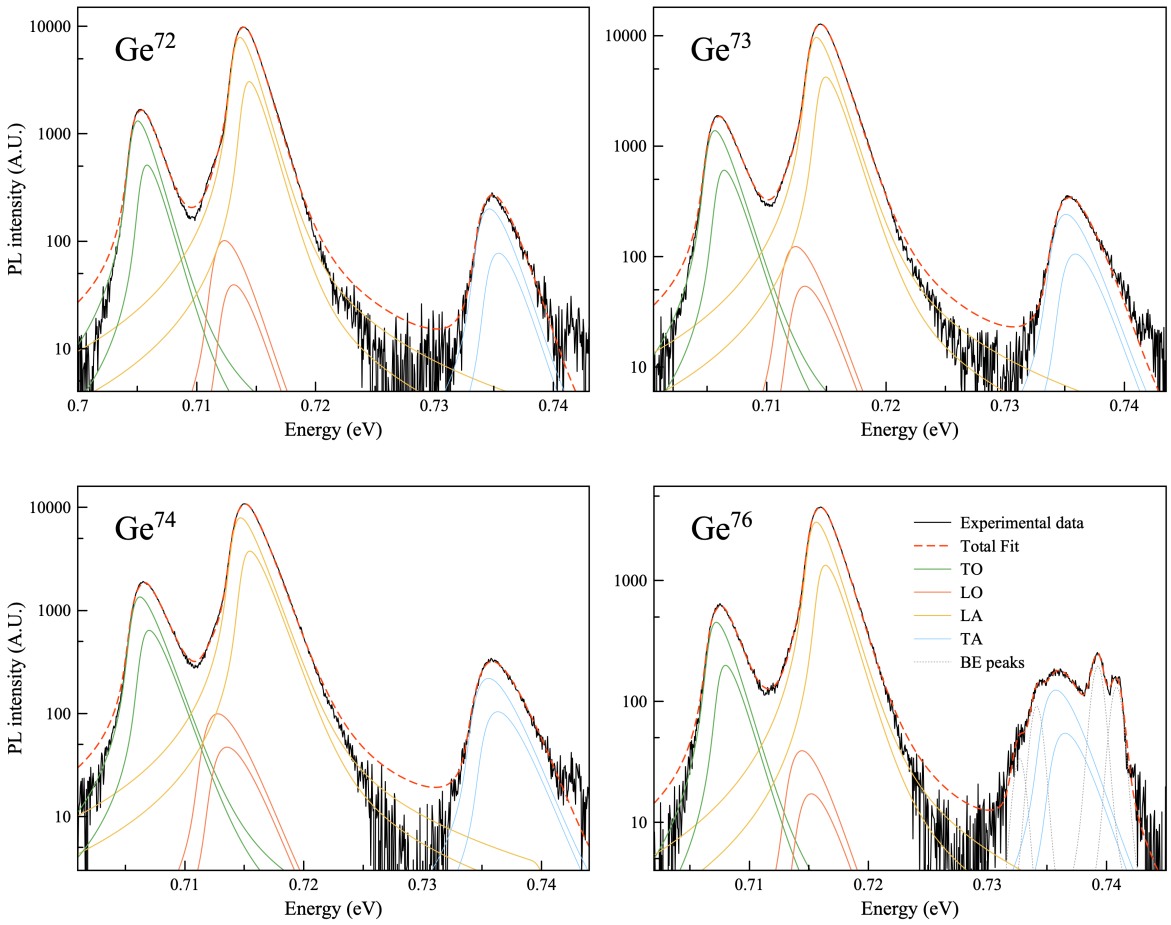

Figure 7.5 PL spectra of isotopically enriched Ge samples of ^{72}Ge, ^{73}Ge, ^{74}Ge and ^{76}Ge. The fits were performed in accordance with the model presented in Chapter 4. LO-to-LA intensity ratio was fixed at 0.017. BE peaks seen for ^{76}Ge were fitted using Voigt functions.

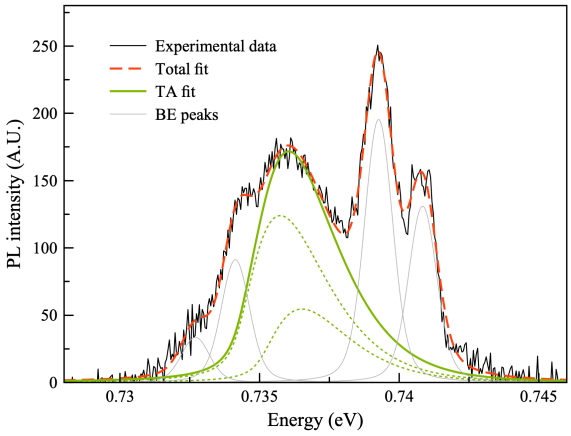

Figure 7.6 TA-assisted PL from ^{76}Ge. BE peaks fits are Voigt functions of equal width.

ment with Eq. 7.3 is excellent. The fit parameters of $A = -0.60 \pm 0.02\,\text{eV} \cdot (\text{a.m.u.})^{1/2}$ and $E_0 = 0.784 \pm 0.002\,\text{eV}$ exhibit low relative uncertainties of 3% and 0.3% respectively. Their physical meaning will be discussed in more detail later, following the evaluation and subtraction of phonon energies.

The value measured in natural Ge is shown on the plot (red data point) but was not used in the fit. Its purpose is to demonstrate that ^{nat}Ge peak positions are consistent with the trends discussed here, when they are plotted using the average atomic mass. This particular ^{nat}Ge was acquired several months before the isotopically enriched spectra and the relatively large uncertainty reflects experimental factors such as the difference in temperature or alignment between the two data sets, rather than the quality of an individual spectrum. It demonstrates the importance of exactly replicating experimental conditions when such subtle differences between samples are compared. This was ensured for the four isotopically purified samples which were measured in the same cryostat cooldown.

Fig. 7.8 compares the shifts reported here with those obtained by Etchegoin et al. [81]. Note that their samples were of lesser isotopic purity, as reflected in fractional M_v values. The agreement is reasonable, except for the $M_v = 70.1$ which appears to be an outlier. Red trend lines show the fit using all 4 values (dashed) or the three highest values (solid), only the latter fit being consistent with this work and with theory. In the original publication, the 4-point fit was proposed but the divergence from the theoretical trend for ^{70}Ge is not addressed.

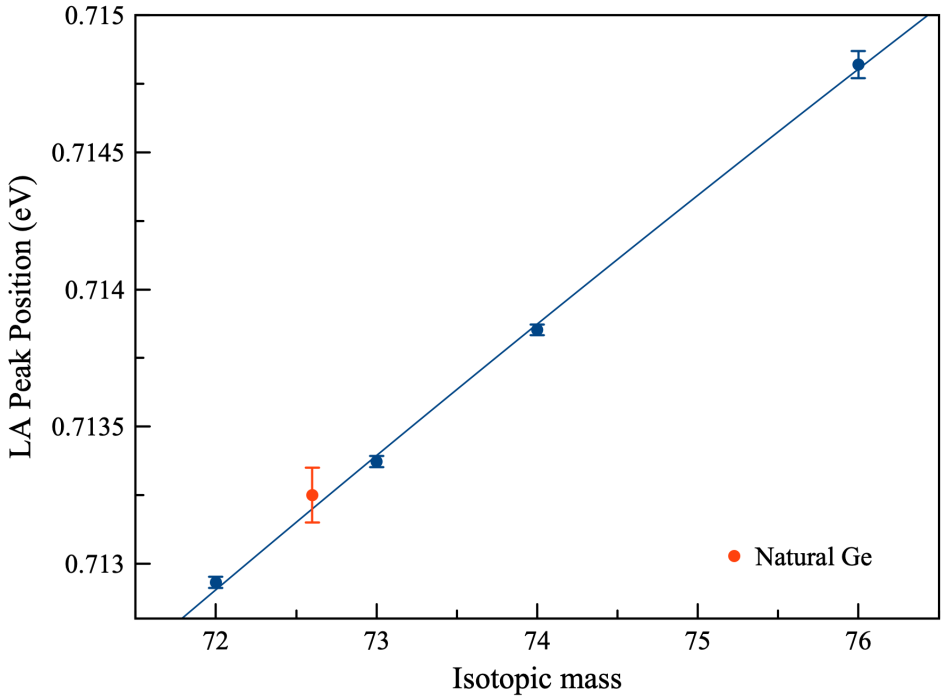

Figure 7.7 LA peak position as a function of the isotopic mass. The shift is well modeled by Eq. 7.3. The ^{nat}Ge value is shown (in red) but was excluded from the fit.

Peaks associated with different phonons do not shift at the same rate. Fig. 7.9 shows the evolution of the energy separation between LA and TO peaks. They shift closer to each other with the increasing isotopic mass. Crucially, subtracting the two peak energies from one another allows to isolate the phonon energy shifts: the electronic band shifts are expected to be equal for both transitions and thus their effect is removed. Within the harmonic approximation, the data can be modeled as follows:

$$\Delta E_{TO-LA} = E_{gap}(M_v) - \hbar\omega_{LA} - (E_{gap}(M_v) - \hbar\omega_{TO})$$

$$= \frac{\hbar(\sqrt{k_{TO}} - \sqrt{k_{LA}})}{\sqrt{M_v}}. \tag{7.4}$$

The fit performed in Fig. 7.9 returned a good agreement with Eq. 7.4 and yielded:

$$\hbar(\sqrt{k_{TO}} - \sqrt{k_{LA}}) = 73.0 \pm 0.3\,\text{eV}\,(\text{a.m.u.})^{1/2}. \tag{7.5}$$

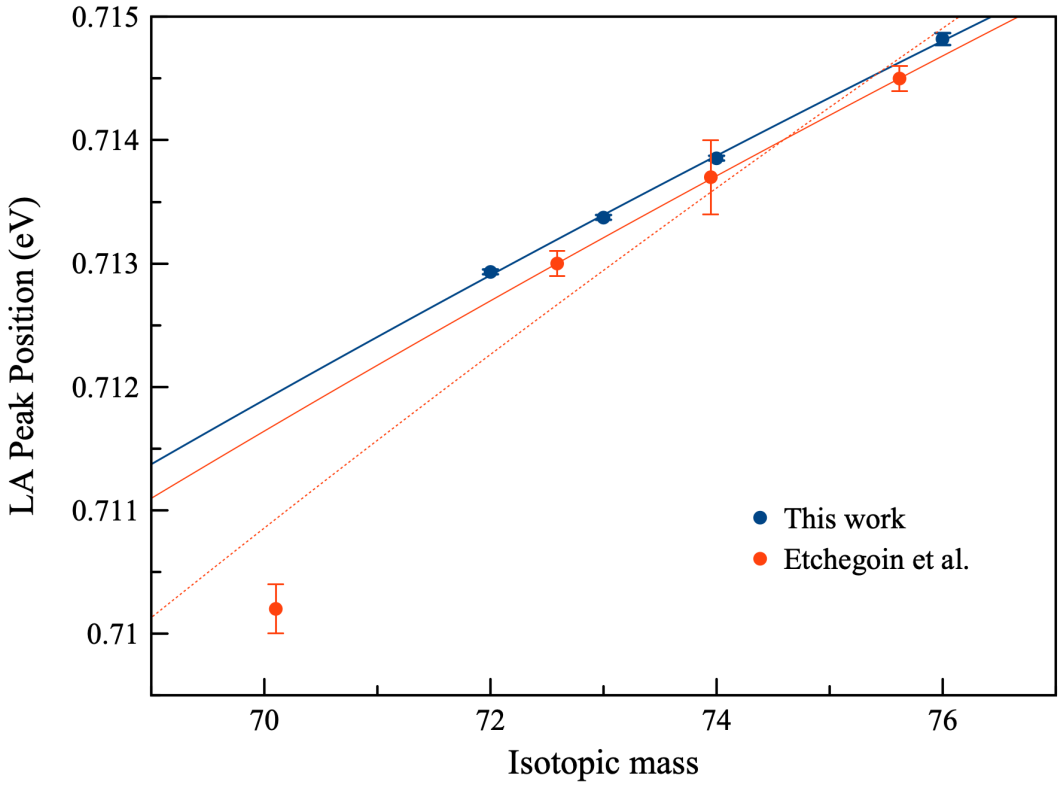

Figure 7.8 Comparison of LA peak position reported in this thesis (blue) with data from [81] (red). Dashed red line is the fit of Eq. 7.3 using all four data points.

LA-TA energy separation was analyzed in an equivalent fashion. The peak separations and the fit shown in Fig. 7.10 led to:

$$\hbar(\sqrt{k_{LA}} - \sqrt{k_{TA}}) = 171 \pm 1\,\text{eV}\,(\text{a.m.u.})^{1/2}. \tag{7.6}$$

In order to obtain absolute phonon energies from these differential measurements, at least one absolute value must be known. Handily, bound exciton PL discussed in Chapter 6 included the main BE peak and its LA phonon replica. From their energy separation, ^{76}Ge LA phonon energy of 27.0 ± 0.2 meV was obtained. Combining these results, absolute TO, LA and TA phonon energies can be calculated for all isotopes. They are summarized in Table 7.2. Note that the above fits and this calculation assumes perfect harmonicity as well as that force constants k are independent of M_v.

LO peak intensities were too feeble to observe a reliable isotopic trend in their energy po-

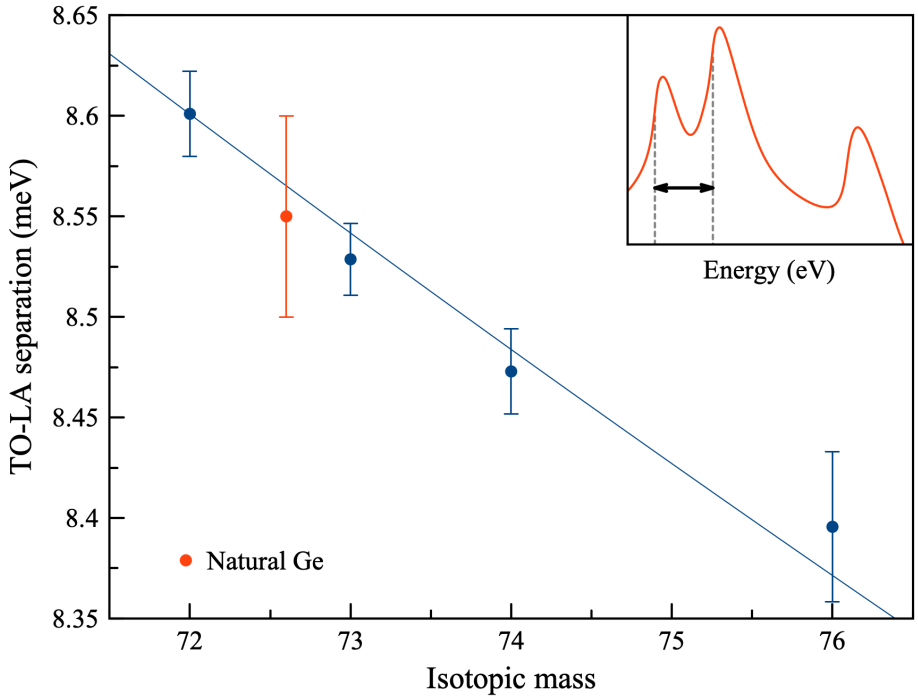

Figure 7.9 Energy separation between TO and LA peaks vs. isotopic mass. The inset schematically shows the plotted energy on a typical Ge PL spectrum. The ^{nat}Ge value is shown (in red) but was excluded from the fit.

sitions, particularly considering their overlap with the nearby LA peaks. Therefore, Eq. 7.4 could not be applied to them in a similar manner to TO and TA peaks. Instead, LO phonon energies reported in Table 7.2 were calculated assuming inverse square root dependence on atomic mass as well as the value of $\Delta E_{LO-LA} = 2.4 \pm 0.3$ meV for natural Ge, reported earlier in Table 4.2. This explains slightly higher uncertainties than those calculated for the other three phonon modes.

Fig. 7.11 compares the phonon energies from Table 7.2 (blue) to the values from [81] (red). The data reported in this work is more complete, both in terms of isotopes, as well as phonon modes included. It also features lower experimental uncertainties. Blue and red data points show similar trends and are roughly consistent within the experimental errors, although there is a systematic shift in energy between them. This cannot be explained by the temperature difference as phonon energies decrease with increasing T [92]. Most likely, the discrepancy occurs from the difference in the calculation methods or lineshape fitting schemes (Etchegoin et al. appear to have disregarded the split ground state of the exciton as well as the collisional

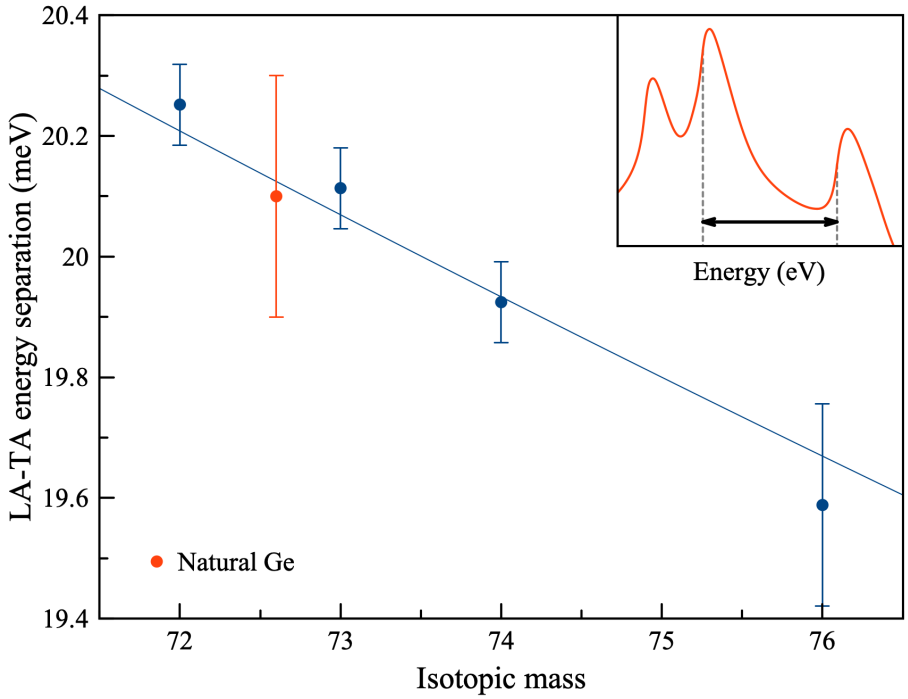

Figure 7.10 Energy separation between LA and TA peaks vs. isotopic mass. The inset schematically shows the plotted energy on a typical Ge PL spectrum. The ^{nat}Ge value is shown (in red) but was excluded from the fit.

broadening).

Equipped with the knowledge of the absolute values of the LA phonon energies, data shown in Fig. 7.7 can be used to calculate the energy position of the free exciton (FE) line for each isotope. This information cannot be obtained directly from spectra as no-phonon FE transition is forbidden and does not feature in Ge photoluminescence. The resulting values are shown in Fig. 7.12 along with the fit based on Eq. 7.3. Error bars mostly stem from the uncertainty in $\hbar\omega_{LA}$ which was indirectly used to calculate the energy gap values. The value of A obtained from the fit is $A = -0.38 \pm 0.01\,\text{eV}\,(\text{a.m.u.})^{1/2}$, with a relative uncertainty of 2.6 %. Etchegoin et al. [81] used a linear approximation to Eq. 7.3 but their findings were consistent with this value of A. However, their relative uncertainty is significantly higher (when the previously discussed ^{70}Ge value is included) at 19 %.

The E_0 value, corresponding to the FE line energy in the limit of $M_v \to \infty$ is $E_0 =$

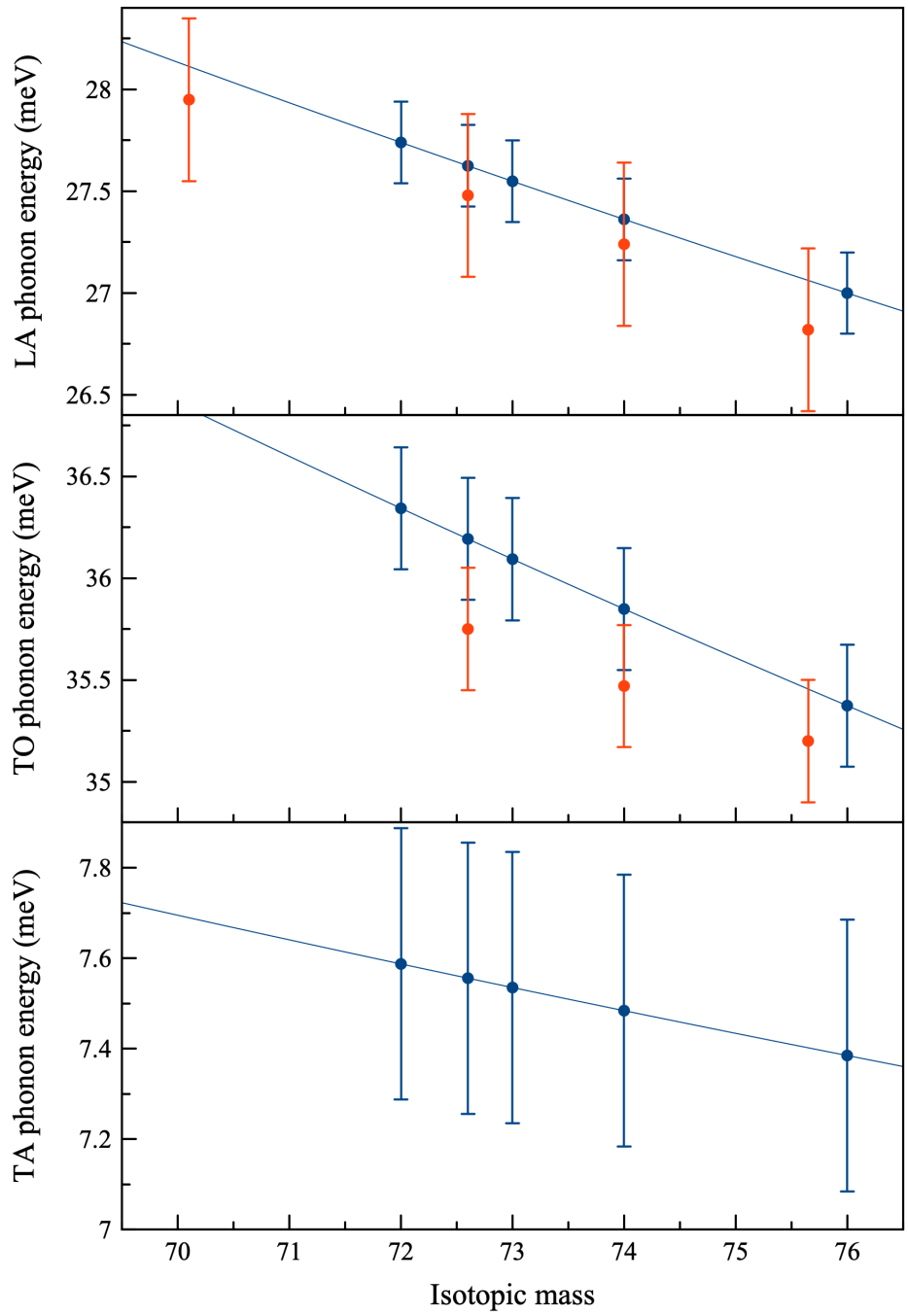

Figure 7.11 Comparison of phonon energies calculated here (blue) to previously reported values from [81] (red). The systematic shifts between blue and red data points are most likely due to the different calculation method or the lineshape fitting scheme. Data presented in this work is more complete and exhibits lower experimental uncertainties.

$0.785 \pm 0.003\,\text{eV}$. Etchegoin et al. report the gap renormalization of $-51.9\,\text{meV}$ (measured) and $-60.65\,\text{meV}$ (theoretical) for ^{70}Ge. Using the above value of E_0, the corresponding renormalization would be a lower value of $-45 \pm 3\,\text{meV}$. Considering the extrapolation needed to obtain this value from a relatively small isotopic spread, this variation is not surprising.

The results presented in this section showed an excellent agreement with the theory outlined earlier. In particular, the high SNR of the acquired data and their thorough analysis permitted the calculation of phonon energies with very low uncertainties. Compared to the earlier studies of isotopic shifts in Ge PL, this work offers a more complete picture and a significantly better quality of the reported values.

7.4 Relative peak intensities

In the indirect PL spectra of Ge, the allowed LA-assisted transition leads to the most intense peak. It is followed by TO (which also gives rise to allowed radiative recombination) and even less intense peaks due to TA- and LO-assisted forbidden transitions. The exact balance of the four peak intensities is governed by phonon deformation potentials which are directly related to the shape of phonon dispersion bands. This may lead to the dependence of relative intensities on isotopic mass.

Those relative intensities associated with different phonon modes were compared based on the values extracted from the fits presented in Fig. 7.5. Fig. 7.13 shows the intensity ratio of the TO and LA peaks. Recorded ratios reproducibly differ in a statistically significant way between the four isotopes studied, although the trend is not monotonic. This could be sample-specific and related to their quality or it could be a more intrinsic, isotope-specific property. In order to verify this, a detailed theoretical calculation of the effect of M_v on phonon deformation potentials would be required which is beyond the scope of this work.

A simpler explanation may exist for the variation in TA/LA PL intensity seen in Fig. 7.14. The ratio increases slightly for ^{74}Ge and more markedly for ^{76}Ge. The TA-assisted transition is forbidden, which means that anything that distorts the symmetry of the lattice creates more favorable conditions for it. The presence of intense BE peaks in ^{76}Ge, weak ones in ^{74}Ge and their absence in ^{73}Ge and ^{72}Ge indicates that the TA/LA ratio increases when the sample quality is compromised.

Table 7.2 Absolute phonon energies for Ge isotopes and natural Ge.

Isotope	Mass (amu)	LA (meV)	TO (meV)	TA (meV)	LO (meV)*
^{72}Ge	72	27.7 ± 0.2	36.3 ± 0.3	7.6 ± 0.3	30.1 ± 0.4
^{nat}Ge	72.6	27.6 ± 0.2	36.2 ± 0.3	7.6 ± 0.3	30.0 ± 0.4
^{73}Ge	73	27.4 ± 0.2	36.1 ± 0.3	7.5 ± 0.3	29.8 ± 0.4
^{74}Ge	74	27.2 ± 0.2	35.8 ± 0.3	7.5 ± 0.3	29.6 ± 0.4
^{76}Ge	76	27.0 ± 0.2	35.4 ± 0.3	7.4 ± 0.3	29.4 ± 0.4

* Calculated assuming $\Delta E_{LO-LA} = 2.4 \pm 0.3$ meV for natural Ge.

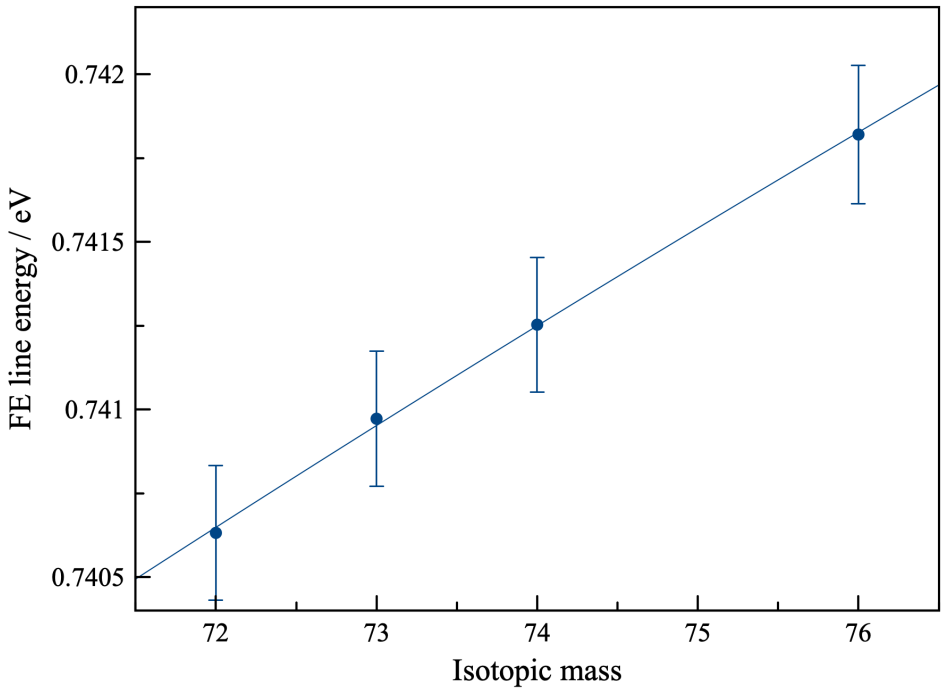

Figure 7.12 Free exciton (FE) line energy in Ge as a function of isotopic mass.

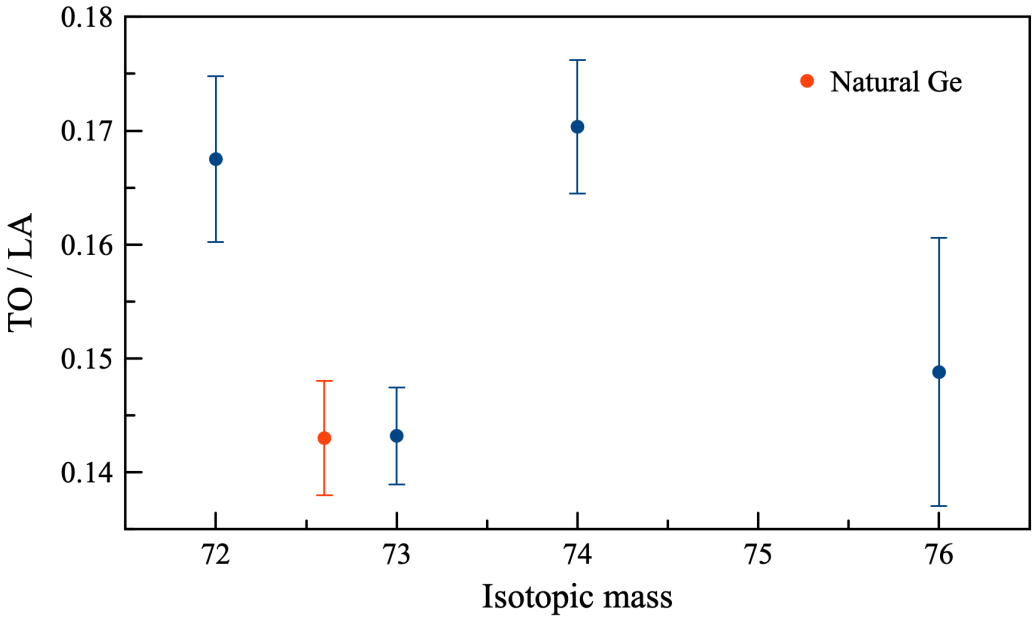

Figure 7.13 Intensity ratio of TO- and LA-assisted PL as a function of isotopic mass. The trend is not monotonous but it is replicable and statistically significant.

Interestingly, the ratio extracted from a ^{nat}Ge spectrum is lower than those exhibited by the isotopically enriched samples. Following the logic outlined in the preceding paragraph, this would suggest that the isotopic purification process negatively impacts the quality of the resulting samples.

7.5 Broadening due to isotopic disorder

Isotopic disorder typically leads to an increase in the broadening of spectral features, as evidenced by measurements of photoluminescence from silicon. Peaks observed in ^{28}Si are roughly three times narrower than their counterparts in natural Si [93]. Somewhat surprisingly, isotopic purification in Ge does not lead to a similarly pronounced decrease in broadening [94].

Section 4.6 described the difficulties associated with accurately extracting Gaussian broadening w_G from indirect PL peaks in Ge. Fortunately, spectral acquisitions performed in the course of this work numbered in the hundreds which permitted a more rigorous comparison of

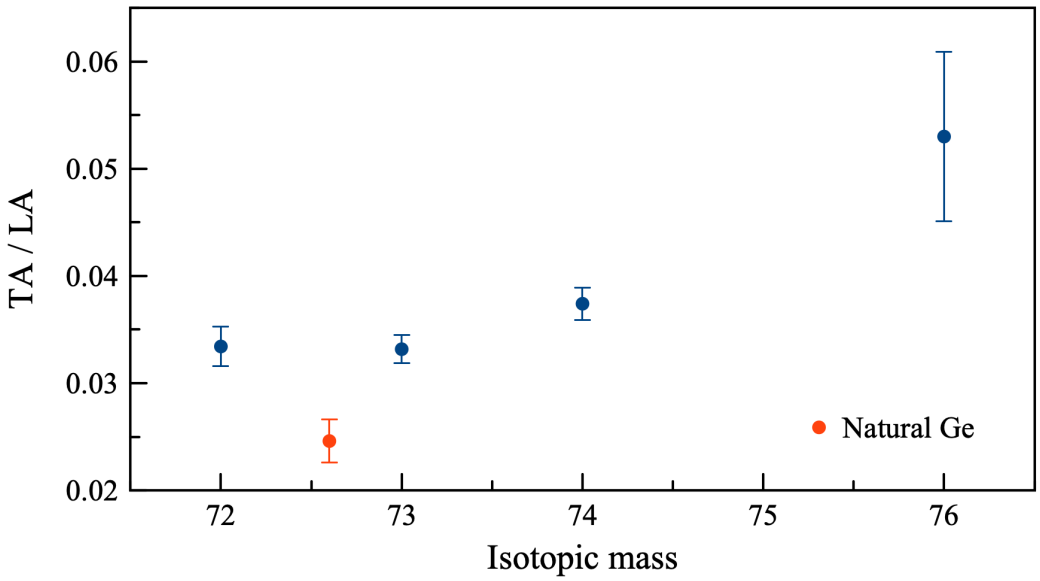

Figure 7.14 Intensity ratio of TA- and LA-assisted PL as a function of isotopic mass. The gradual increase is most likely related to the sample quality, rather than the isotopic mass itself.

natural and isotopically-purified Ge. Still, no statistically significant difference in the Gaussian broadening was observed. The measurement uncertainty of 0.05 meV was calculated from the spreads in extracted w_G values, constituting an upper bound for the contribution due to the isotopic disorder.

Raman spectroscopy offers a more appropriate platform to study this effect, as peak widths are more directly linked to the atomic mass. Also, thermal and collisional broadening do not conceal the Gaussian broadening in the same way they do in indirect PL peaks. Cardona et al. [56] observed a Raman peak width $\Delta\omega$ in natural Ge which was higher than the trend exhibited by the isotopically purified samples. To further validate their finding, they measured a sample consisting of equal parts of ^{70}Ge and ^{76}Ge, designed to maximize isotopic disorder. The resulting $\Delta\omega$ was indeed even higher, as shown in Fig. 7.15.

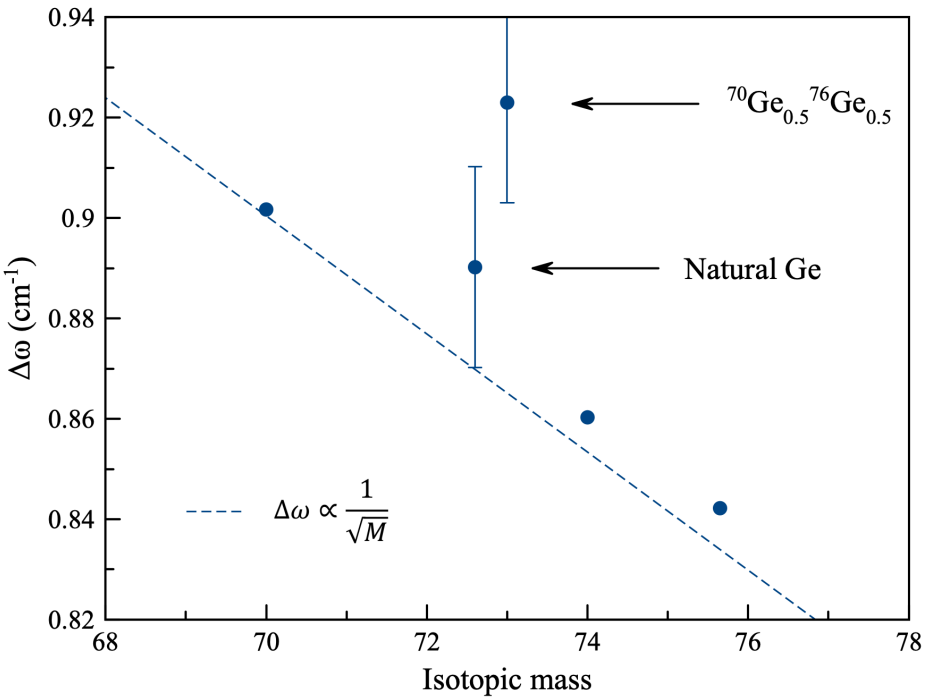

Figure 7.15 Raman peak width $\Delta\omega$ of Ge as a function of isotopic mass. Samples with increased isotopic disorder exhibited higher $\Delta\omega$ values than the trendline would suggest. Data from [56].

The value of $\Delta\omega$ due to the isotopic disorder in natural Ge found by Cardona et al. is 0.02 cm^{-1}, corresponding to 0.0025 meV. This explains why it was not possible to observe

this effect in PL data, with a measurement uncertainty of 20 times that value. The reason for such a small extent of this effect is phonon delocalization in Ge [86,95]. If a phonon is spread over sufficiently many lattice sites, it does not experience the variations of isotopic mass from one site to another. The atomic mass distribution of sites through which it passes is always the same, within the statistical error. The value of $0.02\,\mathrm{cm}^{-1}$ was successfully calculated [56] using the formalism of Anderson localization [96].

The inability to reduce spectral widths by isotopic purification may seem like a disadvantage of Ge. However, this inability stems from the fact that the isotopic inhomogeneity does not play a significant part in natural Ge, meaning that the disorder is not an issue in the first place.

7.6 Exciton energy splitting

So far in this chapter, all spectral fits assumed a constant energy splitting in the electronic ground state of $\Delta E = 0.77\,\mathrm{meV}$, consistent with the value determined in Section 4.3. Fig. 7.16 shows the extracted values for ΔE when it is allowed to vary as a free parameter. There is an apparent trend, with the splitting decreasing by $0.08\,\mathrm{meV}$ from ^{72}Ge to ^{76}Ge.

However, this change far exceeds the expected behavior. Within the linear approximation to Eq. 7.3, electronic energies should scale according to:

$$\frac{\Delta E}{E} \propto \frac{\Delta M}{M}$$

Based on other energy shifts reported in this chapter, the change in ΔE is expected to be $\sim 0.002\,\mathrm{meV}$. The apparent shift of $0.08\,\mathrm{meV}$ is most likely the result of systematic errors stemming from the fitting procedure. As the isotopic mass increases, TO and LA peaks move closer together in energy affecting the way in which the fit handles the limitations of the theoretical model. Given significant measurement uncertainties and temperature variations, this could also be a purely random effect.

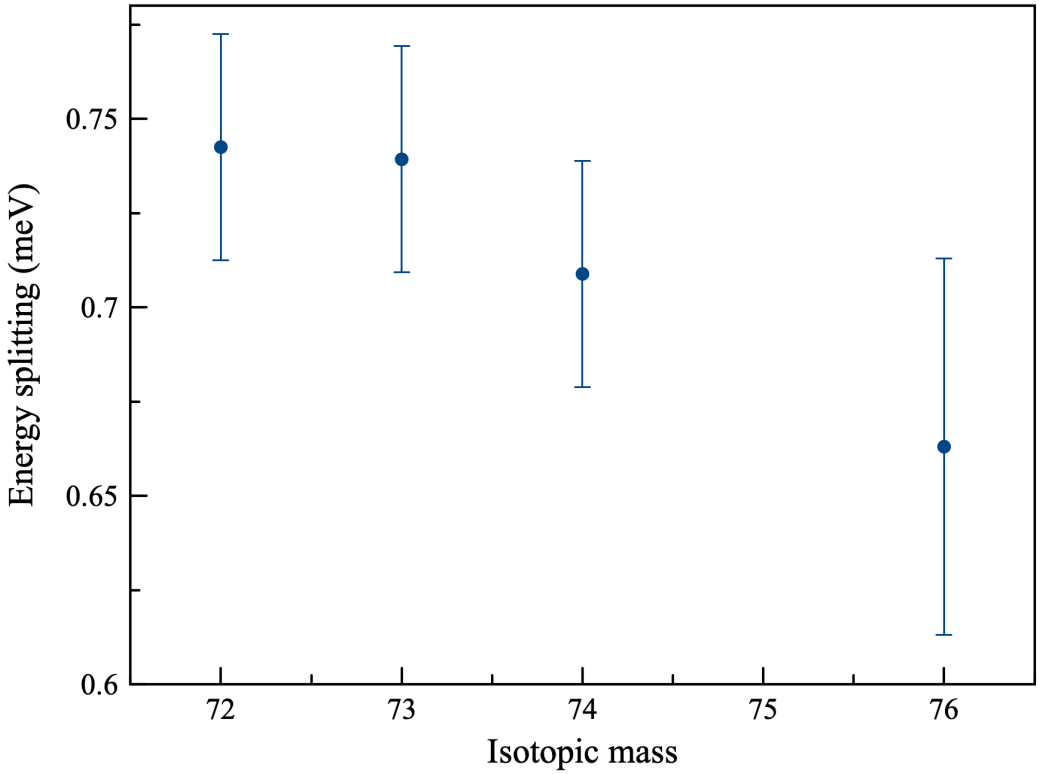

Figure 7.16 Energy splitting in the ground state of the indirect exciton as a function of the isotopic mass.

7.7 Conclusions

The comprehensive analysis of indirect PL spectra of isotopically purified Ge presented in this chapter has exceeded the quality of earlier reports in several key ways. To begin with, the samples were of superior isotopic purity and crystal quality. Furthermore, the carefully optimized experimental set-up and the detailed understanding of the impact of excitation conditions allowed the acquisition of spectra with much higher SNR. The more intricate model used for fitting PL spectra permitted the extraction of PL parameters with lower uncertainties. Finally, this analysis included ^{72}Ge and ^{73}Ge (absent from earlier PL studies) and examined the peaks stemming from the TA-assisted transition.

The shifts in energy positions of the PL peaks showed an excellent agreement with the theoretical models. The results were largely in agreement with existing literature (while exhibiting lower uncertainties) but the energy gap renormalization due to electron-phonon

interactions obtained here was lower (-45 ± 3 meV, compared to -51.9 meV in [81]). Notably, absolute phonon energies for all phonon modes and for all 4 isotopes (as well as natural Ge) were reported with lower uncertainties than any other study.

Isotopic trends in relative intensities of peaks associated with different phonon modes were reported for the first time. While the behavior of the TA/LA intensity ratio appears to stem from the quality of the samples, the TO/LA ratio exhibited a genuine isotopic trend (both TO- and LA-assisted transitions are allowed and should respond similarly to the compromised crystal quality). However, the detailed calculations required to explore this avenue were beyond the scope of this work.

Two other aspects of PL spectra discussed here were the additional broadening due to the isotopic disorder as well as the change in the energy splitting in the excitonic ground state. In both cases, the scale of these effects was too small to be resolved based on the lineshapes of PL peaks. However, the author has the satisfaction of having approached the limit of what is possible to achieve.

CHAPTER 8 CONCLUSION

The comprehensive investigation of Ge PL presented in this thesis has systematically addressed fundamental aspects of indirect radiative recombination, building towards an analysis of isotopic effects. The work has progressed through careful experimental optimization, rigorous theoretical modeling and detailed spectroscopic analysis to achieve outstanding precision in characterizing Ge PL across multiple isotopes.

8.1 Summary of results

The foundation of this research was established through the meticulous optimization of the experimental set-up. Solving the problem of spectrometer-induced alignment shifts represented a critical breakthrough that enabled all subsequent high-quality measurements. The shifts in the detector's focal plane were reduced from more than $100\,\mu$m to less than $3\,\mu$m over the available spectral range, representing a vast improvement over the original design. The technical solution was based on careful theoretical modelization and addressed the fundamental nature of the problem with elegant simplicity. Without this enhanced detection capability, many of the subtle features of Ge PL demonstrated throughout this work could not have been successfully resolved.

A theoretical framework for indirect PL lineshapes was presented and rigorously validated, encompassing all known contributions to the spectral lineshape. While following established mathematical approaches from the literature, this work provided novel insights through systematic examination of each spectral component. The accurate determination of the excitonic ground state energy splitting, $\Delta E = 0.77 \pm 0.05\,$meV, was achieved thanks to the exceptional quality of the experimental data. The consistency between this value and the independently derived result of $\Delta E = 0.7 \pm 0.2\,$meV from temperature-dependent relative amplitude analysis provides a compelling validation of both approaches.

Perhaps the most significant theoretical advancement was the attribution of the collisional broadening mechanism. Through comprehensive power dependence, temperature dependence and spectral analysis, this work conclusively demonstrated that collisional broadening in Ge is predominantly caused by exciton-free carrier interactions, rather than exciton-exciton collisions, directly contradicting established literature. The demonstration of the $I_{PL} \propto \Gamma_L^2$

relationship in the nonlinear regime provided the strongest evidence for this interpretation, while the behavior of the $\Delta x/\Gamma_L$ ratio further supported this conclusion, as it was inconsistent with the van der Waals interaction potential. This finding represents a shift in the understanding of carrier interaction mechanisms in indirect semiconductors.

The investigation also provided crucial clarification regarding the Gaussian broadening in Ge PL spectra. By demonstrating that fitted σ values are extremely sensitive to experimental variations and other fit parameters, this work explained the high level of inconsistency in reported values in the subject literature. No evidence was found for statistically significant Gaussian broadening exceeding instrumental resolution, resolving a long-standing source of confusion in the field.

The analysis of excitation conditions revealed important dependencies that had been incompletely understood due to limited data in previous studies. The systematic investigation of laser wavelength effects provided compelling evidence that the observed trends arise from interactions with defects, rather than fundamental band structure effects. This interpretation offers a consistent explanation for previously disparate observations, even though the anomalous case of 633 nm excitation illustrates the need for further research. Furthermore, the discussion itself has clarified a number of important conceptual points.

The investigation into the role of the numerical aperture of the excitation explicitly demonstrated the dominant role of lateral out-diffusion in establishing the spatial distribution of charge carriers. The diffusion model from Menedez et al. [36] offered an order of magnitude estimate of the measured quantities. The remaining significant disparity pointed towards the role of surface effects and offered a possible experimental avenue to study them in the future.

The enhanced PL due to carrier localization constituted a striking finding that does not seem to have been addressed in literature. While the explanation of it offered in this thesis is tentative, careful documentation of the effect may allow a more definitive future resolution.

The investigation of bound exciton transitions associated with phosphorus impurities provided additional insights into defect physics in Ge. The power exponent of ~ 1.5 observed for these transitions, and temperature dependencies of intensities associated with different

peaks, offer important clues in understanding the underlying carrier dynamics. Even though the detailed analysis was not pursued in this work, it is pertinent to research project pursued simultaneously. The observation of BE LA replicas also enabled a precise measurement of absolute LA phonon energy, enabling the phonon energy calculation presented in Chapter 7.

These efforts in the experimental technique, theoretical modeling and the understanding of excitation conditions culminated in the comprehensive isotopic analysis that represents the primary achievement of this thesis. The investigation of isotopically purified ^{72}Ge, ^{73}Ge, ^{74}Ge, and ^{76}Ge samples exceeded the quality of the previous reports in several different ways. The superior isotopic purity and crystal quality of the samples, combined with the optimized experimental set-up and detailed understanding of excitation effects, enabled the acquisition of spectra with unprecedented signal-to-noise ratios. The detailed fitting model, incorporating all insights gained from earlier chapters, permitted extraction of PL parameters with significantly reduced uncertainties.

The isotopic energy shifts of PL peaks demonstrated excellent agreement with theoretical models, validating the fundamental understanding of phonon-mediated transitions and how they scale with isotopic mass. While largely consistent with existing literature, this work achieved lower uncertainties and provided a more complete picture by including ^{72}Ge and ^{73}Ge (absent from earlier PL studies). The energy gap renormalization due to electron-phonon interactions was determined to be $-45 \pm 3\,\text{meV}$, somewhat lower than previously reported values but with improved precision.

For the first time, isotopic trends in relative intensities of peaks associated with different phonon modes were systematically characterized. While the TA/LA intensity ratio variations appeared to correlate with sample quality, the TO/LA ratio exhibited genuine isotopic dependence. The measurement of absolute phonon energies for all modes across all four isotopes and natural Ge established reliable reference values for future theoretical and experimental research. The systematic analysis also revealed that effects such as additional broadening due to isotopic disorder and changes in the excitonic ground state energy splitting, while theoretically predicted, occur at scales below the resolution limits of current experimental techniques.

As a by product of multiple T dependence measurements throughout this thesis, the free

exciton binding energy was obtained multiple times. These values are presented in Table 8.1. They demonstrate consistency with each other and the values reported in the literature.

Table 8.1 Summary of free exciton binding energies extracted from various analyses presented in this thesis.

Sample	E_{FE} (meV)	Analysis Method	Figure
Natural Ge	3.4 ± 0.3	T dependence of Γ_L	Fig. 4.9
Natural Ge [42]	3 ± 1	T dependence of Γ_L	Fig. 4.10
^{76}Ge	3.3 ± 0.5	T dependence of I_{PL} due to laser heating	Fig. 5.10
^{76}Ge	3.05 ± 0.15	BE T dependence	Fig. 6.8
^{76}Ge	2.92 ± 0.28	BE T dependence	Fig. 6.8
^{76}Ge	3.0 ± 0.6	T dependence of I_{PL}	Fig. 6.9

8.2 Future research directions

While this thesis offers several insights in a very conclusive manner, other aspects of Ge PL would benefit greatly from further work. In particular, the analysis of excitation wavelengths would be more illuminating if more λ values were used in power dependence measurements.

The diffusion model revealed a possible influence of surface effects on carrier distributions, particularly when large excitation NAs are used. NA-resolved measurements, supported by other findings discussed in this thesis, could be used to probe these surface mechanisms. The PL enhancement due to carrier localization constitutes another phenomenon with an unclear origin and a potentially large impact.

Earlier, the linear increase in the $\Delta x/\Gamma_L$ ratio could be used to better understand the coherence-limiting carrier interactions, if properly modeled. Finally, the information gathered on the behavior of BE peak PL was not fully explored. It would, however, benefit any study of defect-related luminescence in Ge.

* * *

While the progressive development from experimental optimization through theoretical validation to comprehensive spectral and isotopic analysis was always motivated by the search for isotopic trends in Ge, each intermediate step turned out to be a rewarding endeavor in its

own right. The phenomena discussed throughout this thesis are strongly interconnected and provide validation for each other. This multidimensional nature of the analysis ranks this study as one of the most comprehensive presentations of PL characteristics of germanium.

REFERENCES

[1] G. Scappucci *et al.*, "The germanium quantum information route," *Nature Reviews Materials*, vol. 6, pp. 926–943, 2021.

[2] D. E. P. Vanpoucke, "Ab initio study of Pt induced nanowires on Ge(001)," Ph.D. dissertation, University of Twente, Enschede, Netherlands, 2009.

[3] M. E. Kurdi *et al.*, "Band structure and optical gain of tensile-strained germanium based on a 30 band k·p formalism," *Journal of Applied Physics*, vol. 107, p. 013710, 2010.

[4] C. Kittel, *Introduction to Solid State Physics*, 6th ed. New York: John Wiley, 1986.

[5] V. Volodin *et al.*, "Applying an improved phonon confinement model to the analysis of raman spectra of germanium nanocrystals," *Journal of Experimental and Theoretical Physics*, vol. 118, no. 1, pp. 65–71, 2014.

[6] J. W. C. Dunlap and R. L. Watters, "Direct measurement of the dielectric constants of silicon and germanium," *Physical Review*, vol. 92, no. 6, pp. 1396–1397, 1953.

[7] S. Adachi, *Properties of Group-IV, III-V and II-VI Semiconductors*. Chichester, UK: John Wiley & Sons, 2005.

[8] M. Cardona and F. H. Pollak, "Energy-band structure of germanium and silicon: The k·p method," *Physical Review*, vol. 142, no. 2, pp. 530–543, 1966.

[9] I. Saïdi *et al.*, "Band structures of GaAs, InAs, and InP: A 34 k·p model," *Journal of Applied Physics*, vol. 104, p. 023706, 2008.

[10] N. W. Hendrickx *et al.*, "Sweet-spot operation of a germanium hole spin qubit with highly anisotropic noise sensitivity," *Nature Materials*, vol. 23, p. 920–927, 2024.

[11] O. Malkoc *et al.*, "Charge-noise-induced dephasing in silicon hole-spin qubits," *Physical Review Letters*, vol. 129, p. 247701, 2022.

[12] F. H. L. Koppens *et al.*, "Spin echo of a single electron spin in a quantum dot," *Physical Review Letters*, vol. 100, p. 236802, 2008.

[13] E. Evers *et al.*, "Hole spin coherence in InAs/InAlGaAs self-assembled quantum dots emitting at telecom wavelengths," *Physica Status Solidi (B)*, vol. 262, no. 1, p. 2400174, 2025.

[14] G. Burkard *et al.*, "Semiconductor spin qubits," *Reviews of Modern Physics*, vol. 95, no. 2, p. 025003, 2023.

[15] O. Bulancea-Lindvall *et al.*, "Isotope-purification-induced reduction of spin-relaxation and spin-coherence times in semiconductors," *Physical Review Applied*, vol. 19, p. 064046, 2023.

[16] A. Kononov *et al.*, "Proximity-induced superconductivity within the InAs/GaSb edge conducting state," *Physical Review B*, vol. 96, p. 245304, 2017.

[17] M. Aghaee *et al.*, "InAs-Al hybrid devices passing the topological gap protocol," *Physical Review B*, vol. 107, p. 245423, 2023.

[18] Y. Kamata, "High-k/Ge MOSFETs for future nanoelectronics," *Materials Today*, vol. 11, no. 1-2, pp. 30–38, 2008.

[19] I. A. Fischer *et al.*, "On-chip infrared photonics with Si-Ge-heterostructures: What is next?" *APL Photonics*, vol. 7, p. 050901, 2022.

[20] J. R. Sánchez-Pérez *et al.*, "Direct-bandgap light-emitting germanium in tensilely strained nanomembranes," *PNAS*, vol. 108, no. 47, p. 18893–18898, 2011.

[21] O. Moutanabbir *et al.*, "Monolithic infrared silicon photonics: The rise of (Si)GeSn semiconductors," *Applied Physics Letters*, vol. 118, p. 110502, 2021.

[22] S. Choudhary *et al.*, "Novel process integration flow of germanium-on-silicon finFETs for low-power technologies," *Journal of Vacuum Science Technology B*, vol. 41, p. 052203, 2023.

[23] W. I. L. Lawrie *et al.*, "Quantum dot arrays in silicon and germanium," *Applied Physics Letters*, vol. 116, p. 080501, 2020.

[24] Z. Kong *et al.*, "Undoped strained Ge quantum well with ultrahigh mobility of two million," *ACS Applied Materials Interfaces*, vol. 15, no. 23, pp. 28 799–28 805, 2023.

[25] T. Schmidt *et al.*, "Excitation-power dependence of the near-band-edge photoluminescence of semiconductors," *Physical Review B*, vol. 45, no. 16, pp. 8989–8994, 1992.

[26] C. Spindler *et al.*, "Excitation-intensity dependence of shallow and deep-level photoluminescence transitions in semiconductors," *Journal of Applied Physics*, vol. 126, p. 175703, 2019.

[27] P. C. Palleti *et al.*, "Development and morphological analysis of the zone refining process for high purity germanium," *Materials Science in Semiconductor Processing*, vol. 185, p. 108924, 2025.

[28] S. A. Adamchik *et al.*, "Ultrapurification of ^{76}Ge-enriched GeH_4 by distillation," *Inorganic Materials*, vol. 47, p. 694–696, 2011.

[29] M. F. Churbanov *et al.*, "Production of germanium stable isotopes single crystals," *Crystal Research and Technology*, vol. 52, no. 4, p. 1700026, 2017.

[30] Horiba Scientific, "510 16 grating curve," https://www.horiba.com/index.php?id=3363&L=2, accessed: July, 2025.

[31] I. E. Zadeh *et al.*, "Superconducting nanowire single-photon detectors: A perspective on evolution, state-of-the-art, future developments, and applications," *Applied Physics Letters*, vol. 118, p. 190502, 2021.

[32] J. Reader, "Optimizing Czerny-Turner spectrographs: A comparison between analytic theory and ray tracing," *Journal of the Optical Society of America*, vol. 59, no. 9, pp. 1189–1196, 1969.

[33] A. B. Shafer *et al.*, "Optimization of the Czerny-Turner spectrometer," *Journal of the Optical Society of America*, vol. 54, no. 7, pp. 879–887, 1964.

[34] N. O. Lipari and A. Baldereschi, "Energy levels of indirect excitons in semiconductors with degenerate bands," *Physical Review B*, vol. 3, no. 8, pp. 2497–2503, 1971.

[35] Y. Abe, "Electron-hole exchange energy in shallow excitons," *Journal of the Physical Society of Japan*, vol. 19, no. 6, pp. 818–829, 1964.

[36] J. Menendez *et al.*, "Temperature-dependent photoluminescence in Ge: Experiment and theory," *Physical Review B*, vol. 101, p. 195204, 2020.

[37] R. J. Elliott, "Intensity of optical absorption by excitons," *Physical Review*, vol. 108, p. 1384, 1957.

[38] G. W. Kamerman and B. J. Feldman, "Further comments on the luminescence line shape of the free exciton in germanium," *Physical Review B*, vol. 15, no. 2, pp. 1209–1211, 1977.

[39] V. Weisskopf, "Zur theorie der kopplungsbreite und der stossdampfung," *Zeitschrift für Physik*, vol. 77, no. 5-6, pp. 287–301, 1932.

[40] H. M. Foley, "The pressure broadening of spectral lines," *Physical Review*, vol. 69, no. 11-12, pp. 616–628, 1946.

[41] H. R. Griem, *Spectral Line Broadening by Plasmas*. New York and London: Academic Press, 1974.

[42] G. A. Thomas *et al.*, "Collision broadening in the exciton gas outside the electron-hole droplets in Ge," *Physical Review B*, vol. 13, no. 4, pp. 1692–1702, 1976.

[43] I. I. Sobel'man *et al.*, *Excitation of Atoms and Broadening of Spectral Lines*, 2nd ed. Berlin, Heidelberg, New York: Springer-Verlag, 1995.

[44] C. B. a la Guillaume and M. Voos, "Luminescence line shape of free excitons in pure Ge," *Solid State Communications*, vol. 12, pp. 1257–1260, 1973.

[45] F. F. Gross *et al.*, "Nablyudenie vozbuzhdennykh sostoyaniy i eksperimental'noe opredelenie energii svyazi nepryamogo eksitona v germanii," *JETP letters*, vol. 13, pp. 332–336, 1971.

[46] T. K. Lo, "Spectroscopic determination of condensation energy and density of electron-hole droplets in pure Ge," *Solid State Communications*, vol. 15, no. 8, pp. 1231–1234, 1974.

[47] R. R. Lieten *et al.*, "Photoluminescence of bulk germanium," *Physical Review B*, vol. 86, p. 035204, 2012.

[48] E. O. Kane, "Exciton dispersion in degenerate bands," *Physical Review B*, vol. 11, no. 10, pp. 3850–3859, 1975.

[49] M. Altarelli and N. O. Lipari, "Indirect exciton dispersion and line shape in Ge," *Physical Review Letters*, vol. 36, no. 11, pp. 619–622, 1976.

[50] A. Frova *et al.*, "Mass reversal effect in the split indirect exciton of Ge," *Physical Review Letters*, vol. 34, no. 25, pp. 1572–1575, 1975.

[51] E. O. Kane, "Energy band structure in p-type germanium and silicon," *Journal of Physics and Chemistry of Solids*, vol. 1, pp. 82–99, 1956.

[52] A. Honold *et al.*, "Collision broadening of two-dimensional excitons in a GaAs single quantum well," *Physical Review B*, vol. 40, no. 9, p. 6442–6445, 1989.

[53] G. G. Macfarlane *et al.*, "Exciton and phonon effects in the absorption spectra of germanium and silicon," *Journal of Physics and Chemistry of Solids*, vol. 8, pp. 388–392, 1959.

[54] A. Schenk, "A model for the field and temperature dependence of Shockley-Read-Hall lifetimes in silicon," *Solid-State Electronics*, vol. 35, no. 11, pp. 1585–1596, 1992.

[55] Y. P. Varshni, "Temperature dependence of the energy gap in semiconductors," *Physica*, vol. 34, no. 1, pp. 149–154, 1967.

[56] M. Cardona *et al.*, "Effect of isotopic disorder and mass on the electronic and vibronic properties of three-, two- and one-dimensional solids," *Journal of Physics: Condensed Matter*, vol. 5, pp. A61–A72, 1993.

[57] G. A. Thomas *et al.*, "Indirect recombination mechanisms in germanium," *Physical Review B*, vol. 19, no. 2, pp. 702–718, 1979.

[58] C. Jacoboni *et al.*, "Electron drift velocity and diffusivity in germanium," *Physical Review B*, vol. 24, no. 2, pp. 1014–1026, 1981.

[59] A. L. Smirl *et al.*, "Picosecond dynamics of high-density laser-induced transient plasma gratings in germanium," *Physical Review B*, vol. 25, no. 4, pp. 2645–2659, 1982.

[60] S. Michel, *PhD student, Polytechnique Montreal*, 2025, calculations yet to be published.

[61] D. E. Cooper *et al.*, "Photoluminescence spectroscopy of excitons for evaluation of high-quality CdTe crystals," *Journal of Crystal Growth*, vol. 86, pp. 544–551, 1988.

[62] H. M. van Driel *et al.*, "Photoluminescence spectra of germanium at high excitation intensities," *Solid State Communications*, vol. 20, no. 9, pp. 837–840, 1976.

[63] L. Wang *et al.*, "Significant photoluminescence improvements from bulk germanium-based thin films with ultra-low threading dislocation densities," *arXiv preprint arXiv:2404.05663v3*, 1976.

[64] W. Klingenstein and H. Schweizer, "Direct gap recombination in germanium at high excitation level and low temperature," *Solid-State Electronics*, vol. 21, pp. 1371–1374, 1978.

[65] T. Arguirov *et al.*, "Luminescence from germanium and germanium on silicon," *Solid State Phenomena*, vol. 205-206, pp. 383–393, 2013.

[66] A. T. Tarekegne *et al.*, "Dependence of photoluminescence emission on excitation power and temperature in highly doped 6H-SiC," *Physical Review Applied*, vol. 13, p. 064002, 2020.

[67] K. Tanaka *et al.*, "Determination of intervalley scattering time in germanium by sub-picosecond time-resolved raman spectroscopy," *Physical Review Letters*, vol. 71, no. 12, pp. 1935–1938, 1993.

[68] C. J. Kaplan *et al.*, "Femtosecond tracking of carrier relaxation in germanium with extreme ultraviolet transient reflectivity," *Physical Review B*, vol. 97, p. 205202, 2018.

[69] R. F. Potter, "Optical constants of germanium in spectral region from 0.5 eV to 3.0 eV," *Physical Review*, vol. 150, no. 2, pp. 562–567, 1966.

[70] C. Emminger *et al.*, "Temperature dependent dielectric function and direct bandgap of Ge," *Journal of Vacuum Science Technology B*, vol. 38, p. 012202, 1967.

[71] G. A. Thomas *et al.*, "Liquid-gas phase diagram of an electron-hole fluid," *Physical Review Letters*, vol. 33, no. 4, pp. 219–222, 1974.

[72] L. V. Keldsyh and A. M. Kozlov, "Collective properties of excitons in semiconductors," *Soviet Physics JETP*, vol. 27, no. 3, pp. 521–528, 1968.

[73] Y. Pokrovskii, "Condensation of non-equilibrium charge carriers in semiconductors," *Physica Status Solidi*, vol. 11, pp. 385–410, 1972.

[74] C. B. a la Guillaume *et al.*, "Condensation of free excitons into electron-hole drops in pure germanium," *Physical Review B*, vol. 5, no. 8, pp. 3079–3087, 1972.

[75] V. M. Asnin *et al.*, "Giant fluctuations of photocurrent in germanium," *JETP Letters*, vol. 11, no. 3, pp. 162–165, 1970.

[76] Y. Pokrovskii and K. I. Svistunova, "Light scattering by drops of the condensed phase of nonequilibriurn carriers in germanium," *JETP Letters*, vol. 13, no. 6, pp. 297–301, 1971.

[77] C. B. a la Guillaume and M. Voos, "Electron-hole drops in pure Ge," *Physical Review B*, vol. 7, no. 4, pp. 1723–1727, 1973.

[78] R. W. Martin, "Observation of bound multiple-excitons in germanium," *Solid State Communications*, vol. 14, no. 4, pp. 369–372, 1974.

[79] A. E. Mayer and E. C. Lightowlers, "Bound-exciton luminescence and absorption in phosphorus-doped germanium," *Journal of Physics C: Solid State Physics*, vol. 12, no. 13, pp. 539–544, 1979.

[80] N. L. Rowell *et al.*, "Optical emission from germanium nanocrystals," *ECS Journal of Solid State Science and Technology*, vol. 7, no. 12, pp. 195–205, 2018.

[81] P. Etchegoin *et al.*, "Isotope effect in Ge: a photoluminescence study," *Solid State Communications*, vol. 83, no. 11, pp. 843–848, 1992.

[82] G. Kirczenow, "A new model for bound multiexciton complexes," *Solid State Communications*, vol. 21, no. 8, pp. 713–715, 1977.

[83] J. R. de Laeter *et al.*, "Atomic weights of the elements. Review 2000 (IUPAC Technical Report)," *Pure and Applied Chemistry*, vol. 75, no. 6, pp. 683–800, 2003.

[84] M. Asen-Palmer *et al.*, "Thermal conductivity of germanium crystals with different isotopic compositions," *Physical Review B*, vol. 56, no. 15, pp. 9431–9447, 1975.

[85] H. D. Fuchs *et al.*, "Isotopic disorder-effects on the phonons in germanium," *Solid State Communications*, vol. 82, no. 4, pp. 225–228, 1992.

[86] ——, "Anharmonic decay time, isotopic scattering time, and inhomogeneous line broadening of optical phonons in ^{70}Ge, ^{76}Ge, and natural Ge crystals," *Physical Review B*, vol. 44, no. 16, pp. 8633–8642, 1991.

[87] V. F. Agekyan *et al.*, "Izotopicheskii effekt v germanii," *Fizika Tverdogo Tela*, vol. 31, no. 12, pp. 101–104, 1989.

[88] S. Zollner *et al.*, "Isotope and temperature shifts of direct and indirect band gaps in diamond-type semiconductors," *Physical Review B*, vol. 45, no. 7, pp. 3376–3385, 1992.

[89] J. Camassel and D. Auvergne, "Temperature dependence of the fundamental edge of germanium and zinc-blende-type semiconductors," *Physical Review B*, vol. 12, no. 8, pp. 3258–3267, 1975.

[90] M. Cardona *et al.*, "Isotope effects on the electronic excitations and phonons in semiconductors," *Journal of Non-Crystalline Solids*, vol. 141, pp. 257–264, 1992.

[91] G. Davies *et al.*, "Isotope dependence of the indirect energy gap of germanium," *Semiconductor Science and Technology*, vol. 7, pp. 1271–1273, 1992.

[92] G. Nelin and G. Nilsson, "Phonon anharmonicity of germanium in the temperature range 8-80 K," *Physical Review B*, vol. 10, no. 2, pp. 612–620, 1974.

[93] D. Karaiskaj *et al.*, "Photoluminescence studies of isotopically enriched silicon," *Physica Status Solidi*, vol. 235, no. 1, pp. 63–74, 2003.

[94] E. E. Haller, "Isotopically controlled semiconductors," *Solid State Communications*, vol. 133, p. 693–707, 2005.

[95] H. D. Fuchs *et al.*, "Comparison of the phonon spectra of ^{70}Ge and natural Ge crystals: Effects of isotopic disorder," *Physical Review B*, vol. 43, no. 6, pp. 4835–4842, 1991.

[96] P. W. Anderson, "Absence of diffusion in certain random lattices," *Physical Review*, vol. 109, no. 5, pp. 1492–1505, 1958.